universität wien

MASTERARBEIT / MASTER'S THESIS

Titel der Masterarbeit / Title of the Master's Thesis

„Generation of Aerosol Nanoparticles of different Composition in Air and Helium“

verfasst von / submitted by

Gerald Köberl BSc

angestrebter akademischer Grad / in partial fulfilment of the requirements for the degree of

Master of Science (MSc)

Wien, 2019 / Vienna, 2019

Studienkennzahl lt. Studienblatt / degree programme code as it appears on the student record sheet:	A 066 876
Studienrichtung lt. Studienblatt / degree programme as it appears on the student record sheet:	Masterstudium Physik
Betreut von / Supervisor:	Assoz. Prof. Dr. Paul Winkler

Danksagung

Mein gesamtes Studium, im Speziellen diese Arbeit, wäre ohne Hilfe nicht möglich gewesen. An dieser Stelle möchte ich mich bei all jenen bedanken, die mich auf diesem Weg begleitet, und mir diesen erleichtert haben.

In erster Linie gilt mein Dank meinem Betreuer, Assoz. Prof. Dr. Paul Winkler, für die Aufnahme in das Team von Nanodynamite, das ständig großartige Arbeitsklima, sowie für das Ermöglichen von überaus spannenden Reisen zu Großforschungsanlagen. Großes Dankeschön dem gesamten Team von Nanodynamite, das mich nicht nur herzlich ins Team aufgenommen hat, sondern mir auch immer mit Rat und Tat zur Seite gestanden ist.

Besonderen Dank möchte ich Paulus Bauer aussprechen. Von ihm durfte ich in meinem letzten Studienjahr, auch abseits der Aerosolphysik und der täglichen Laborarbeit, unheimlich viel lernen. Die ständige und aktive Hilfsbereitschaft bei aufgetretenen Herausforderungen ist keineswegs selbstverständlich. Selbst unendlich scheinende Autobahnkilometer auf Forschungsreisen, sowie lange Nachtstunden bei Messungen am Synchotron wurden auch durch ihn zu einem besonderen Erlebnis.

Ohne Rückhalt meiner Familie, meinen Schwestern Sonja und Silvia, sowie meinen Eltern Stefanie und Franz, wäre das Abschließen des Studiums im Allgemeinen, und somit das Verfassen dieser Arbeit im Speziellen aber nicht möglich gewesen. Vor allem Letzteren danke ich herzlich für die immerwährende Fürsprache und Unterstützung in jeglicher Hinsicht.

Ausgesprochen großer Dank gilt auch meiner Freundin Anita. Danke für das Aufrichten in Momenten des Zweifels, danke für den ständigen Zuspruch!

Euch allen ist diese Arbeit gewidmet!

Abstract

The basic objective of this thesis is to provide a complete characterization of three different aerosol nanoparticle generators, a tungsten oxide (WO_x) generator, a glowing wire generator and a tube furnace in two different carrier gases, air and helium.

These state-of-the-art techniques allow to synthesize nanosize particles with control over number, size and composition. Sizing as well as counting of the particles is done with a Differential Mobility Particle Sizer (DMPS), which consists in principal of an aerosol neutralizer to electrically charge the particles, a Differential Mobility Analyzer (DMA) to classify them according to their electrical mobility, and a particle counter, such as a Faraday Cup Electrometer (FCE). In order to gain information about the structural composition of the nanoparticles, Transmission Electron Microscopy (TEM) images are taken.

Finding new approaches to characterize aerosol nanoparticles requires detailed knowledge of the synthesized particles. In this work, nanoparticles of three generators are studied. This information is needed exemplary for the application of small angle x-ray scattering (SAXS) on studying aerosol nanoparticles performed by Bauer [2019]. Because helium carried particles are particularly suitable for SAXS studies, the characteristics of the generators using helium instead of air are of great interest.

The Grimm WO_x generator #7.860 malfunctioned in helium, whereas in air it was found to be a very stable source of particles between 4 nm and 20 nm with high concentrations. The hot-wire generator was operated with different wire materials. Tungsten turned out to be the best source for stable nanoparticle generation with high concentrations over the period of several hours. The tube furnace was used to generate exceedingly stable concentrations of salt and silver nanoparticles in air and helium. For silver, particle modes between 6 nm and 12 nm (in the case of air) and 4 nm and 9 nm (helium) were measured. Salt particles were detected in the size range between 4 nm and 40 nm (in the case of air).

In addition to measurements of the number size distributions of the generated particles, the effect of humidity on sodium chloride nanoparticles was studied. It is shown, that for both carrier gases considered in this work, salt particles shrink in the presence of water vapor. In air, the median of the size distributions decrease by about 14 % between utterly dry and relative humidity of 34 %. Beyond that, size resolved data shows, that smaller particles shrink less than bigger ones.

Kurzfassung

Die grundlegende Zielsetzung dieser Arbeit ist eine vollständige Charakterisierung von drei unterschiedlichen Aerosol-Nanopartikel Generatoren, dem Grimm Wolframoxid (WO_x) Generator, einem Glühdraht-Generator und einem Rohrofen, in zwei unterschiedlichen Trägergasen, Luft und Helium.

Diese Generatoren erlauben das Erzeugen von Nanopartikeln mit Kontrolle über deren Anzahl, Größe sowie Zusammensetzung. Die Messung der Partikelgrößenverteilung erfolgt durch einen differentiellen Mobilitätsanalysator (DMA). Dazu ist es notwendig, dass die Nanopartikel davor in einen wohldefinierten Ladungszustand gebracht werden. Anschließend folgt die Zählung in einem Elektrometer (FCE). Um Informationen über die Struktur der Nanopartikel zu erhalten, wurden Bilder mittels eines Transmissionselektronenmikroskops (TEM) angefertigt.

Neue Herangehensweisen zur Charakterisierung von Nanopartikeln erfordern detailliertes Wissen über die künstlich hergestellten Teilchen. In dieser Arbeit werden die Partikel von drei Generatoren charakterisiert. Diese Information ist beispielsweise für die Anwendung von Kleinwinkelröntgenstreuung (SAXS) zur Untersuchung von Nanopartikeln, wie der Studie von Bauer [2019], von erheblicher Bedeutung. Da sich heliumgetragene Partikel für SAXS Studien als besonders geeignet herausstellten, sind in Helium generierte Teilchen von besonderem Interesse.

Der Grimm Wolframoxid (WO_x) Generator #7.860 konnte nicht mit Helium betrieben werden, für Luft stellte er sich jedoch als außerordentlich stabiler Generator von hohen Nanopartikelkonzentrationen mit Größen zwischen 4 nm und 20 nm heraus. Der Glühdraht-Generator wurde mit Drähten verschiedener Materialien betrieben. Wolfram zeigte sich dabei als am Geeignetsten für die Generierung von stabilen und hohen Konzentrationen von Nanopartikeln. Besonders beständige Teilchenkonzentrationen von Salz und Silber in Luft sowie Helium konnten mit dem Rohrofen generiert werden. Für Silber lagen die Modalwerte der Anzahlgrößenverteilungen zwischen 6 nm und 12 nm (in Luft generiert), sowie 4 nm und 9 nm (in Helium). In Luft erzeugte Salzpartikel hatten Größen zwischen 4 nm und 40 nm.

Zusätzlich zur Messung von Anzahlgrößenverteilung der generierten Teilchen wurde der Einfluss von Feuchtigkeit auf Natriumchlorid Nanoteilchen untersucht. Es stellte sich heraus, dass die Partikel sowohl in Luft, als auch in Helium in Anwesenheit von Wasserdampf schrumpfen. In Luft sinkt der Median der Anzahlgrößenverteilungen, zwischen trockenen Bedingungen und relativer Feuchtigkeit von 34 % um etwa 14 %. Darüber hinaus zeigen Messungen mit Nanopartikeln verschiedener Größe, dass kleinere Teilchen prozentual weniger schrumpfen als größere.

Contents

1 Introduction

Aerosols are suspensions of solid particles or liquid droplets in a gaseous medium in sizes within a few nanometer and 100 μm. They are ubiquitous in the atmosphere of the earth and their origin is manifold. Dust, fume, haze, smog, smoke and spray, as well bioaerosols like viruses, fungi and pollen, all these terms are summarized as aerosols ([Hinds, 1999, p.3-6]).

In general, they can be divided in two categories: primary and secondary aerosols. Primary aerosols are introduced straight into the atmosphere, like sea spray or volcano ashes, whereas the latter nucleate through gas-to-particle conversions. This process is often termed New Particle Formation (NPF) and has a considerable influence on aerosol climate effects (Kulmala et al. [2013]).

Aerosol science is often equated with pollution control. According to the World Health Organisation (WHO), ambient air pollution kills about 3 million people per year (WHO [2016]). However, controlling particle emissions in order to prevent detrimental human health effects is only one aspect. Primary, as well as secondary nucleated particles have a strong influence on the formation of clouds (Merikanto et al. [2009]), and radiative forcing (Haywood and Boucher [2000]). The latter is poorly understood, its uncertainties are much larger than uncertainties in positive forcing caused by changes in greenhouse gases for example carbon dioxide (Carslaw et al. [2013], IPCC [2013]). As a result, in recent years, a lot of effort is put into a better understanding of these complex concepts.

Especially nanoparticles, particles within 1 and 100 nm ([Kulkarni et al., 2011, p. 5]), are of special interest. Their profound impact on various research areas include not only their significant effect on total numbers of Cloud Condensation Nuclei (CCN's) and therefore the earths' climate (Merikanto et al. [2009]), but also industrial use of nanoscale materials (Stark et al. [2002], Santos et al. [2015]), as well as possible benefits and concerns of human exposure to nanoparticles (Handy and Shaw [2007]). Contrarily to risks regarding human health caused by natural airborne nanoparticles (Forbes [2003]) or anthropogenic sources (Dahl et al. [2006], Kittelson et al. [2004]), ultrafine particles have many beneficial medical applications as well. For instance, synthesized silver nanoparticles have an antibacterial and antifungal effect (Khaydarov et al. [2009]) which allows development of low cost water filters (Jain and Pradeep [2005]). Beyond that, the use of nanoparticles leads to new applications in diagnosis and treatment of cancer (Yezhelyev et al. [2006]).

These widespread research fields are all based on the need for a clear understanding of the convoluted behavior of nanoparticles. The fundamental objective of this thesis is to acquire further knowledge on the generation of aerosol nanoparticles in different carrier

gases, that can lead to new experimental approaches. Using helium instead of air as carrier gas prepared the ground for in-situ nanoparticle characterization utilizing Small Angle X-ray Scattering (SAXS) performed by Bauer [2019].

In this work, different nanoparticle generators are characterized. It should provide an overview of theoretical and experimental challenges as much as distinctions of different mobility analysis in varying carrier gases and commonly used aerosol nanoparticle generators.

The initial section of this thesis gives a theoretical overview of differential mobility analysis with close attention on discrepancies between air and helium. Subsequently, brief descriptions of the operated equipment is given, as well as theoretical background on calculation of the particle size distributions. Inversion of the raw data requires considerable effort, especially when different carrier gases are involved.

Experimental results regarding characterization of the nanoparticle generators are presented, and advantages and drawbacks of each approach are discussed.

Moreover, experimental findings of humidity effects on sodium chloride nanoparticles in air and helium are provided. It turns out that in the presence of increasing relative humidity, the particles shrink depending on their initial size.

2 Differential Mobility Analysis of Aerosols

The distribution of particles regarding size is one of the most important measurements in aerosol physics. A common method to obtain information concerning size of aerosol particles is differential mobility analysis. This is achieved by using an apparatus that classifies aerosols, commonly called Differential Mobility Analyzer (DMA).

The idea of particle sizing by measuring the different mobility of aerosols with a DMA was introduced by Hewitt [1957]. There are several different types of DMA geometries, for example parallel plated configurations (Zhang and Wexler [2006]) or radial DMA's (Zhang et al. [1995]). Nevertheless, the standard design is the coaxial cylindrical DMA, as described by Knutson and Whitby [1975] and Liu and Pui [1974], which was further developed to the so called Vienna Type DMA (Winklmayr et al. [1991]), and was entirely used in this work.

2.1 Basic Principles

In this section, the theory of a coaxial cylindrical DMA, as shown in Figure 2.1 is described.

The DMA is fundamentally composed of two concentric electrodes, where the inner one is maintained at a certain voltage at about 1 V to 10 kV (both polarities are adjustable), whereas the outer electrode is grounded.

From the top, particle-free sheath gas Q_{sh} enters the coaxial chamber, filling the gap between inner and outer electrode. A nylon mesh screen ensures laminar flow. At this point it should be mentioned, that "top" only refers to the illustration. Since for this size range, gravitational effects are imperceptible, the DMA can be operated in arbitrary position, without compromises in performance (Winklmayr et al. [1991]). Furthermore the beforehand charged polydisperse aerosol is introduced tangentially (Q_{ae}). As a consequence of the electric field, particles of suitable polarity are attracted by the inner electrode. The particles drift according their electrical mobility through the sheath gas flow. A small fraction of them within a certain range of electrical mobility is able to reach a narrow sample outlet (Q_s). The remaining particles are exhausted via the Q_{ex} flow.

Because of the geometry of the DMA (radii R_{in}, R_{out} and length L) and predefined working conditions (Q_{sh}, Q_{ae}, Q_{ex}, Q_s), it's possible to calculate the electrical mobility Z of the classified particles in Q_s, and further on their mobility equivalent diameter D_p. Since there is no

information about the shape of the nanoparticle, one can only determine its mobility equivalent diameter, which is the diameter of a spherical particle, that behaves like the appointed nanoparticle in the electric field [Kulkarni et al., 2011, p.6]

2.2 Theory of Differential Mobility Analysis

This section is primarily based on previous essential work of Knutson and Whitby [1975], Flagan [1998] and Steiner [2011].

The mobility μ is a measure of the relative ease of creating steady motion for an aerosol particle:

$$\mu = \frac{\vec{v}}{\vec{F}} \tag{2.1}$$

with the drift velocity of the particle $\vec{v}$ and the force $\vec{F}$ that acts on the particle. For the electrostatic case, Equation 2.1 becomes

$$\mu = \frac{\vec{v}}{i \cdot e_0 \cdot \vec{E}} \tag{2.2}$$

where i is the quantity of e_0 elementary charges, and $\vec{E}$ is the strength of an electric field.

This is why, the electrical mobility Z of a particle is defined as

$$Z = i \cdot e_0 \cdot \mu \tag{2.3}$$

or alternatively

$$Z = \frac{\vec{v}}{\vec{E}} \tag{2.4}$$

In other words Z is the proportionality factor of the drift velocity $\vec{v}$ of a particle that is caused by an electric field with strength $\vec{E}$.

This drift velocity $\vec{v}$ is only dependent on its radial distance r from the axis of the DMA in y direction:

$$\frac{dr}{dt} = Z \left| \vec{E}(r) \right| \tag{2.5}$$

$$\frac{dy}{dt} = v(r) \tag{2.6}$$

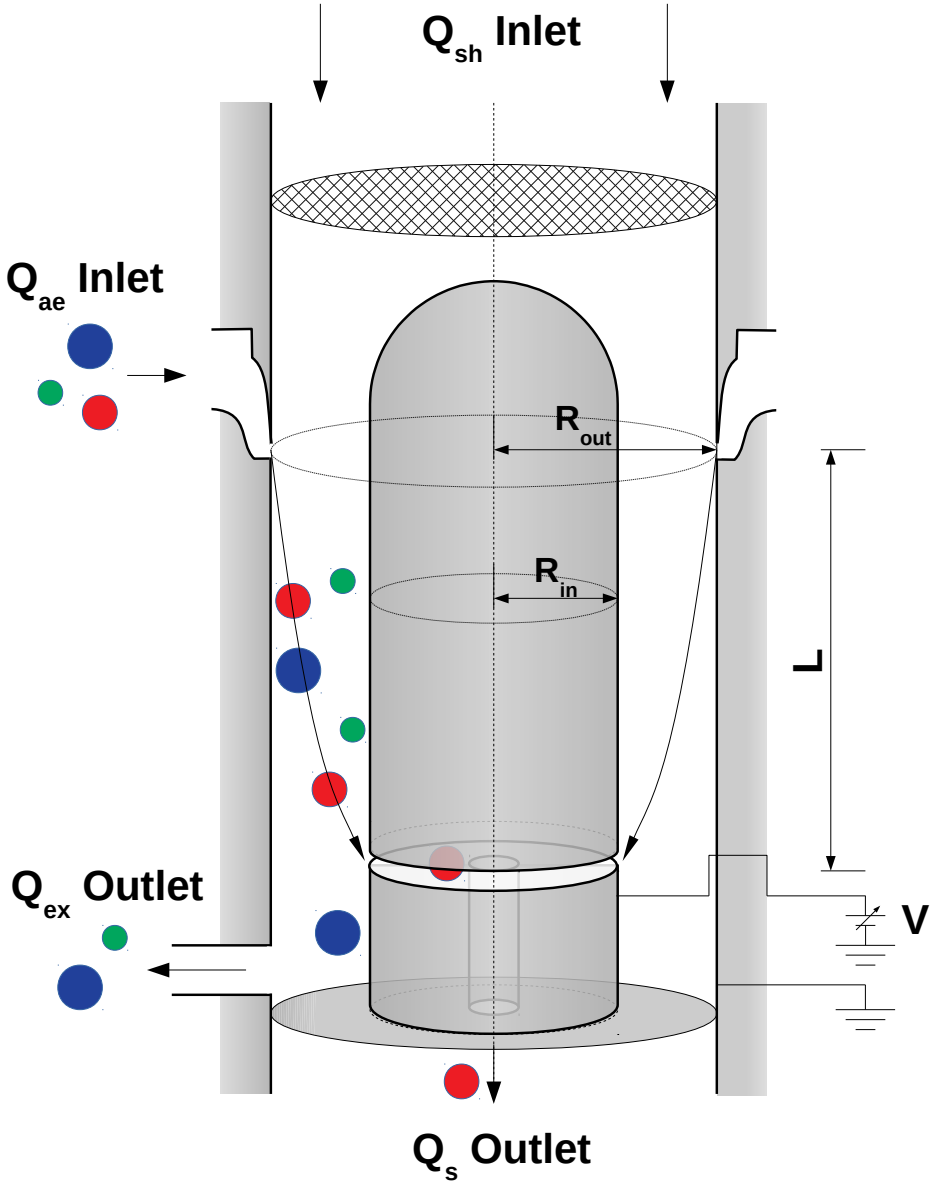

Figure 2.1: Schematic illustration of a Vienna-Type differential mobility analyzer. Sheath gas flows through a laminarization nylon mesh screen into the coaxial analyser chamber. The polydisperse aerosol, pictured as blue, green and red particles, is introduced via the Q_{ae} inlet and if it has the right polarity, it is attracted by the inner electrode. Only particles with a narrow range of electrical mobility reach the sample outlet (red). All other particles are precipitated at either of the electrodes or removed over the exhaust Q_{ex}.

Since a DMA acts like a cylindrical capacitor, the magnitude of an electric field $\left|\vec{E}(r)\right|$ is the following:

$$\left|\vec{E}(r)\right| = \frac{V}{r \cdot \ln\left(R_{out}/R_{in}\right)} \tag{2.7}$$

where V is the applied voltage and r the radial distance from the axial center of the capacitor. Combining 2.5 and 2.7, leads to

$$\frac{dr}{dt} = \frac{Z \cdot V}{r \cdot \ln\left(R_{out}/R_{in}\right)} \quad . \tag{2.8}$$

That's why the complete path of the particle inside a DMA can be written as:

$$\frac{dy}{dr}\frac{dr}{dt} = \frac{dy}{dt} \Rightarrow \frac{dy}{dr} = \frac{dy}{dt}\frac{dt}{dr}$$

$$\frac{dy}{dr} = \underbrace{\frac{r \cdot \ln\left(R_{out}/R_{in}\right)}{Z \cdot V}}_{\frac{dt}{dr}} \frac{dy}{dt}$$

Using Equation 2.6 leads to

$$\frac{dy}{dr} = \frac{\ln\left(R_{out}/R_{in}\right)}{Z \cdot V} \cdot r \cdot v(r) \quad . \tag{2.9}$$

This equation can be straightaway integrated to

$$\int_{y_1}^{y_2} dy = \frac{\ln\left(R_{out}/R_{in}\right)}{Z \cdot V} \cdot \int_{r_1}^{r_2} r \cdot v(r) \cdot dr \quad . \tag{2.10}$$

It proves useful to expand the right side of the equation with 2π and use the circumstance that $\int_{y_1}^{y_2} dy = L$. Therefore one obtains an expression for the electrical mobility Z:

$$Z = \frac{\ln\left(R_{out}/R_{in}\right)}{2 \cdot \pi \cdot L \cdot V} \cdot \int_{r_1}^{r_2} 2 \cdot \pi \cdot r \cdot v(r) \cdot dr \quad . \tag{2.11}$$

As pictured in Figure 2.2, the term $\int_{r_1}^{r_2} 2 \cdot \pi \cdot r \cdot v(r) \cdot dr$ describes the Flow $Q_{\Delta r}$ between the center line of the aerosol flow Q_{ae} and the center line of the sample flow Q_s.

Therefore, Equation 2.11 can be expressed with the flowrates Q_{sh}, Q_{ex}, Q_{ae} and Q_s:

$$Q_{\Delta r} = \int_{r_1}^{r_2} 2 \cdot \pi \cdot r \cdot v(r) \cdot dr = Q_{sh} + Q_{ae} - \frac{Q_s + Q_{ae}}{2} = Q_{ex} + Q_s - \frac{Q_s + Q_{ae}}{2}$$

These deliberations result in

$$Q_{\Delta r} = \int_{r_1}^{r_2} 2 \cdot \pi \cdot r \cdot v(r) \cdot dr = \frac{Q_{sh} + Q_{ex}}{2} \tag{2.12}$$

Using Equation 2.12 and Equation 2.11, the electrical mobility Z is specified as

$$Z = \frac{\ln\left(R_{out}/R_{in}\right)}{2 \cdot \pi \cdot L \cdot V} \cdot \frac{Q_{sh} + Q_{ex}}{2} \tag{2.13}$$

Since a DMA should always operated symmetrically considering the flowrates in the following way (see section 2.4)

$$\begin{aligned} Q_{sh} &= Q_{ex} \\ Q_{ae} &= Q_s \end{aligned}$$

Equation 2.12 can be simplified to

$$Z = \frac{\ln\left(R_{out}/R_{in}\right) \cdot Q_{sh}}{2 \cdot \pi \cdot L \cdot V} \quad . \tag{2.14}$$

This allows direct calculation of the electrical mobility for given geometry of the DMA (R_{in}, R_{out}, and L) as well as working conditions (Q_{sh}).

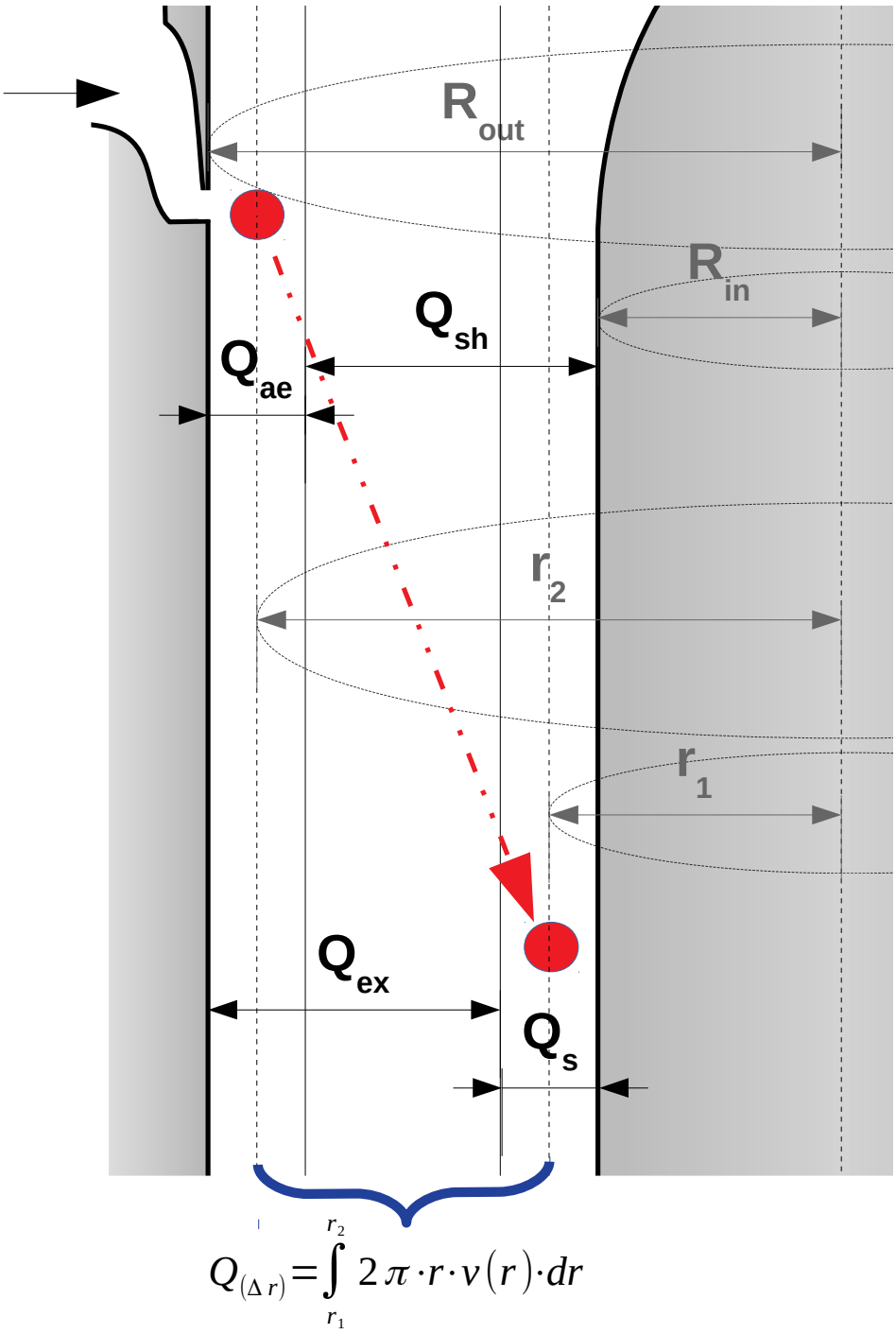

Figure 2.2: Schematic illustration of the volumetric flowrate $Q_{\Delta r}$

2.3 Calculating the Diameter of Aerosol Nanoparticles

Assuming spherical particles in a homogeneous gas, the constant drag force is stated by Stokes' law:

$$F = 3 \cdot \pi \cdot \eta \cdot \vec{v} \cdot D_p \tag{2.15}$$

where η is the viscosity of the carrier gas (η_{Air} = 1.8325· 10^{-5} Pa· s (Birge [1945]) and η_{He} = 1.96 · 10^{-5} Pa · s (Kestin and Leidenfrost [1959])), $\vec{v}$ the drift velocity and D_p the mobility equivalent diameter.

When the particle is in the range of the mean free path λ of the carrier gas, non-continuum effects have to be taken into account (Cunningham [1910]). In this context, the mean free path is the average regarding the traveled distance of a moving molecule of the carrier gas between collisions. The numerical values for the mean free path of air and helium at 20°C and 1 atm are taken from Katz et al. [2011] and Jennings [1988] respectively:

$$\lambda_{Air} = 65.4\,nm$$
$$\lambda_{He} = 191.9\,nm$$

Thus, for nanoparticles, the following corrected derivation of Stokes' law (2.15) has to be used:

$$F = \frac{3 \cdot \pi \cdot \eta \cdot \vec{v} \cdot D_p}{C(D_p)} \tag{2.16}$$

with the Cunningham slip correction factor $C(D_p)$ introduced by Cunningham [1910]:

$$C(D_p) = 1 + \frac{\lambda}{D_p}[A + B \cdot \exp(-C \cdot \frac{D_p}{\lambda})] \quad . \tag{2.17}$$

Various authors have stated slightly different values for the coefficients in Equation 2.17. In this work, the ones from Jung et al. [2012] are in use:

$$A = 2.492$$
$$B = 0.84$$
$$C = 0.43$$

Because of the considerably longer mean free path λ, the non-continuum correction factor $C(D_p)$ is higher for helium than air. For larger particles this factor converges to 1 for both gases. (see Figure 2.3).

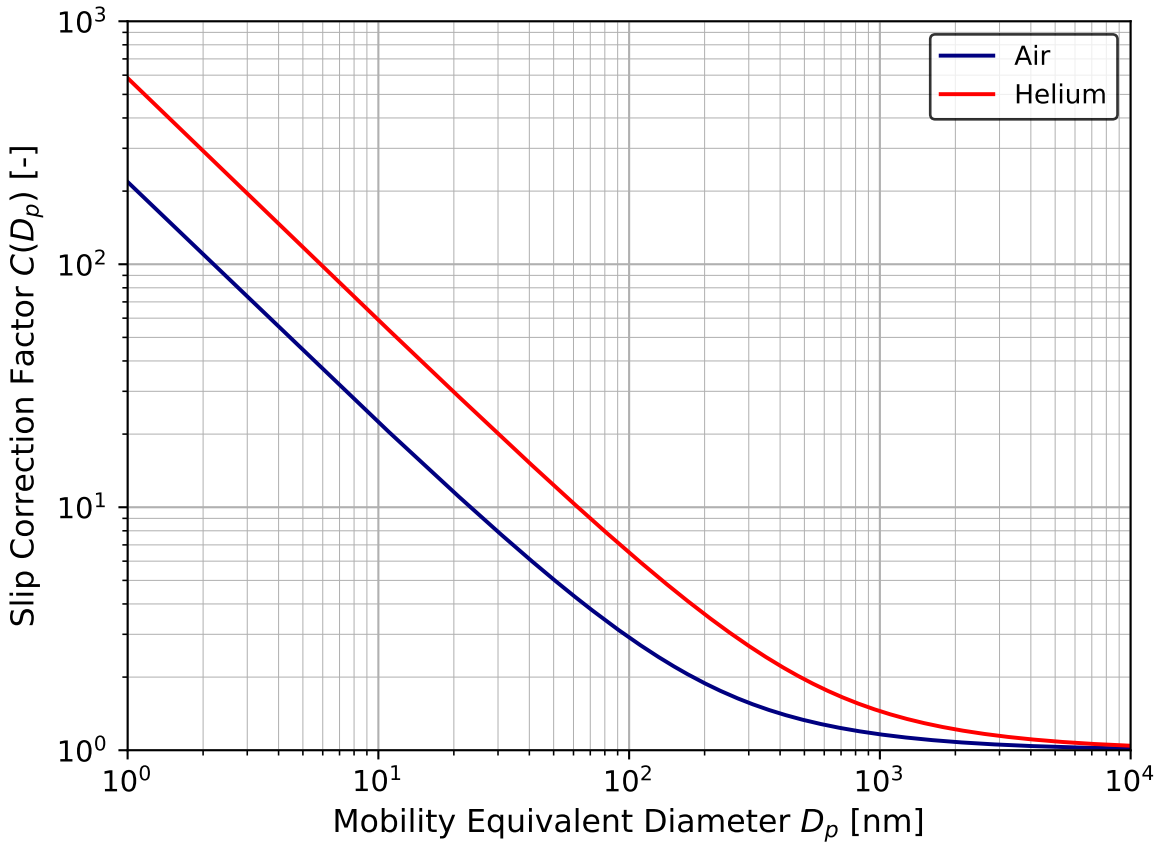

Figure 2.3: Cunningham slip correction factor for air (λ_{Air} = 65.4 nm) and helium (λ_{He} = 191.9 nm). *Mobility equivalent diameter* implies the diameter of a spherical particle with the same electrical mobility as a particle with arbitrary shape. Because of the longer mean free path of helium, the slip correction factor is higher compared to air. For bigger diameters, both functions converge to 1.

Substituting $\vec{F}$ from Equation 2.1

$$\mu = \frac{\vec{v}}{\vec{F}}$$

into Stokes' law (2.16)

$$F = \frac{3 \cdot \pi \cdot \eta \cdot \vec{v} \cdot D_p}{C(D_p)}$$

gives

$$\vec{F} = \frac{\vec{v}}{\mu} = \frac{3 \cdot \pi \cdot \eta \cdot v \cdot D_p}{C(D_p)}$$

Additionally, using Equation 2.3

$$Z = i \cdot e_0 \cdot \mu$$

leads to

$$Z = \frac{i \cdot e_0}{3 \cdot \pi \cdot \eta} \cdot \frac{C(D_p)}{D_p} \quad . \tag{2.18}$$

As a reminder, Equation 2.14 connects the electrical mobility Z with the geometry of the DMA (radii R_{in}, R_{out} and length L) and predefined working conditions (only Q_{sh} when the volumetric flows are ideally symmetrical):

$$Z = \frac{\ln\left(R_{out}/R_{in}\right) \cdot Q_{sh}}{2 \cdot \pi \cdot L \cdot V}$$

Comparing this equation with 2.18 finally results in

$$\boxed{\frac{i \cdot e_0}{3 \cdot \pi \cdot \eta} \cdot \frac{C(D_p)}{D_p} = \frac{\ln\left(R_{out}/R_{in}\right) \cdot Q_{sh}}{2 \cdot \pi \cdot L \cdot V}} \tag{2.19}$$

Equation 2.19 has no analytical solutions for the diameter D_p. For this work, corresponding values were obtained through interpolation methods.

2.4 The Transfer Function of the DMA

A crucial instrument function of the DMA is the so called transfer function Ω. It describes the probability that an aerosol particle with a certain electrical mobility entering the DMA via the inlet will reach the sample flow Q_s under the condition of a given Voltage (Knutson and Whitby [1975]). In this section, losses because of diffusion are neglected. The diffusing transfer function is reviewed in Stolzenburg and McMurry [2008].

As discussed in section 1.2, the electrical mobility is given by Equation 2.13:

$$Z = \frac{\ln\left(R_{out}/R_{in}\right)}{2 \cdot \pi \cdot L \cdot V} \cdot \frac{Q_{sh} + Q_{ex}}{2}$$

Rearranging this equation gives

$$\frac{Q_{sh} + Q_{ex}}{2} = Z \cdot \underbrace{\frac{2 \cdot \pi \cdot L \cdot V}{\ln\left(R_{out}/R_{in}\right)}}_{cons\tan t}$$

Fixing the voltage allows to express the electrical mobility Z exclusively by volume flow rates with

$$Z_{Flow} = \frac{Q_{sh} + Q_{ex}}{2} \quad .$$

Since the aerosol inlet, as well as the outlet are not infinitesimal small, particles within a certain range of electrical mobility ΔZ are able to reach the volumetric flow Q_s .

For the purpose of discussing the transfer function Ω and subsequently the resolution power of a DMA, it is necessary to look upon the boundaries of ΔZ where the upper boundary of ΔZ is denoted as $Z_{Flow}^{\max}$, and the lower boundary as $Z_{Flow}^{\min}$.

Figure 2.4 schematically depicts two particles in the DMA with different electrical mobility. The red particle has the maximal electrical mobility in order to run from the aerosol inlet to the exit slit, whereas the blue particle has the minimal required electrical mobility to be capable to contribute to the sample flow Q_s. It should be mentioned, that the actual pathways of these particles in the DMA is of no relevance.

Using the same method to associate volumetric flowrates to electrical mobilities as in section 2.2, yields in

$$Z_{Flow}^{\min} = Q_{ex} - Q_{ae} = Q_{sh} - Q_s$$

$$Z_{Flow}^{\max} = Q_{ex} + Q_s = Q_{sh} + Q_{ae}$$

As a consequence, the electrical mobility of particles reaching the sample flow Q_s is restricted in the following way:

$$Z_{Flow}^{\min} \leqslant Z_{Flow} \leqslant Z_{Flow}^{\max}$$

$$Q_{sh} - Q_s \leqslant Z_{Flow} \leqslant Q_{sh} + Q_{ae} \quad .$$

- If $Q_s > Q_{ae}$, there are no particles in the remaining flow Q_s - Q_{ae} resulting in dilution of the particle concentration with Q_{ae} / Q_s.
- If $Q_s < Q_{ae}$ it is obvious, that the particle concentration in Q_s cannot exceed the concentration in Q_{ae}, since that would imply, that more particles exit the sampling port, than entering the inlet in the first place.

Ergo, the transfer function Ω becomes

$$\Omega = \min\left(1, \frac{Q_{ae}}{Q_s}\right) \tag{2.20}$$

- If $Q_s = Q_{ae}$, Q_{sh} must be equal to Q_{ex} as well. In this case, the graph of a transfer function is an isosceles triangle. The Full Width at Half Maximum (FWHM) of this function is lower than in case $Q_s > Q_{ae}$ as well as in case $Q_s < Q_{ae}$, which means in effect the highest possible resolution power of the DMA, and therefore ideal flow conditions. Detailed description on these relations is given by Steiner [2011].

In the latter instance, it can be shown, that

$$\frac{FWHM}{Z_{Flow}} = \frac{Q_{ae}}{Q_{sh}} \quad .$$

Introducing a function $\psi(D_p)$ allows to find a link between the actual flow conditions and the particles electrical mobility diameter:

$$\frac{dD_p}{D_p} = \psi(D_p) \cdot \frac{FWHM}{Z_{Flow}} = \psi(D_p) \cdot \underbrace{\frac{Q_{ae}}{Q_{sh}}}_{\beta} \tag{2.21}$$

The fraction Q_{ae} / Q_{sh} is from now on referred to as flow correction β.

Using Equation 2.18 the dimensionless function $\psi(D_p)$ can be found to be

$$\psi(D_p) = \frac{\frac{C(Dp)}{Dp^2}}{\frac{d}{dDp}\left(\frac{C(Dp)}{Dp}\right)} \quad . \tag{2.22}$$

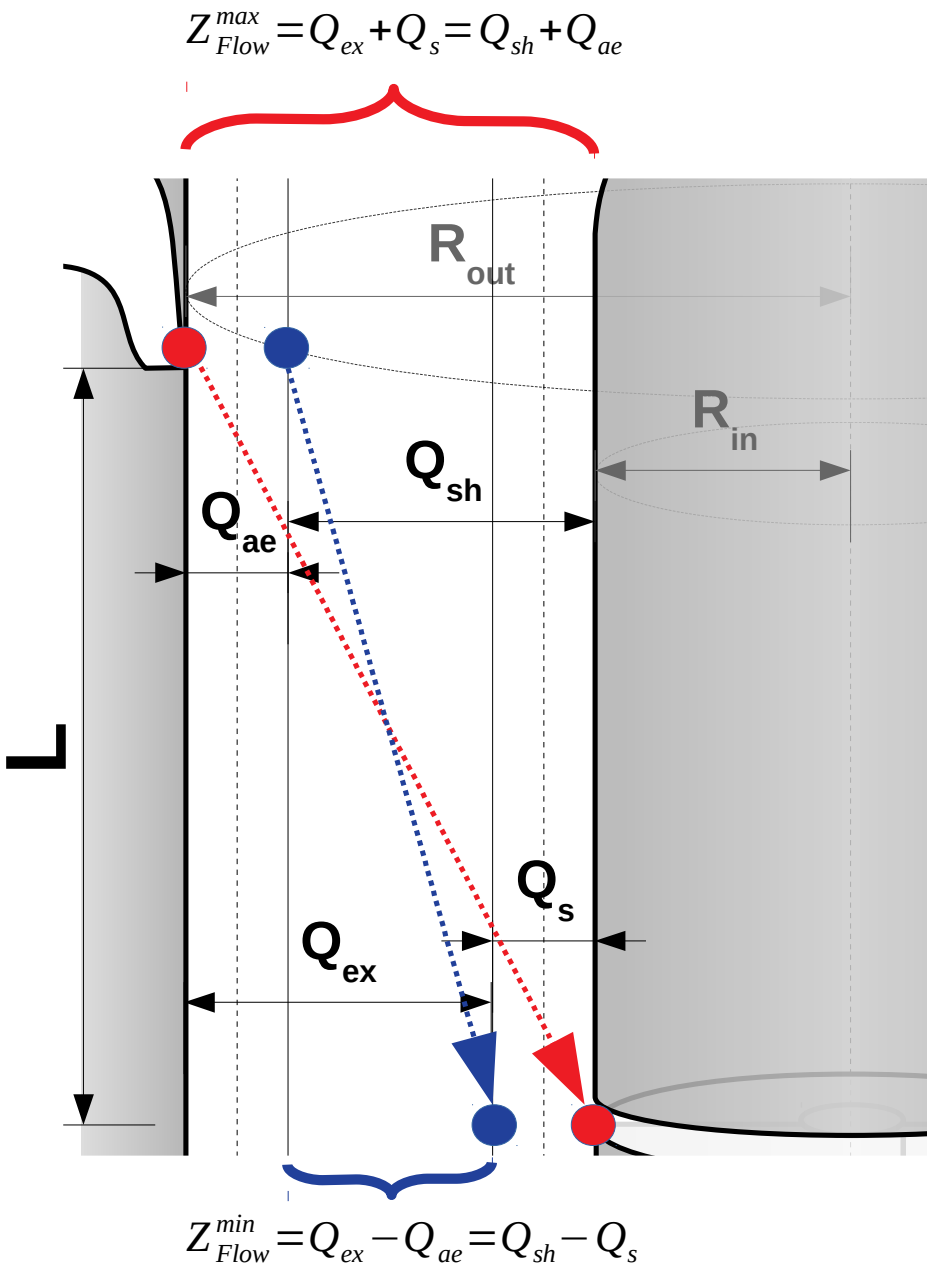

Figure 2.4: Illustration of two particles with different electrical mobility in a DMA. The red one has the maximal, the blue one the minimal electrical mobility in order to contribute to the sample flow Q_s.

Figure 2.5 depicts the function $\psi(D_p)$ using Equation 2.22. As seen in Equation 2.17, the Cunningham slip correction factor $C(D_p)$ is dependent on properties of the carrier gas. This is why, the same applies to $\psi(D_p)$.

For particles in the low nanometer region, $\psi(D_p)$ converges to 0.5. The steepest slope arises for particles with diameters around 1 μm.

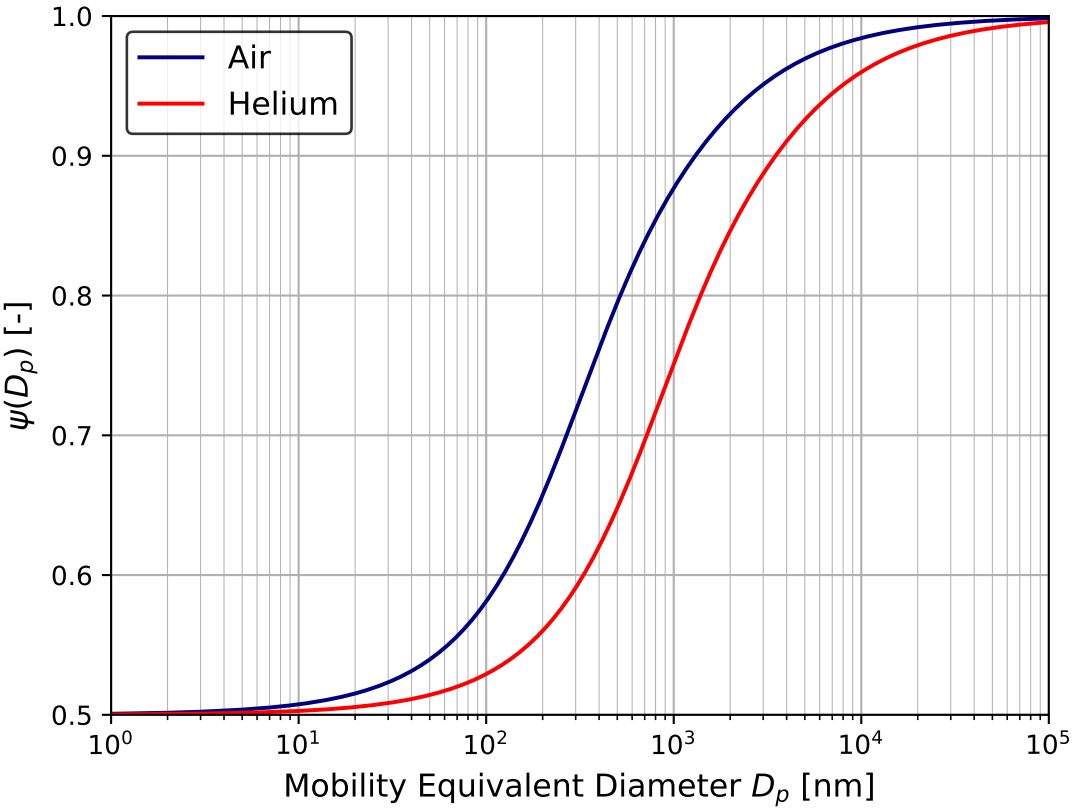

Figure 2.5: Graph of the function $\psi(D_p)$ using Equation 2.22. The difference between air and helium originates from different Cunningham slip correction factors $C(D_p)$ for the different carrier gases. (Equation 2.17, Figure 2.3)

3 Size Parameters of Aerosol Nanoparticles

The size of nanoparticles of an aerosol is decidedly the most important property in terms of its physical characterization.

The diameter (or radius) is only defined for spheres and therefore an inadequate measure for particles of different shapes. For that reason, particle size is defined by the measuring procedure, leading to so called equivalent diameters (John H. Seinfeld [2016]).

In Chapter 2 the diameter of particles is determined by its behavior in an electric field. Hence, the appropriate quantity is the **electrical mobility equivalent diameter**, which is the diameter of a standard-density sphere with the same electrical mobility as the particle under consideration ([John H. Seinfeld, 2016, p.431]).

Dependent on the measuring procedure, a number of additional equivalent diameters are defined. For instance ([John H. Seinfeld, 2016, p.426-431]):

Volume equivalent diameter
: Diameter of a spherical particle with the same volume

Mass equivalent diameter
: Diameter of a spherical particle with the same mass

Aerodynamic equivalent diameter
: Diameter of a sphere with the same terminal settling velocity

Unless clearly mentioned, in this work only the electrical mobility equivalent diameter comes up.

3.1 Size Distributions and Particle Size Statistics

Ordinarily, aerosols are polydisperse with particle sizes spread over at least two orders of magnitude ([Hinds, 1999, p.75]). For that reason, in order to characterize the corresponding size distributions statistic, mean values are used. In general, the size distribution of aerosol particles is the distribution of any property of the particles as a function of size.

In Figure 3.1, simplified representations of discrete frequency size distributions of uniformly distributed data are depicted. The idea is to assign particles into bins according to their

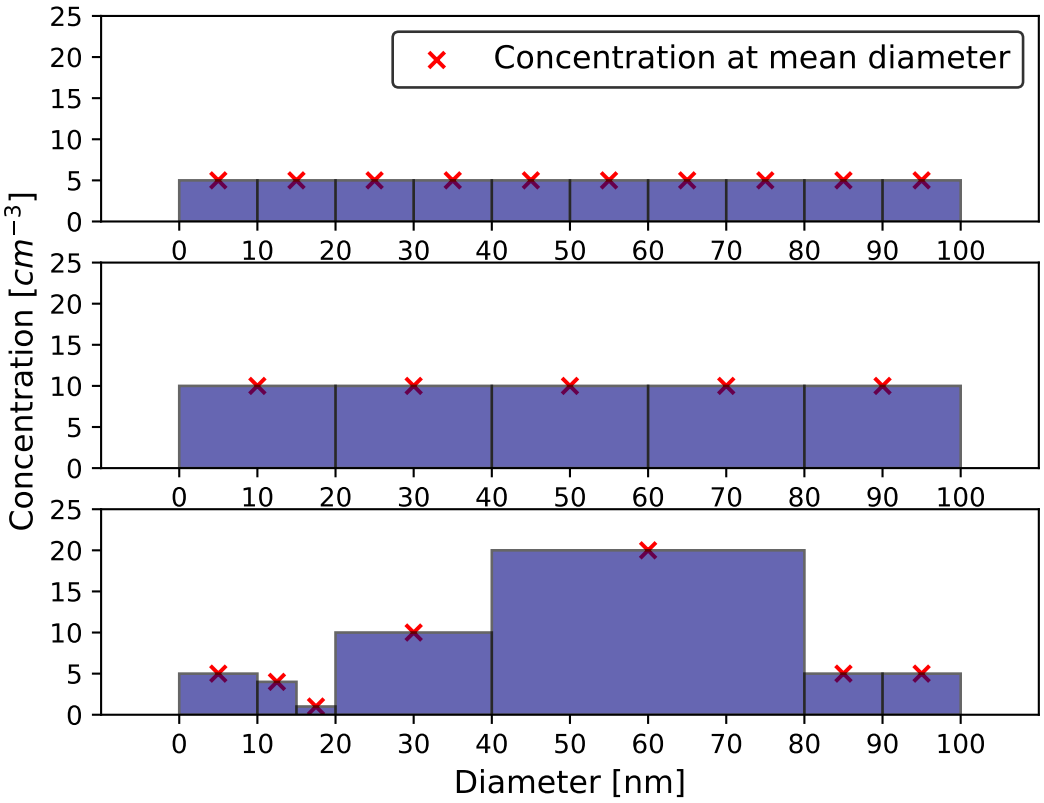

Figure 3.1: Three histograms of the same uniformly distributed data. It demonstrates, that frequency distribution functions are not comparable because of possibly different bin widths.

diameter. The respective frequencies of the particles in each interval are plotted on the Y-axis. It is obvious, that an adjustment of the diameter intervals, which can occur for example due to a change in the instrument, result in a change of the frequencies as well. In the topmost histogram in Figure 3.1, the bin width is halved compared to the histogram in the middle, resulting in half the frequency. The bottom panel depicts the same (uniformly distributed) frequency distribution with arbitrary changed diameter intervals.

This simple example demonstrates, that bin counts, and in further consequence, frequency distribution functions are not comparable due to possibly different bin sizes.

In order to compare the shape of size distributions, one has to normalize to its total number. In Figure 3.2 two exemplary plots of the same set of data are shown. The size distribution is obtained by joining the bin mid-points. Because different bin widths are chosen, the shapes of these frequency size distributions are diverse. That problem is resolved, when each bin height is divided by its bin width, as depicted in Figure 3.3. The number concentration of the dN/dD_p distribution is proportional to the area of each bin. Obviously, the smaller the bin sizes, the better the accordance of the distributions.

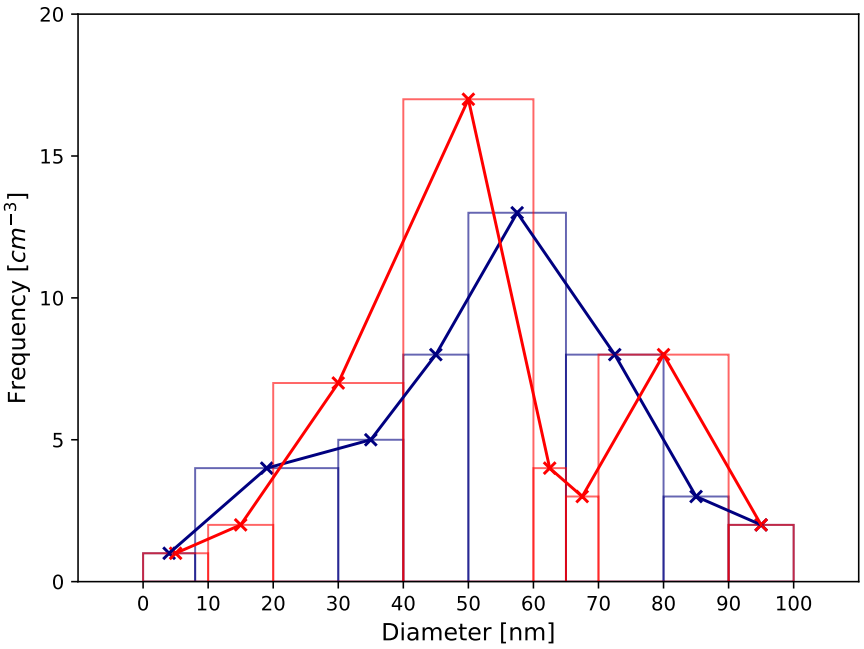

Figure 3.2: Although the same exemplary data is in use, different bin widths implicate different size distributions, obtained by joining the mid-points of the bins.

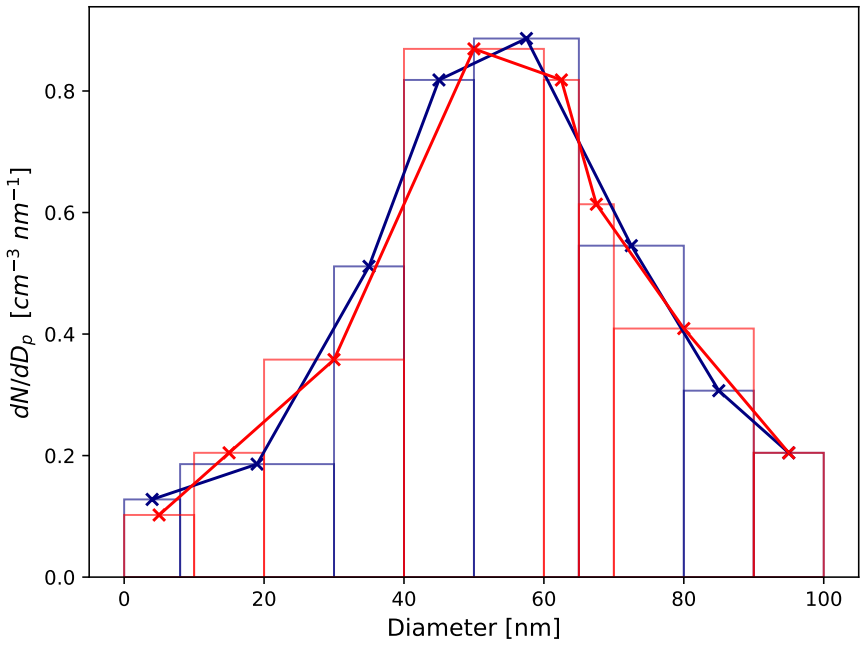

Figure 3.3: Differential particle concentration distributions obtained by normalizing the particle number by the range of particle diameters of the bin. The normalized concentration values on the Y-axis are independent of the bin width.

3.2 The Lognormal Distribution

As discussed in the previous section, the higher the resolution of the measuring instrument, the smaller the bin widths, the smoother is the resulting size distribution. For infinitesimal bin sizes, one would obtain a continuous function, the so called Probability Density Function (PDF).

The widely used PDF of the Gaussian distribution is not suitable to characterize particle size distributions very well. Not alone would it mathematically allow negative values for particle diameters, but rather because most aerosols exhibit a skewed distribution function ([Hinds, 1999, p.91]). This skewness is due to the fact, that most aerosol size distributions have a long tail to the right, at bigger diameters. Additionally, as previously mentioned, polydisperse aerosol-sizes spread over at least two orders of magnitude ([Hinds, 1999, p.75]), so a logarithmic representation in the diameter is preferable.

The most suitable, and therefore the most common aerosol size distribution, is found to be the lognormal distribution. If y is a normally distributed random variable, then $x = e^y$ is lognormal distributed.

The PDF of the lognormal distribution is given by:

$$f(x, \mu, \sigma) = \frac{1}{x \cdot \sigma \cdot \sqrt{2\pi}} e^{-\frac{(\ln x - \mu)^2}{2 \cdot \sigma^2}} \qquad \begin{array}{l} \mu \in (-\infty, +\infty) \\ \sigma > 0 \\ x \in (0, +\infty) \end{array} \tag{3.1}$$

The parameters μ and σ are the location and scale parameters for the corresponding normally distributed variable y.

It should be noted, that there is no physical reason as to why the lognormal distribution is appropriate for aerosol size distributions. It is just empirically found to be the best fit for single source aerosols ([Hinds, 1999, p.91]).

As well es every other distribution, the lognormal PDF is characterized by statistical means. In consequence of the unsymmetrical appearance when plotted on an arithmetic X-axis, the statistical properties Mode, Median and Mean, are (contrary to the gaussian distribution) not identical.

The **mode** is the most frequent diameter of the aerosol distribution, the **median** is equal to the geometric mean, and is defined as the diameter for which fifty percent of the particles are bigger, as well as fifty percent are smaller than this number. The expected value or the arithmetic mean is usually the **mean** of the lognormal distribution. The geometric standard deviation (**GSD**) of the lognormal distributed variable x is labeled σ_{GSD}. Table 3.1 exhibits these properties with their corresponding formulas.

Figure 3.4 depicts examples of the lognormal PDF. In both panels the same three functions are plotted. In the upper one with arithmetic X-axis, in the bottom one with logarithmic scale, where it appears, in consequence of its definition, gaussian shaped. The calculated mode (red line), median (blue), and mean (orange) are marked as well. They are found to be 0.21 (mode), 1 (median) and 2.18 (mean) for an exemplary lognormal distribution with μ=0 and σ=1.25.

Lognormal Distribution	
Property	Formula
Mode	$e^{\mu-\sigma^2}$
Median	e^{μ}
Mean	$e^{\mu+\frac{\sigma^2}{2}}$
σ_{GSD}	e^{σ}

Table 3.1: Statistical means of the Lognormal Distribution

As a general rule of the lognormal distribution ([Hinds, 1999, p.81]):

mode < median < mean

Based on all considerations of this chapter, aerosol particle number size distributions are usually diagrammed with logarithmic X-axis (particle diameter D_p) and logarithmic Y-axis ($dN/dln(D_p)$).

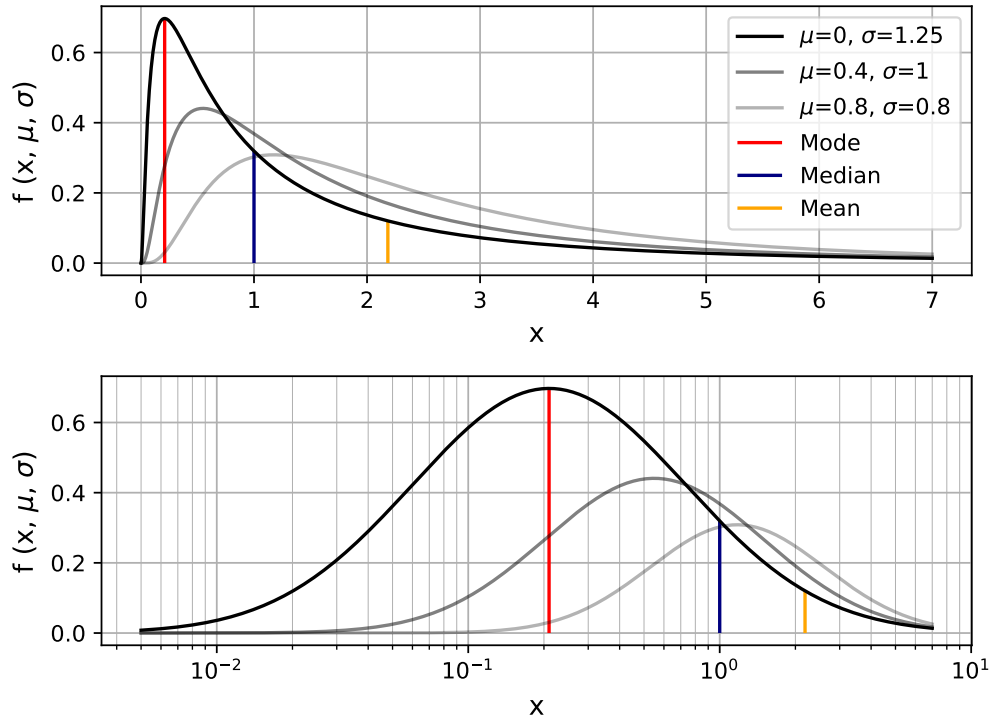

Figure 3.4: Exemplary lognormal distributions with corresponding mean values. The upper panel is plotted with arithmetic X-axis, the bottom one on a logarithmic scale.

4 Charging and Detection of Aerosol Nanoparticles

Differential mobility analysis, as discussed in Chapter 2, is ordinarily used to calculate the particle number size distribution. For this purpose one has to ensure, that the particle charge states are well known. Subsequent to electrical mobility analysis, information about the particle number is achieved by particle counters such as the Condensation Particle Counter (CPC) or the FCE.

4.1 Particle Charging

The charge state of an aerosol is defined by its initial charge distribution, as well as its exposure to ions in the carrier gas. Almost all aerosols have some level of initial electric charge (Whitby and Liu [1967]). Since it is in general unknown, it has to be changed to a well known charge distribution. There are several ways to accomplish this, for example through corona discharging (Chang et al. [1991], Hernandez-Sierra et al. [2003]) or flame charging (Burtscher [1992]). However, throughout this work the most common charging mechanism was in use, namely diffusion charging.

Broadly speaking, the aerosol particles collide with ions, whereby the charges carried by these ions are conveyed to the particles. This cloud of ions is comprehensive (almost) neutral, but it consists of a large number of ions with negative and positive polarity. The generation of these ions is achieved by exposure of the carrier gas to ionizing radiation. Either a radioactive source, like ^{85}Kr, ^{210}Po, ^{63}Ni or ^{241}Am, or soft X-rays can serve as an origin of this radiation (Tigges et al. [2015]). A model to describe this bipolar charge equilibrium is provided by Fuchs [1963]. Since the Fuchs model has to be solved numerically, Wiedensohler [1988] provided an analytical equation (see Equation 4.1) which approximates the Fuchs model:

$$\alpha(D_p, i) = 10^{\left[\sum_{j=0}^{j=5} a_j(i)\left(\log_{10} D_p\right)^j\right]} \quad . \tag{4.1}$$

$\alpha(D_p, i)$ provides the fraction of particles with diameter D_p that carry i elementary charges.

The approximation coefficients $a_j(i)$ are summarized in Table 4.1. It is important to remark, that the diameter D_p needs to be entered in [nm].

	Number of elementary charges i				
$a_j(i)$	-2	-1	0	1	2
a_0	-26.3328	-2.3197	-0.0003	-2.3484	-44.4756
a_1	35.9044	0.6175	-0.1014	0.6044	79.3772
a_2	-21.4608	0.6201	0.3073	0.48	-62.89
a_3	7.0867	-0.1105	-0.3372	0.0013	26.4492
a_4	-1.3088	-0.1260	0.1023	-0.1553	-5.748
a_5	0.1051	0.0297	-0.0105	0.0320	0.5049

Table 4.1: Wiedensohler Approximation coefficients $a_j(i)$, corrected by Flagan [2008].

According to Wiedensohler [1988], this approximation is valid for the following size ranges:

$$1\,nm \leqslant D_p \leqslant 1000\,nm: \quad i = -1, 0, 1$$
$$20\,nm \leqslant D_p \leqslant 1000\,nm: \quad i = -2, 2$$

Particles with diameters up to 70 nm, do not carry more than two elementary charges. To calculate the fraction of particles which got transferred three or more elementary charges, one can use an equation which was initially derived from Gunn and Woessner [1956].

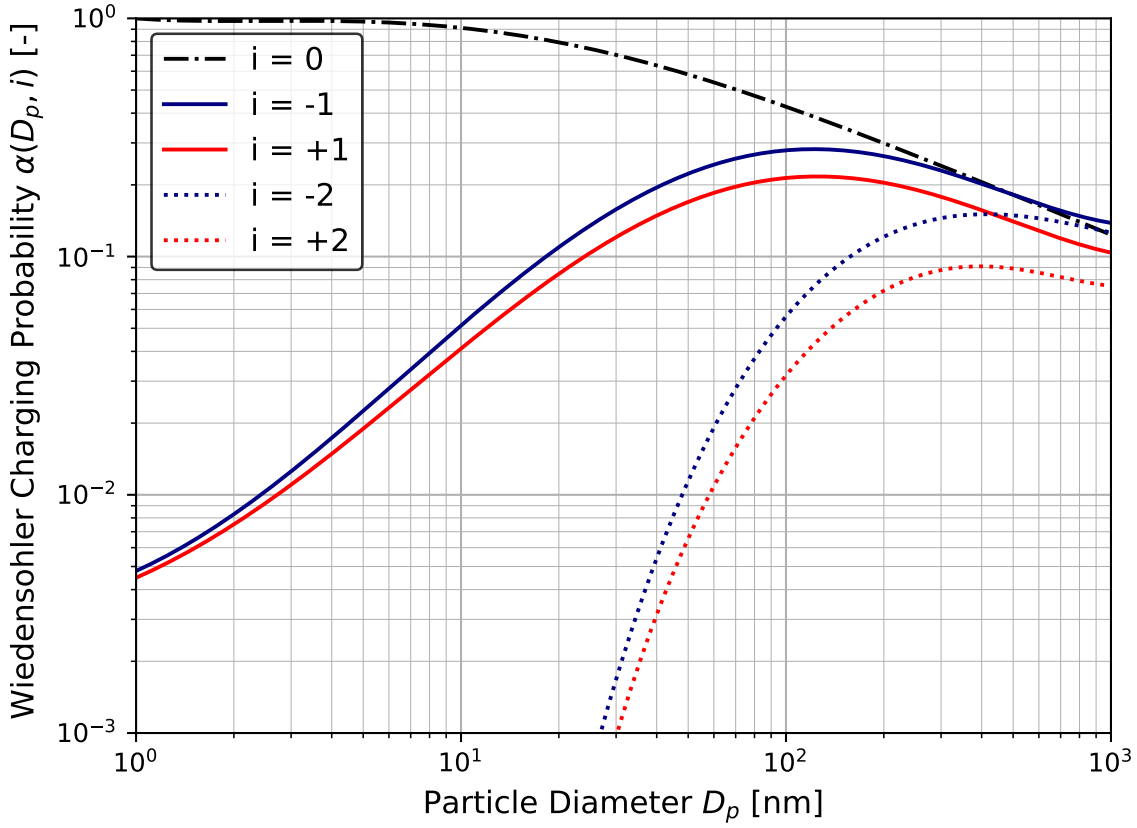

Figure 4.1: Charge distribution for bipolar charging using Equation 4.1 as introduced by Wiedensohler [1988] and corrected by Flagan [2008].

Figure 4.1 depicts the Wiedensohler [1988] charge distribution from Equation 4.1. It illustrates, that downstream the aerosol neutralizer, most of the particles on the smaller side carry no charge at all. For instance, considering particles with a diameter of 10 nm, 91.2 % are not charged, whereas only 4.1 % have charge state of +1 and 5.1 % carry one negative charge. In other words, around 95 % of all nanoparticles of this size cannot be characterized in terms of their electrical mobility as discussed in Chapter 2. That implies, that the charging probability $\alpha(D_p, i)$ has to be appropriately taken into consideration, when it comes to computation of the number size distribution of aerosol nanoparticles.

Within this work, a *TSI Advanced Aerosol Neutralizer Model 3088* has been operated. It is a bipolar diffusion charger, that uses low energy (< 9.5 keV) soft X-rays for the ionization of gas molecules.

4.2 Counting Aerosol Nanoparticles

Detection of submicron airborne particles can be achieved with electrostatic techniques like operating Faraday Cup Electrometers (FCE's), or with Condensation Particle Counters (CPC's). The latter use heterogeneous condensational growth to sizes, where they can be detected by optical means. FCE's measure the charges carried by the particles to infer their number.

4.2.1 Condensation Particle Counter

The idea of supersaturating air, and in further consequence condensate vapor on nanoparticles in order to grow them to a certain size that allow optical detection, was introduced by Aitken [1888]. After considerable improvements, the first commercially-produced Condensation Nucleus Counter (CNC), the TSI Model 3020 was presented by Agarwal and Sem [1980]. Over the decades, three different techniques to supersaturate the condensing vapor were applied. Aitken used a pump for adiabatic expansion of water saturated air. This approach was further developed by various authors, for example Nolan and Pollak [1946]. An other method is to mix cold and hot saturated vapors to reach supersaturation. This two-flow mixing CNC was introduced by Kousaka et al. [1982]. Nevertheless, nowadays most apparatuses use diffusional, alcohol-based, steady-flow CNC's established by Bricard et al. [1976] where the sample is saturated with alcohol vapor, when it passes over a heated reservoir of the working fluid. Further, it flows into a cooled chamber, where the alcohol condenses on the particles.

It should be mentioned, that different terminologies have been adopted by various authors. Some use "Aitken Nuclei Counters" for water based instruments and CNC for apparatuses with different working fluid. In recent years CPC has begun to emerge and as it is less ambiguous, it is from now on used in this thesis.

In this work, a butanol based CPC was in use, the TSI Ultrafine Condensation Particle Counter (UCPC) Model 3776. Figure 4.2 depicts its flow schematic. It can be operated in high flow (1.5 L/min) or low flow (0.3 L/min) mode. High flow mode brings the sample faster

in the CPC and therefore reduces diffusional losses, whereas the low flow mode allows to measure a wider size range when it is operated as a detector in a DMPS.

In both cases, the incoming flow is split up into a sheath flow and a sample flow which add up to 0.3 L/min, that is ensured by a critical orifice. When the CPC is operated in high flow mode, the excess 1.2 L/min bypasses the entire sensor system (see Figure 4.2).

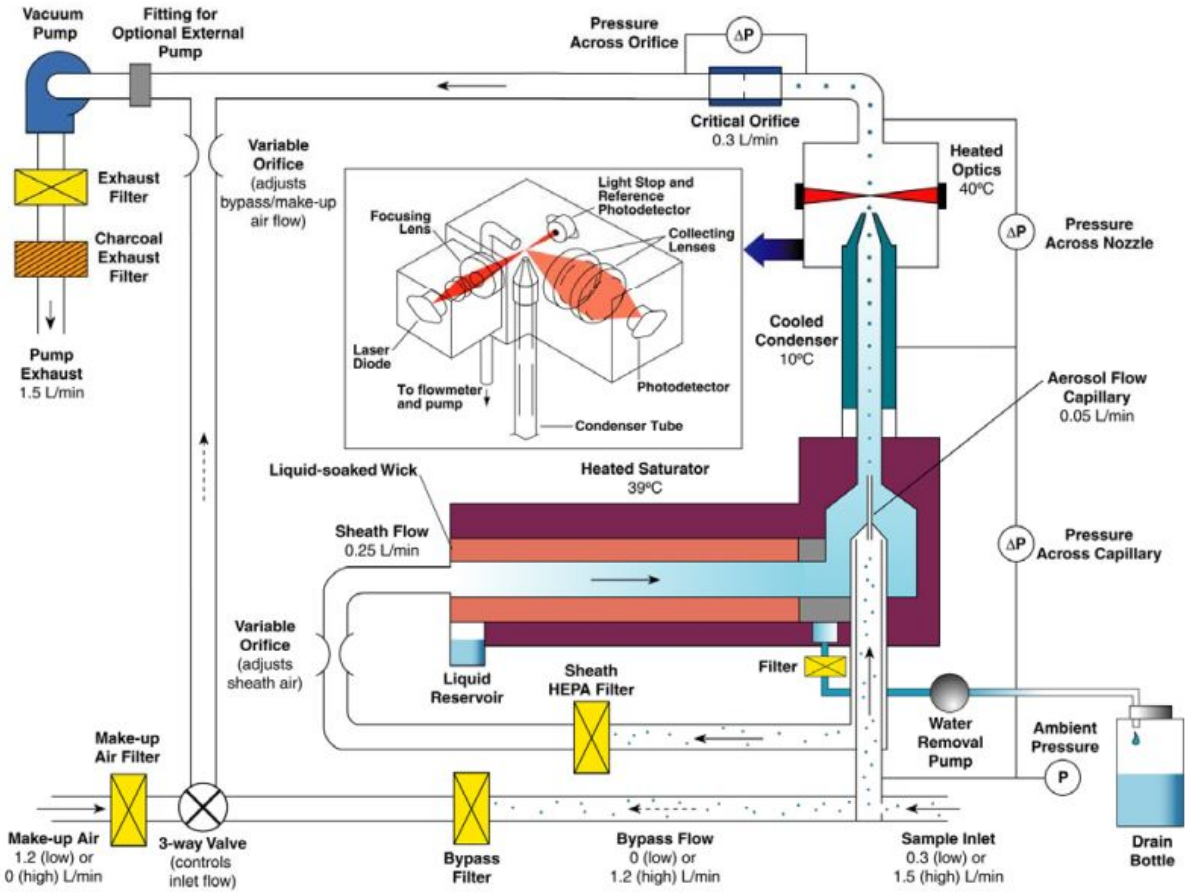

Figure 4.2: Model 3776 UCPC Flow Shematic, taken from its manual.

The 0.25 L/min sheath flow is filtered and streams into the heated section, where it is saturated with evaporated butanol, the working fluid of the Model 3776 CPC. The remaining 0.05 L/min sample flow is injected in a vertical condenser, where it joins the saturated sheath flow and hereinafter both undergo cooling. This is where the vapor becomes supersaturated and condenses onto the particles under investigation. These droplets grow to a size of about 10 to 12 micrometers, which allows optical detection in the subsequent laser optics.

When the CPC was operated with helium instead of air as carrier gas, to prevent homogeneous nucleation, the saturator temperature was lowered from 39° C to 35° C, the condenser temperature was set to 15° C instead of 10° C. The likewise changed volumetric flow rates were adjusted via variable orifices in the device verified with a bubble flowmeter (Gilian Gilibrator-2).

4.2.2 Faraday Cup Electrometer

The usage of Faraday Cup Electrometers (FCE's) as particle detectors has proven to be successful over the last decades. Modern FCE's build upon the development of Whitby and Clark [1966], although its keynote is well known way longer (e.g. Zeleny [1929]).

Since aerosol particles need to be charged to be classified in the DMA, these charges can be further used to detect them. Figure 4.3 shows a schematic illustration of the FCE. It consists of a metal housing where a High Efficiency Particulate Air (HEPA) filter is mounted on insulating material (e.g. Teflon). Unipolar aerosol charges that are collected on the filter result in a change of the electrical potential of the cup. Ultra-low compensation currents (less than 10^{-12} A (Intra and Tippayawong [2014])) are a direct measure of the number concentration of the aerosol particles N:

$$N = \frac{I_{FCE}}{e_0 \cdot Q_s \cdot i} \tag{4.2}$$

N is the total number concentration, e_0 is the elementary unit of charge ($1.602 \cdot 10^{-19}$ C), Q_s the volumetric flow rate into the FCE and i the number of charges on the particles.

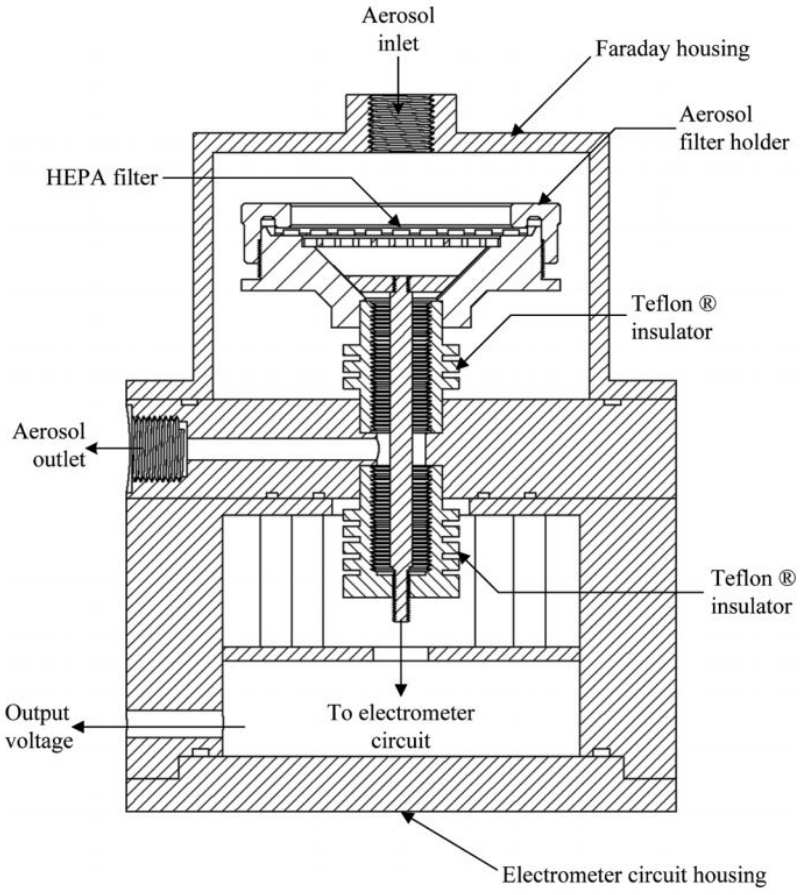

Figure 4.3: Schematic diagram of a Faraday Cup Electrometer. This Figure is taken from Intra and Tippayawong [2014]

As seen in Figure 4.1, the probability that particles smaller than around 40 nm carry more than one charge is less than one percent. For bigger particles, multiple charges have to be considered, and therefore more deliberations are necessary.

Due to different measurement techniques, CPC's and FCE's have diverse limitations. CPC's are restricted on the minimal particle size that can be activated. Typical counting efficiencies of several CPC's, including the TSI Model 3776 can be found in Hermann et al. [2007]. FCE's on the other hand, are mainly restricted to the electrical sensitivity of the electrometer, which results in a lower limit in the range of a few hundred particles that are detectable. Consequently, FCE's are likely used for measurements of high particle concentrations, especially in laboratory conditions, whereas CPC's are often more suitable for atmospheric measurements.

5 Differential Mobility Particle Sizing

Differential mobility particle sizing is a technique for measurement of submicron aerosol size distributions. The Differential Mobility Particle Sizer (DMPS) couples a DMA (see Chapter 2) with a particle counter as described in section 4.2. This approach allows to measure small nanoparticles down to about 1 nm (Intra and Tippayawong [2008], Winklmayr et al. [1991], Reischl et al. [1997]). When scanning the voltage of the DMA step-wise through the full electrical mobility range of particles under investigation, the number mobility distribution can be measured.

5.1 Setup of the Nanoparticle Generator and DMPS

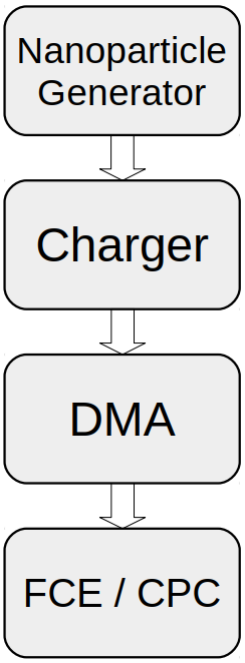

Figure 5.1: Nanoparticle Generator and DMPS Setup

For this work, a DMPS was used to obtain raw data about number and size of the generated nanoparticles, that further can be computed to number size distributions.

As a first step, a controlled flow of particle-free carrier gas streams into the generator. Subsequently, the generated nanoparticles are neutralized in an aerosol charger, as specified in section 4.1, and thereupon, the DMA separates the particles according to their electrical mobility (see Chapter 2). The sheath flow (Q_{sh}) of the DMA is a closed loop. The exhaust flow Q_{ex} is drawn into a HEPA filter, a silica gel diffusion dryer and active carbon before it is pumped as sheath flow into the DMA again. This provides a dry and particle-free Q_{sh} stream.

Constant flows are ensured with critical orifices. At a certain fraction between upstream and downstream pressure of the orifice, gas velocity in a constriction inside the orifice attains the speed of sound. This results in a chocked flow, for which a continuing decline in pressure downstream the orifice does not result in an increase of the flow through the device [Kulkarni et al., 2011, p. 468].

Generally, all flows have to be checked before starting the measurements. One has to verify, that the DMA operates symmetrically ($Q_{sh} = Q_{ex}$, $Q_s = Q_{ae}$, see Section 2.4), has to know exact values for the sheath flow for calculating the mobility equivalent diameter (Equation 2.19), as well as flow rates into the particle counter Q_s (Equation 4.2). All flows were checked before and after the measurement.

Downstream the DMA the particles are counted in an FCE or CPC which are specified in Section 4.2. For this work, the DMPS was operated with an electrometer. To avoid any excess pressure in the system, an overflow through a HEPA filter was provided.

Potential drawback of measuring number size distributions with a DMPS is, that it is not sensitive to different particle shapes. As discussed in Chapter 2, nanoparticles are analyzed according to their electrical mobility. Additionally, because of the step-wise scanning of the DMA-voltage and respective counting, the time resolution is limited.

To take the problem of unknown particle shapes into account, samples of most generated nanoparticles were taken for further investigation via Transmission Electron Microscopy (TEM) utilizing the TSI Nanometer Aerosol Sampler Model 3089. This method permits comprehensive analysis of nanoparticle properties such as shape, crystallinity and composition (Dixkens and Fissan [1999]). According to TSI, this apparatus allows to sample 2 nm to 100 nm particles onto TEM grids. Inside the sampler, an electrode is installed on which a fixed voltage between 500 V and 10 kV can be applied. The corresponding electric field draws charged particles that are inserted by an aerosol inlet (0.2 to 2.5 L/min) onto the middle of the electrode, where a TEM grid is mounted with adhesive tape. After sampling times between 15 minutes and 1 hour, the grid can be removed for analysis with an electron microscope. In this work, a PHILIPS CM 200 transmission electron microscope was used, that allowed not only imaging, but also chemical analysis of the sample by Energy Dispersive X-ray Spectroscopy (EDX).

5.2 Operating the DMPS with Helium

Operating a DMPS with a carrier gas different than air entails a number of challenges.

All flows have to be measured with a bubble flow meter (Gilian Gilibrator-2), because the thermal mass flow meters, that were used for air, could not be calibrated for helium. Besides that, the constant volumetric flow rate downstream a critical orifice is a function of gas density, so using helium as carrier gas instead of air significantly influences the flow conditions and therefore the flow rates downstream the orifice. Moreover, care must be taken that the system in its entirety is filled with helium before the measurement is started. In order to speed up this process, additional helium was pumped into the DMA loop.

Particular attention must be paid to the critical voltage at which a breakdown in a DMA may occur. Paschen [1889] found, that this breakdown voltage between two electrodes is heavily dependent on the gap length as well as the mean free path of the gas in between. Since the latter is way longer in helium than in air, (λ_{Air} = 65.4 nm, λ_{He} = 191.9 nm see Section 2.3) in order to avoid electrical breakdowns, a maximal DMA voltage of 1050 V was applied (compared to 10 kV in air for a DMA with gap length of 6.6 mm). This significantly reduces the maximal size of nanoparticles, that are detectable with a certain DMA.

Given the importance of cooling regarding nanoparticle generation, it has to be considered, that diverse gases have different thermal conductivities. The value for helium (0.152 $\frac{W}{m \cdot K}$ at 300 K) is almost six times higher than for air (0.026 $\frac{W}{m \cdot K}$ at 300 K)(Vargaftik and Yakush [1977], Lemmon and Jacobsen [2004]). Accordingly, when using helium as carrier gas this results in a substantially faster cooling of the aerosol leaving the nanoparticle generator. Furthermore, a change in charging efficiency needs to be taken into account ([Baumgartner, 2018, p.67])

5.3 Calculation of the Number Size Distribution

As discussed in Section 3.2, the number size distribution of aerosol particles is commonly denoted as $\frac{dN}{d \ln Dp}$. Before these particles are detected in a FCE or CPC (see Section 4.2), they need to be charged (Section 4.1) and analyzed in a DMA (Chapter 2). Because of the physical principles which all these instruments are based on, only a fraction of particles that are generated can be detected. Hence, so as to obtain the size distribution of the initial present particles $\frac{dN}{d \ln Dp}$, appropriate inverse-calculation of the measured raw data is needed.

The following inversion factors have to be considered:

Charging probability $\alpha(D_p, i)$

As discussed in Section 4.1, most of the particles downstream the charging device carry no charge at all (see Figure 4.1). Besides that, in order to be analyzed in the DMA, the particle has to have the right polarity.

The charging probability $\alpha(D_p, i)$ is calculated with Equation 4.1 provided by Wiedensohler [1988].

FLow correction β

The inversion factor $\beta = Q_{ae}/Q_{sh}$ takes the dilution of the aerosol flow rate Q_{ae} by the sheath flow Q_{sh} in the classification channel of the DMA into account.

$\psi(D_p)$ **function**

The dimensionless function $\psi(D_p)$ (Equation 2.22) as discussed in section 2.4 has to be taken into account as well. Since it contains the carrier gas dependent Cunningham slip correction factor (Equation 2.17, Cunningham [1910]), $\psi(D_p)$ changes with the carrier gas as well (see Figure 2.5)

Diffusion losses $\delta(D_p)$

The diffusion of aerosol particles to the walls of the tubing they flow through have to be appropriately taken into consideration. Under the assumptions of a laminar flow through a circular tube, the fraction of incoming particles that exit, is a function of the deposition parameter μ ([Hinds, 1999, p.163]):

$$\mu = \frac{D \cdot L}{Q} \tag{5.1}$$

Therein L is the length of the tube, Q is the volumetric flow rate, and D the diffusion coefficient. The theory of diffusion is based on findings of Einstein [1905] and Smoluchowski [1906]. Including Stokes' law (Equation 2.15) gives the Stokes-Einstein relation for the diffusion coefficient ([Hinds, 1999, p.153]):

$$D = \frac{k_B \cdot T \cdot C(D_p)}{3\pi \cdot \eta \cdot D_p} \tag{5.2}$$

where k_B is the Boltzmann constant $1.38 \cdot 10^{-23} \frac{N \cdot m}{K}$, $C(D_p)$ the Cunningham slip correction factor (Equation 2.17), and η the viscosity of the carrier gas.

Therewith, the fraction of particles that are lost due to diffusion result in ([Hinds, 1999, p.163]):

$$\begin{aligned} \delta = \frac{n_{out}}{n_{in}} &= 1 - 5.5 \cdot \mu^{2/3} + 3.77 \cdot \mu \quad for \quad \mu < 0.009 \\ \delta &= 0.819 \cdot e^{-11.5 \cdot \mu} + 0.0975 \cdot e^{-70.1 \cdot \mu} \quad for \quad \mu \geqslant 0.009 \end{aligned} \tag{5.3}$$

A remarkable fact is, that the loss of particles in a tube does not depend on the tube diameter at all ([Hinds, 1999, p.163]).

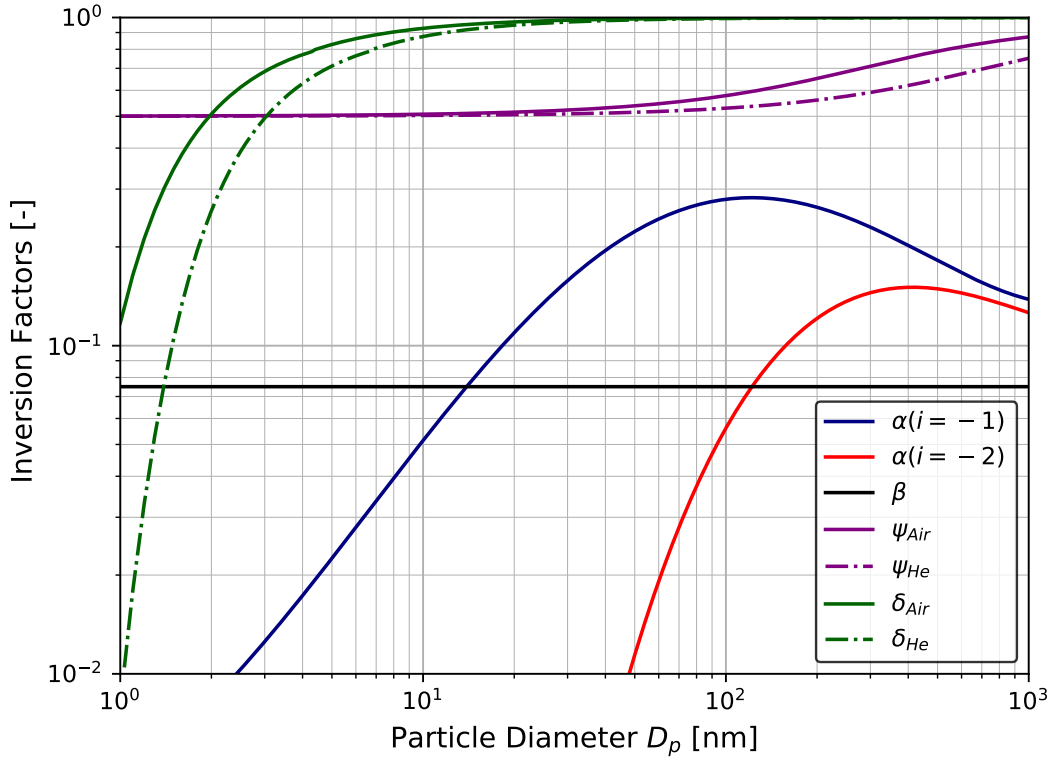

Figure 5.2: Inversion Factors for particles with diameters within 1nm and 1μm in helium and air.

Figure 5.2 sums up all discussed inversion factors between 1nm and 1μm for both carrier gases considered in this study.

$\psi(D_p)$, and $\delta(D_p)$ are depicted for helium and air as carrier gases. The latter is calculated with Equation 5.3 for an exemplary tube length L = 1 m and a volumetric flow rate of 2 L/min at 293.15 K and 1 atm. The values for the mean free path (λ_{Air} = 65.4 nm and λ_{He} = 191.9 nm) are taken from Katz et al. [2011] and Jennings [1988] with according viscosities of η_{Air} = 1.8325· 10^{-5} Pa· s (Birge [1945]) and η_{He} = 1.96 · 10^{-5} Pa · s (Kestin and Leidenfrost [1959]). For calculating β, Q_{ae}= 1.5 L/min and Q_{sh}= 20 L/min are used.

For the case of singly charged particles only, the number size distribution $\frac{dN}{d\ln Dp}$ from the raw data N_{raw} is obtained by dividing it with the inversion factors:

$$N_{raw} = \frac{dN}{d\ln D_p} \cdot \alpha(D_p, 1) \cdot \beta \cdot \gamma(D_p) \cdot \delta(D_p)$$

$$\frac{dN}{d\ln D_p} = \frac{N_{raw}}{\alpha(D_p, 1) \cdot \beta \cdot \gamma(D_p) \cdot \delta(D_p)} \tag{5.4}$$

In the event of an FCE is used for detecting (see Equation 4.2) it results in:

$$\frac{dN}{d\ln D_p} = \frac{I_{FCE}}{Q_{ae} \cdot e_0 \cdot \alpha(D_p, 1) \cdot \beta \cdot \gamma(D_p) \cdot \delta(D_p)} \tag{5.5}$$

with a computed diameter D_p by use of Equation 2.19 from Section 2.3:

$$\frac{i \cdot e_0}{3 \cdot \pi \cdot \eta} \cdot \frac{C(D_p)}{D_p} = \frac{\ln\left(R_{out}/R_{in}\right) \cdot Q_{sh}}{2 \cdot \pi \cdot L \cdot V}$$

Due to the size range of the nanoparticles considered in this work, only singly- and doubly charged particles were taken into account.

6 Generation of Aerosol Nanoparticles

Particles in the size range of 1-100 nm are commonly called nanoparticles [Kulkarni et al., 2011, p. 5]. Because of the small size, their physical and chemical properties may vary significantly from those of the respective bulk material (Karlsson [2004]). This is why, regarding aerosol technology, proper measurements concerning size and controlled generation of these nanoparticles gain considerable attention.

Dependent on requested size and composition, nanoparticles can be synthesized in various ways. In general, they can be generated either in the liquid or in the gas phase. The former includes exemplary Electrohydrodynamic Atomization (EHDA), also called electrospraying. Under this method, monodisperse droplets are generated via electrical forces. Ensuing evaporation of the liquid leads to the emergence of solid nanoparticles (Biskos et al. [2008], Grace and Marijnissen [1994], Taylor [1964]). The other route is nanoparticle generation through gas-to-particle conversion, where the material under investigation sublimates or evaporates. Subsequent nucleation and coagulation forms the nanoparticles.

In accordance with standard aerosol textbooks like Hinds [1999] or Kulkarni et al. [2011], the following definitions are used in this thesis:

Sublimation
: A phase transition of a material from the solid directly to the gas phase, without a transitional liquid phase.

Nucleation
: The initial step in forming clusters of molecules of a critical size, that are allowed to grow further via other processes, is called nucleation. One distinguishes between homogeneous and heterogeneous nucleation. The former is the formation of particles induced by a supersaturated vapor only. Supersaturation occurs, when the saturation ratio, which is the ratio of the partial vapor pressure of a system to its saturation pressure of vapor for a given temperature, exceeds 1. In contrast, heterogeneous nucleation utilizes existing condensation nuclei. Homogeneous nucleation requires supersaturation values of 2-10, whereas in the latter case, lower supersaturation of only a few percent is required, which can be further lowered with soluble seed particles like salt.

Condensation
: When a stable droplet is formed through nucleation, it may grow further based on random collisions between vapor molecules and the particle, so called condensation. Since the probability for potential collisions is dependent on the mean free path of the

carrier gas (see Section 2.3), growth by condensation differs between using air and helium.

Evaporation
Evaporation is the opposite to condensation, which appears when more molecules escape the particle surface than condensate.

Coagulation
Aerosol particles may collide with one another and therefore form bigger particles. Coagulation is called thermal, when the collisions are based on Brownian motion, whereas kinematic coagulation is driven through collisions caused by external forces, like gravity or electricity.

Agglomeration
The term coagulation was initially developed for particles in liquids. For solid particles, this process is commonly called agglomeration.

Nanoparticle generators are an indispensable tool for basic research experiments. Throughout this work, the following three generators were in use:

- Grimm WO_x Generator Model #7.860
- Hot Wire Generator
- Carbolite® Gero Tube Furnace Type 301

In this study, two DMAs with different dimensions were in use. From now on, they are referred to as

- **DMA 1**: R_{in} = 17.5 mm for the inner radius, R_{out} = 24.1 mm for the outer radius and length L = 15 mm.
- **DMA 2**: R_{in} = 17.5 mm for the inner radius, R_{out} = 24.1 mm for the outer radius and length L = 150 mm.

6.1 Grimm WO_x Generator

In this section, a characterization of the Grimm WO_x Generator Model #7.860 is given.

This nanoparticle generator is based on the design of a prototype, built at the Institute of Chemical Kinetics and Combustion in Novosibirsk (Ankilov et al. [2002]). Additional improvements at the University of Vienna (Reischl et al. [1997]) resulted in a cooperation with Grimm-Aerosoltechnik GmbH & Co. Kg which made the generator commercially available as Tungsten Oxide generator Model #7.860.

The working principle relies on sublimation of tungsten oxide from a heated coil. In oxygen or air, the formed oxide is always WO_3 ([Erik Lassner, 2012, p.86]). At temperatures above 750°C tungsten trioxide sublimates. According to Steiner [2011], the heating cell of the Grimm WO_x generator provides temperatures of up to 900°C.

Figure 6.1 depicts the Grimm WO_x generator, as well as its flow schematic. It displays three valves that allow adjustment of different volumetric flow rates that are controlled with float-type flow meters. The *WO_x Air* rotameter is labeled from 1.6 liters per hour (l/h) to 16 l/h, but the flow can increased further. The highest possible *WO_x Air* flow setting is referred to as *maximal WO_x Air*. This flow can be diluted with *Carrier Air* in the range between 50 l/h and 500 l/h. Both streams flow in the heating unit with the tungsten coil, transporting the molecules. If lower particle concentrations are needed, further dilution can be provided via *Dilution Air* between 180 l/h and 1800 l/h. Beyond that, the voltage of the heater can be changed. By means of all these settings, different sizes and concentrations of nanoparticles can be achieved.

(a) Grimm WO_x Generator Model 7.860

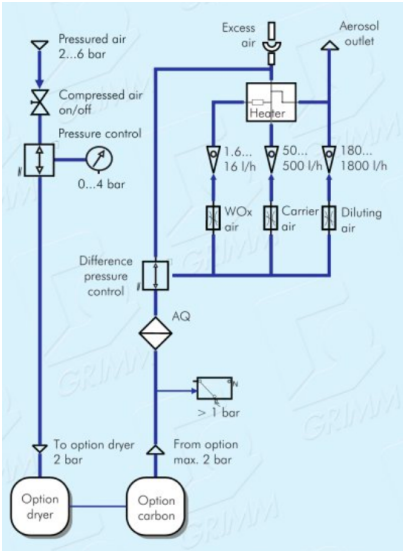

(b) Flow schematic of the WO_x Generator

Figure 6.1: The left panel depicts the Grimm WO_x Generator Model 7.860 with its three different valves that permit changes in the volumetric flow rates. The right panel represents its flow schematic. *WO_x Air* and *Carrier Air* transport the molecules out of the heater. For low concentrations, additional dilution can be provided via *Dilution Air*. Pictures: Grimm-aerosol

6.1.1 Experimental Setup

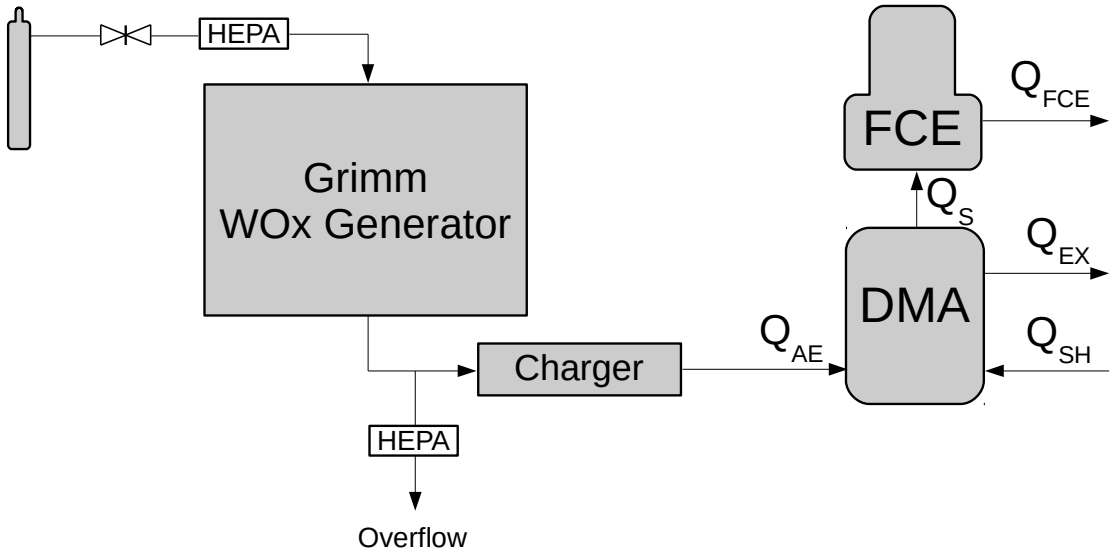

Figure 6.2: Schematic figure of the WO_x Generator Setup

Figure 6.2 depicts a schematic representation of the experimental Differential Mobility Particle Sizer (DMPS) setup, as described in Section 5. The DPMS was operated with DMA 1 (see Chapter 6).

Air from a gas cylinder with pressure of 2 bar was provided through a valve and an additional High Efficiency Particulate Air (HEPA) filter into the inlet of the WO_x generator. It was not possible to operate this nanoparticle generator with helium as carriere gas. It is likely, that the lack of oxidation impedes sublimation of molecules from the tungsten curl.

As discussed in Section 5, a DMPS in combination with subsequent back-calculation permits retrieval of the number size distribution of the generated nanoparticles.

6.1.2 Experimental Results

In this section the experimental results of measuring the number size distributions of the WO_x nanoparticle generator are presented. The adjusted flow rates in units liter per minute [l/min] of the DMPS are listed below and were held constant throughout all measurements with the WO_x generator.

$$Q_{sh} = Q_{ex} = 31\ l/min \qquad Q_{ae} = Q_s = 2\ l/min$$

Initially, the WO_x Air was set to maximal flow. Regarding Carrier Air six different settings, between 50 l/h and 500 l/h were chosen. In Table 6.1, parameters of the respective lognormal fits and calculated means are listed (see Section 3.2). For all measurements no additional Dilution Air was added. The heater voltage was set to a maximum of 15.78 V and 1.62 A.

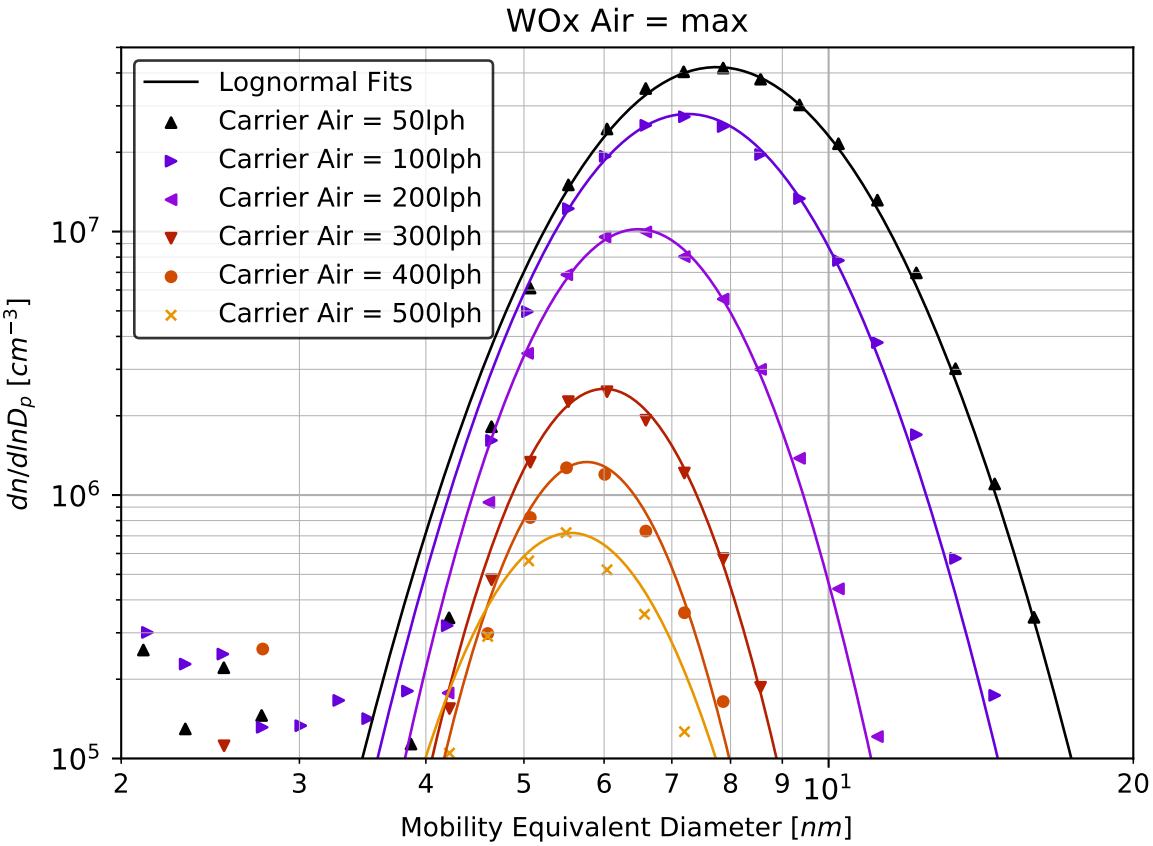

Figure 6.3: Number size distributions with maximal WO_x Air flow for different Carrier Air dilution and corresponding best lognormal fits.

Carrier Air [l/h]	μ	σ_{GSD}	Mode [nm]	Median [nm]	Mean [nm]
50	2.10	1.26	7.75	8.18	8.40
100	2.02	1.23	7.26	7.58	7.75
200	1.89	1.19	6.49	6.68	6.78
300	1.81	1.16	6.00	6.14	6.22
400	1.77	1.15	5.76	5.88	5.95
500	1.74	1.17	5.56	5.71	5.79

Table 6.1: Lognormal fit parameters and respective means for different Carrier Air settings and maximal WO_x Air.

Roughly speaking, nanoparticles between 4 nm and 18 nm were measured, with mean diameters ranging between 8.4 nm and 5.8 nm. Needless to say, that with increasing dilution through higher Carrier Air, the concentration decreases. Less obvious is, that with rising

dilution the particles undergo faster cooling and therefore become overall smaller. In addition, higher dilution rates lead to less coagulation, keeping the particles more to their original size. Thereafter, the WO_x Air was successive lowered to 16 l/h, 10 l/h, 6 l/h and 3 l/h.

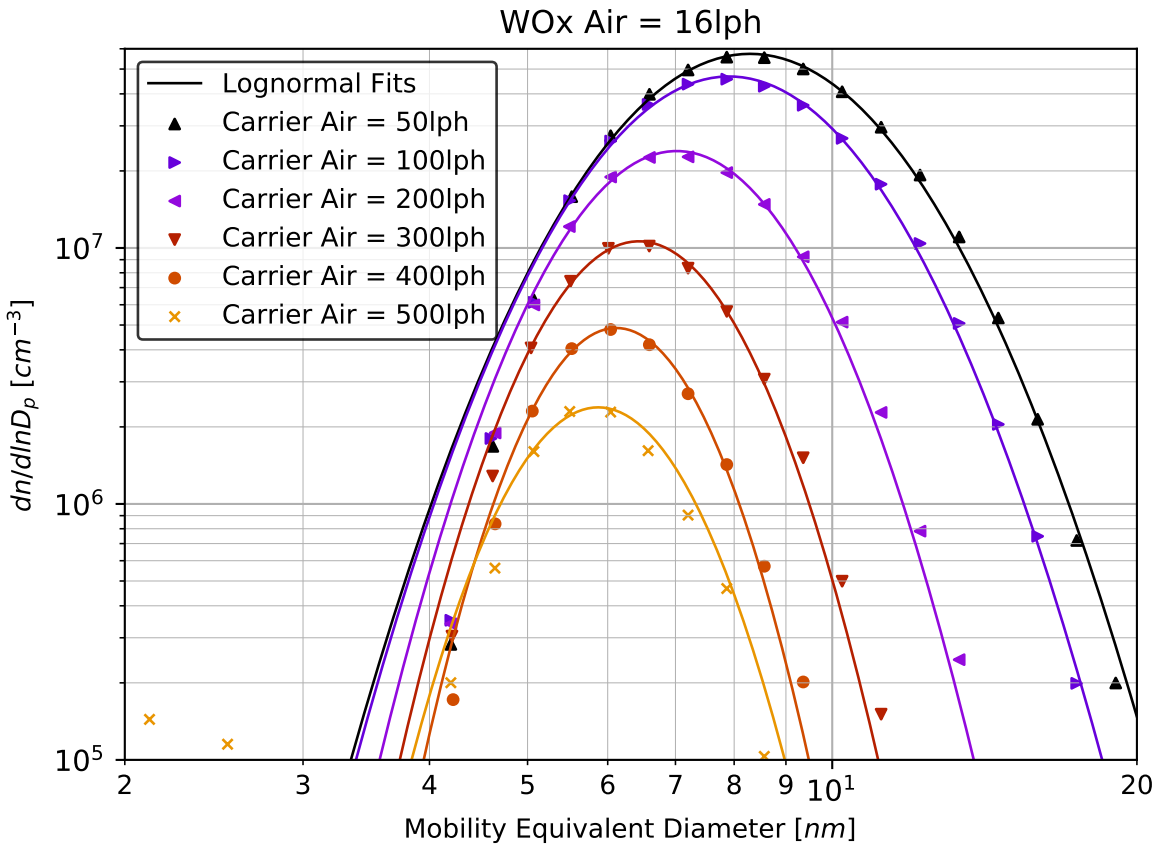

Figure 6.4: Number size distributions with WO_x Air flow of 16 l/h for different carrier air dilution.

Carrier Air [l/h]	μ	σ_{GSD}	Mode [nm]	Median [nm]	Mean [nm]
50	2.18	1.28	8.29	8.85	9.14
100	2.13	1.27	7.91	8.38	8.64
200	1.99	1.23	7.02	7.32	7.47
300	1.89	1.19	6.44	6.65	6.76
400	1.84	1.17	6.12	6.27	6.34
500	1.80	1.17	5.87	6.04	6.13

Table 6.2: Lognormal fit parameters and respective means for different Carrier Air settings and WO_x Air flow of 16 l/h.

It is noteworthy, that a decrease of the WO_x Air to 16 l/h results in higher concentrations, as well as overall slightly bigger nanoparticles. It is anticipated, that with these settings the highest particle concentrations were achieved.

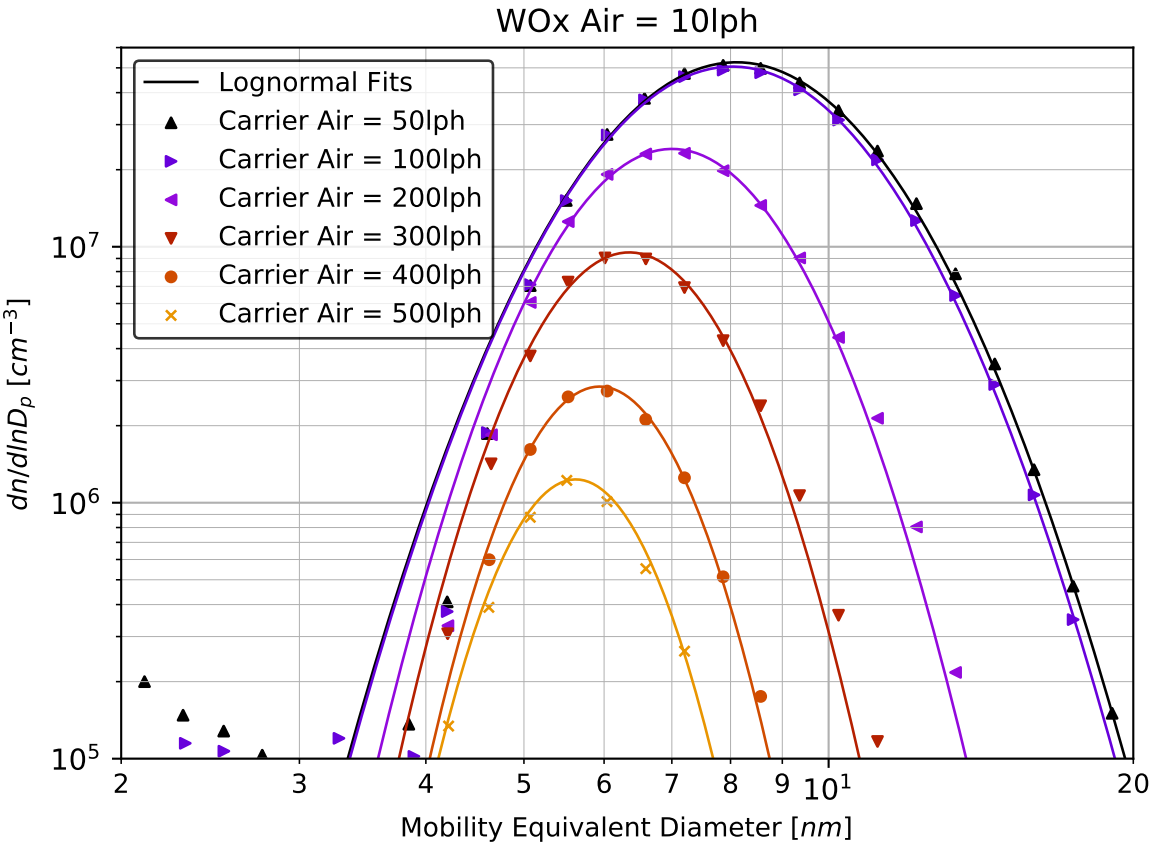

Figure 6.5: Number size distributions with WO_x Air flow of 10 l/h for different carrier air dilution.

Carrier Air [l/h]	μ	σ_{GSD}	Mode [nm]	Median [nm]	Mean [nm]
50	2.15	1.28	8.11	8.63	8.90
100	2.14	1.28	8.03	8.53	8.80
200	1.99	1.22	7.00	7.29	7.44
300	1.88	1.19	6.35	6.54	6.65
400	1.80	1.16	5.94	6.07	6.14
500	1.74	1.15	5.62	5.73	5.79

Table 6.3: Lognormal fit parameters and respective means for different Carrier Air settings and WO_x Air flow of 10 l/h.

Lowering the WO_x Air to 10 l/h, the concentrations appear to decrease, but are still higher than in the case of maximal WO_x Air flow rate.

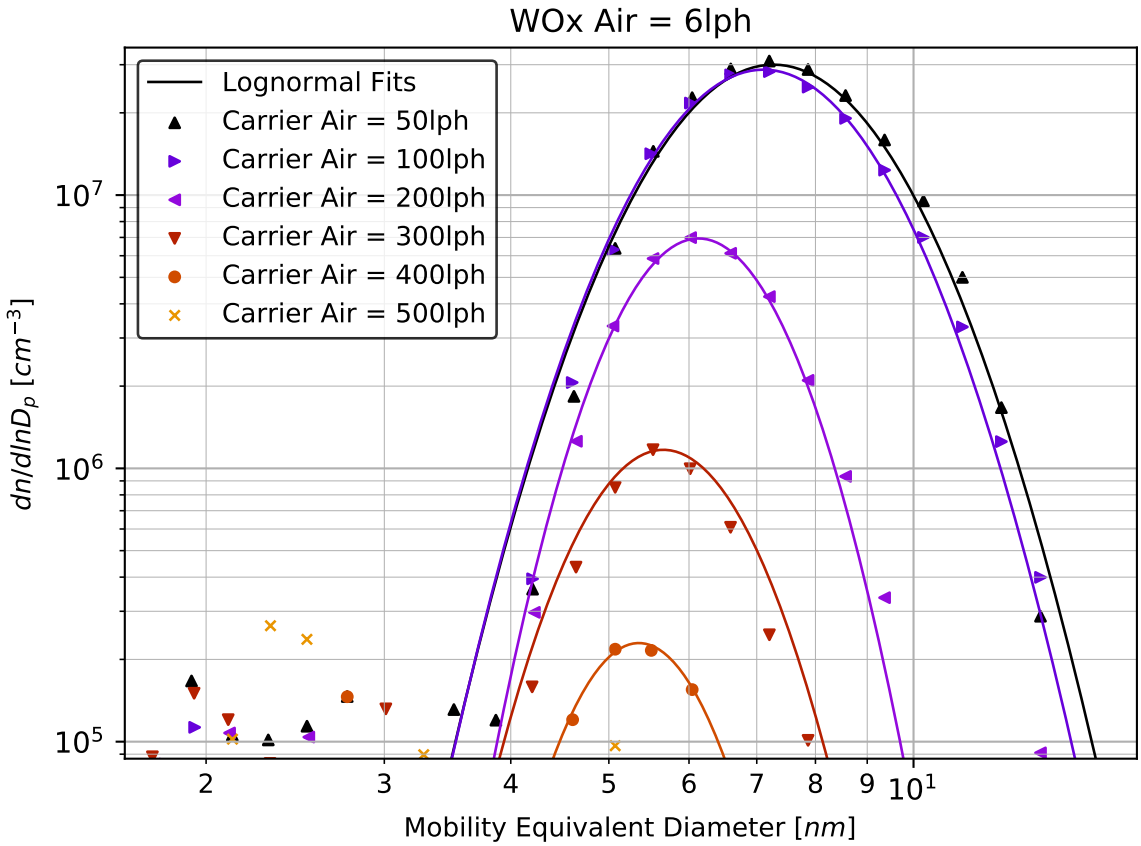

Figure 6.6: Number size distributions with WO_x Air flow of 6 l/h for different Carrier Air dilution.

Carrier Air [l/h]	μ	σ_{GSD}	Mode [nm]	Median [nm]	Mean [nm]
50	2.03	1.23	7.27	7.62	7.79
100	2.00	1.22	7.11	7.42	7.58
200	1.84	1.17	6.13	6.28	6.36
300	1.76	1.17	5.65	5.81	5.89
400	1.69	1.15	5.35	5.45	5.51

Table 6.4: Lognormal fit parameters and respective means for different Carrier Air settings and WO_x Air flow of 6 l/h.

Adjusting the WO_x Air to 6 l/h, the number size distributions become narrower. The concentrations, together with the overall particle sizes drop significantly. For the highest dilution of 500 l/h, no distribution was measurable.

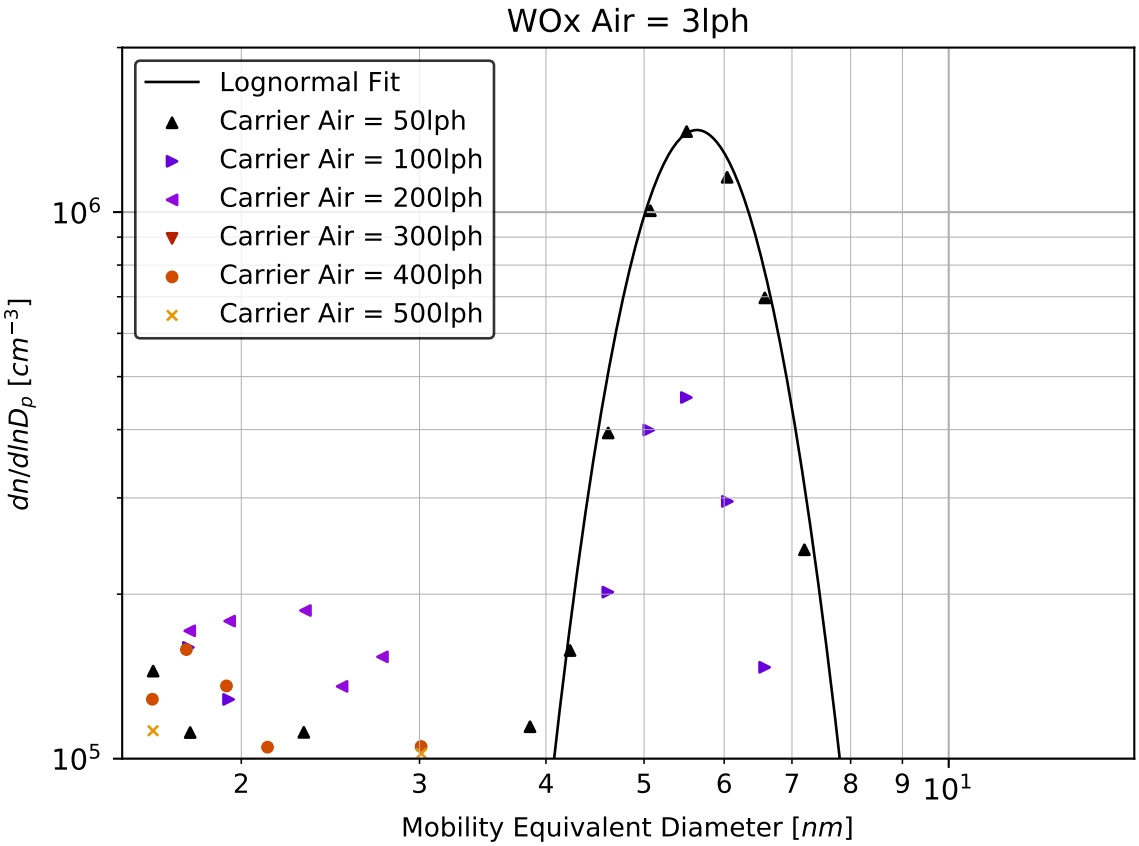

Figure 6.7: Number size distributions with WO_x Air flow of 3 l/h for different Carrier Air dilution.

Carrier Air [l/h]	μ	σ_{GSD}	Mode [nm]	Median [nm]	Mean [nm]
50	1.74	1.15	5.64	5.75	5.81

Table 6.5: Lognormal fitting parameters and respective means for Carrier Air 50 l/h and WOx air flow of 3 l/h.

At the lowest measured flow rate of WO_x air, only the distribution for the bottom limit of dilution via carrier air is worth the mention.

Altogether, the Grimm WO_x generator is a very stable source of aerosol nanoparticles in air. Its manual states generation of nanoparticles in the size range between 1.2 nm and 20 nm. 1.25 nm is the mobility equivalent diameter of WO_3 monomers (Kilpatrick [1971], Steiner [2011]). The used DMPS allowed to detect particles between 4 nm and 20 nm with eminently high concentrations.

Operating the generator with flow rates of 16 l/h for WO_x Air, low Carrier Air dilution (50 l/h) and maximal heater voltage, the highest concentrations were reached.

6.2 Hot Wire Generator

In this section, a glowing wire generator, hereafter referred to as hot wire generator, is described. Its basic functioning is nanoparticle generation via evaporating material from a resistively heated metal wire (Biskos et al. [2008]). The wrapped wire is connected to a DC power supply, with which the applied voltage and current can be altered.

This approach of nanoparticle synthesis was introduced by Schmidt-Ott et al. [1980]. Ever since this method is very common for production of metallic particles in aerosol research, for example Burtscher et al. [1982], de la Mora et al. [2003] and many others.

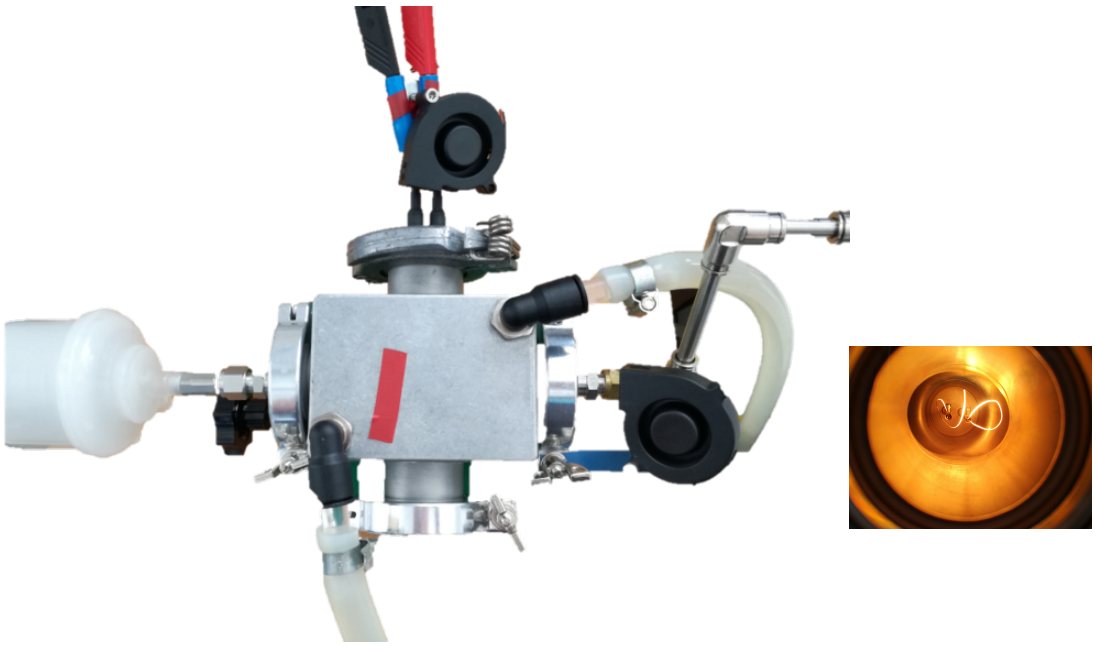

(a) **(b)**

Figure 6.8: **(a)** Top view of the Hot Wire nanoparticle generator. The carrier gas is coming through the HEPA filter from the left into the generator. In the middle of the water cooled housing, a metallic coil is installed. This wire is resistively heated by a DC power supply, its red and black connectors can be seen on the top. The evaporating material is picked up by the gas flow, leaving the generator on the right. Inflow and outflow of the coolant is provided via the transparent tubing. To enhance cooling of the fittings, additional fans are installed. A window in the front allows to monitor the wire. **(b)** A glowing wire as seen through this window.

Figure 6.8 depicts the hot wire generator as used in this work. A conducting wire is installed in a water cooled housing and is resistively heated with high current. This consequently leads to evaporation of the material. Combined with the carrier gas, high supersaturation can be achieved (Peineke et al. [2006]). By subsequent condensation, nanoparticles are formed, whereby most constant particle concentrations are achieved when the wire is heated close to its melting point. In general, the hot wire generator satisfies the condition of very high purity of the synthesized particles, since only the particle-generating wire is heated. This avoids pollution of the aerosol induced by hot surroundings (Biskos et al. [2008]).

6.2.1 Experimental Setup

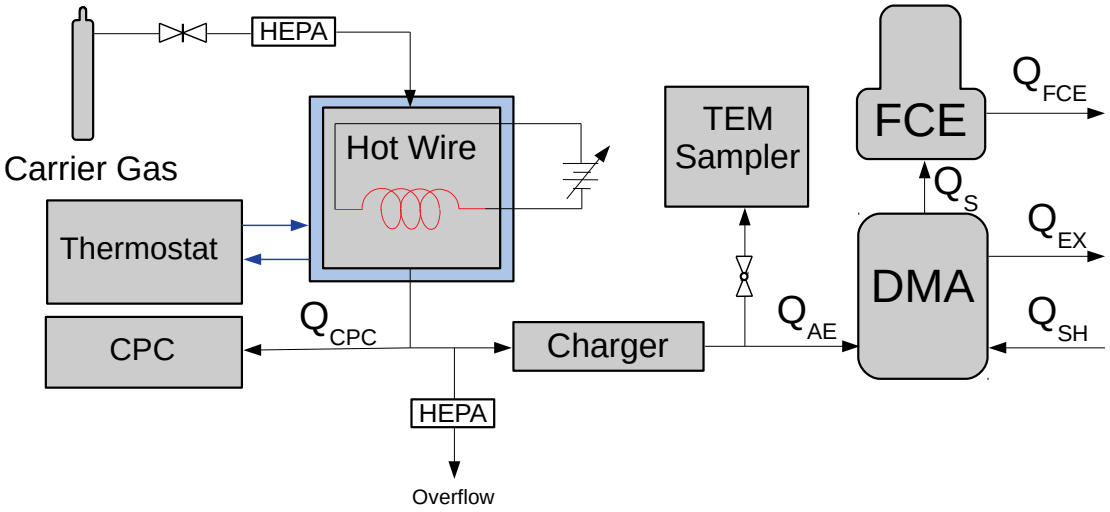

Figure 6.9: Hot Wire DMPS flow chart. The carrier gas of choice enters with a pressure of 2 bar and a volumetric flow rate of 6 lpm the hot wire generator, whose metal housing is water cooled with an associated thermostat. Downstream, a TSI CPC 3776 measures the total number concentration, the DMPS allows to obtain corresponding particle size distributions (see Chapter 5). TEM samples were accessed with a TSI Nanometer Aerosol Sampler Model 3089.

Nanoparticles were generated in air and helium. The pressure reducer of the gas cylinder was adjusted to 2 bar, a needle valve enabled various flow rates of carrier gas. The particle generating wire was connected to a DC power supply (BK Precision® Model 1901B), that allowed voltage settings within 1 V and 32 V and high currents up to 30 A. Sufficient water cooling of the metal housing was provided with a Lauda RCS 20-D thermostat adjusted to 20 °C. To avoid rupture of the wire, the voltage, as well as the current was increased stepwise. Downstream the particle generator, a TSI CPC 3776 was installed to measure total number concentrations, and the DMPS was set up (see Section 5.1) which provided data, with which the discrete size-dependent number distributions were calculated (see Section 5.3). In addition, TEM samples were taken, utilizing the TSI Nanometer Aerosol Sampler Model 3089.

For this work, following wire materials (with corresponding diameters) have been used:

- Silver (0.2 mm and 0.3 mm)
- Copper (0.4 mm)
- Brass (0.4 mm)
- Platin (0.4 mm)
- Stainless Steel (0.5 mm)
- Gold (0.3 mm)
- Tungsten (0.3 mm)

6.2.2 Experimental Results

In this section, the calculated number size distributions of nanoparticles synthesized by different wires with the hot wire generator are presented.

Silver 0.2 mm

Most stable silver nanoparticle concentrations were achieved with 8.2 A and 2.4 V (0.2 mm wire) and 12.5 A and 2 V (0.3 mm wire). Figures 6.10 and 6.11 depict the number size distributions for these power supply settings and wires with diameters of 0.2 mm and 0.3 mm respectively. It was these currents and voltages, where the wires started glowing and an increase of only 0.2 A resulted in instantaneous rupture. Because of the imperfect stability of the generated particle size distributions, four (0.2 mm wire), alternatively three (0.3 mm wire) DMPS scans were arithmetically averaged and lognormal fitted (Figures 6.10 and 6.11). The corresponding fitting parameters are given in Tables 6.7 and 6.8 as well as the calculated means and the averaged total concentration obtained from the CPC. Flow rates of these measurements are provided in Table 6.6.

For measurements with both silver wires the DMA 1 (see Chapter 6) was operated.

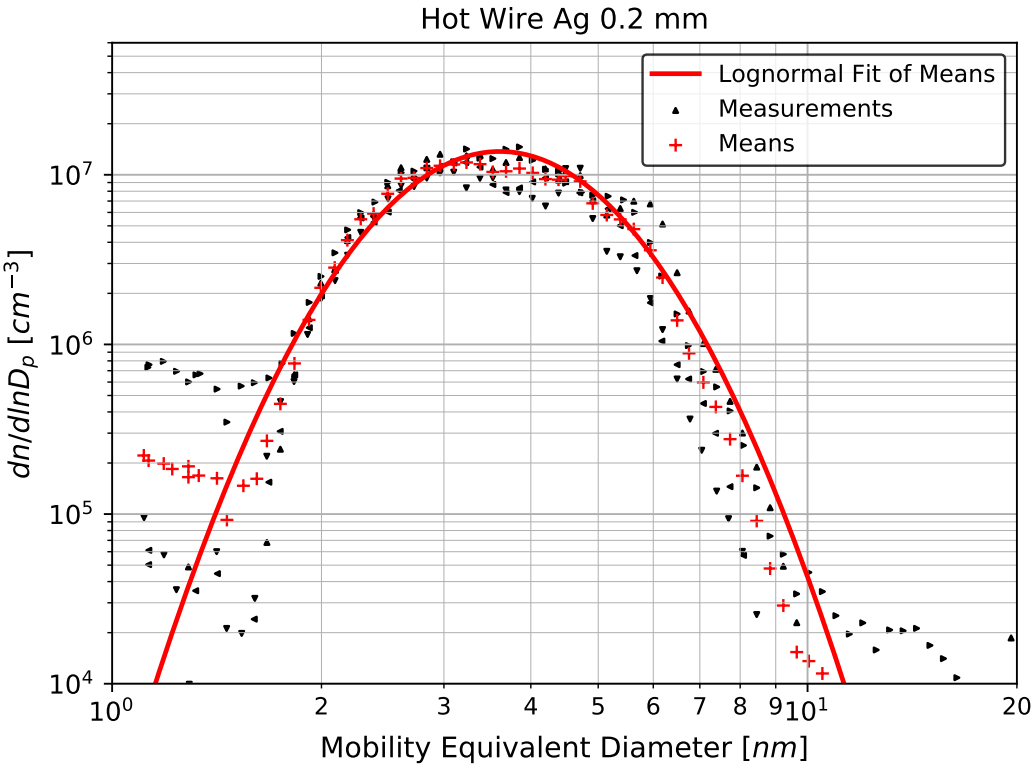

Figure 6.10: Silver particle size distributions generated with the hot wire generator and silver wire with a diameter of 0.2 mm (black) and the arithmetic mean value of four DMPS measurements performed at identical settings with corresponding least square lognormal fit of the means (red).

Flow Conditions Hot Wire Ag 0.2 mm and 0.3 mm in Air			
$Q_{HotWire}$ [l/min]	$Q_{sh} = Q_{ex}$ [l/min]	$Q_s = Q_{ae}$ [l/min]	Q_{CPC} [l/min]
6	19	2.2	1.5

Table 6.6: DMPS flow conditions Hot Wire Ag in Air.

Power Supply Settings		μ	σ_{GSD}	Mode [nm]	Median [nm]	Mean [nm]	N_{tot} $[cm^{-3}]$
I = 8.2 A	U = 2.4 V	1.35	1.39	3.47	3.85	4.06	$4.7 \cdot 10^5$

Table 6.7: Lognormal fitting parameters and corresponding means for silver nanoparticles generated with the hot wire generator and a wire with diameter of 0.2 mm and total number concentration measured with the CPC.

Silver 0.3 mm

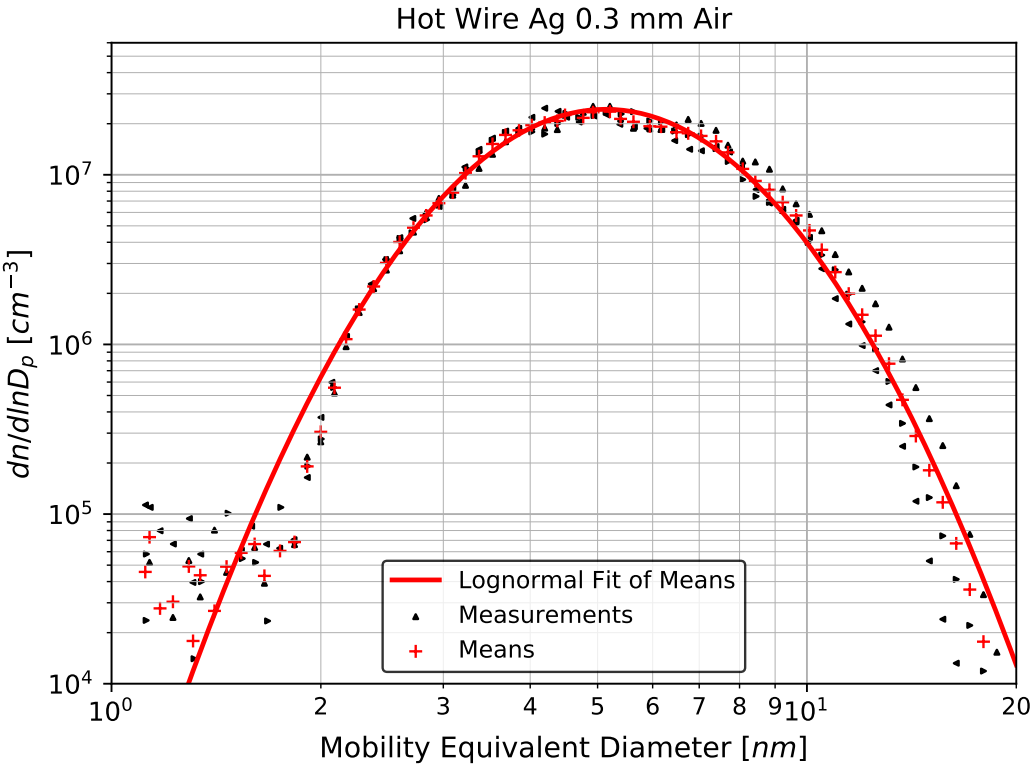

Figure 6.11: Silver particle size distributions generated with the hot wire generator and silver wire with a diameter of 0.3 mm (black) and the arithmetic mean value of three DMPS measurements performed at identical settings with corresponding least square lognormal fit of the means (red).

Power Supply Settings		μ	σ_{GSD}	Mode [nm]	Median [nm]	Mean [nm]	N_{tot} [cm^{-3}]
I = 12.5 A	U = 2 V	1.76	1.43	5.11	5.86	6.28	$4.9 \cdot 10^5$

Table 6.8: Lognormal fitting parameters and corresponding means for silver nanoparticles generated with the hot wire generator and a curl with diameter of 0.3 mm and total number concentration measured with the CPC.

Stainless Steel 0.5 mm

Stainless steel nanoparticles were generated using a wire with 0.5 mm in diameter. Figure 6.12 illustrates different number size distributions for particles generated with certain power supply settings with carrier gas air, Figure 6.13 for helium respectively. Increasing the current stepwise, for helium and air, initial glowing was observed between 5 A and 6 A. Thenceforward, the concentrations began to stabilize. In air, distribution modes between 4.4 nm and 8.1 nm were measured, whereas in helium the modes do not exceed 4.9 nm, even with high currents.

The DMPS flow conditions for these measurements are given in Tables 6.9 and 6.11, lognormal fitting parameters with corresponding means and CPC readings are listed in Table 6.10 for air, as well as 6.12 for particles generated in helium. For both carrier gases, DMA 1 (see Chapter 6) was operated.

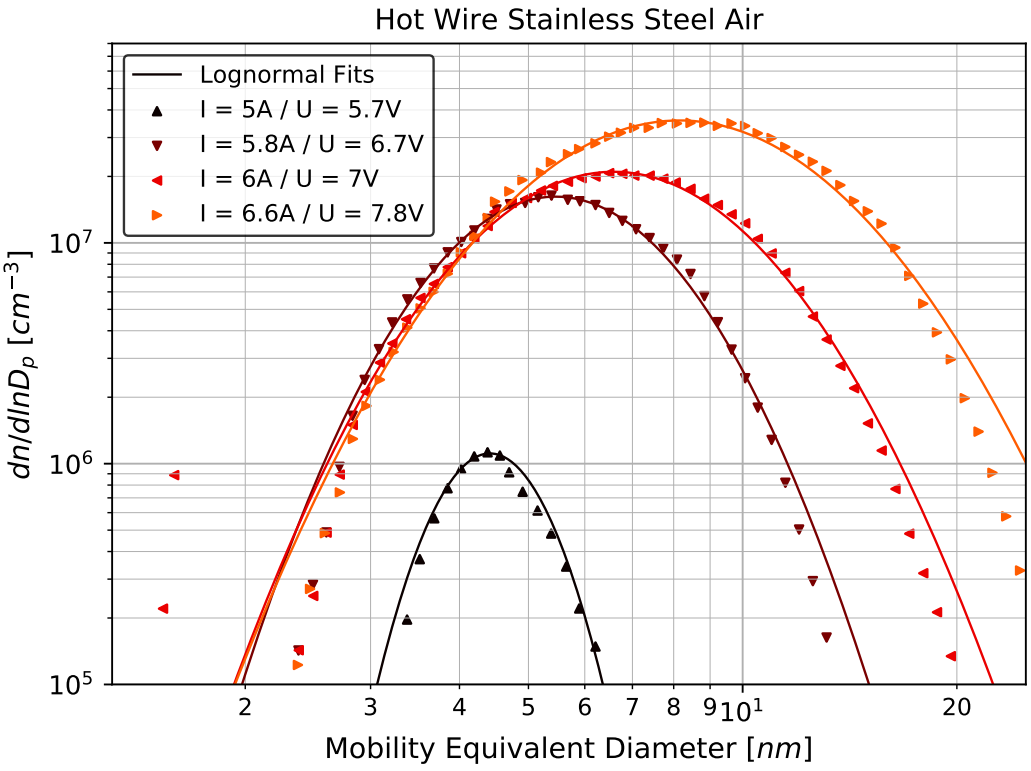

Figure 6.12: Stainless steel particle size distributions generated in air with the hot wire generator for different power supply settings with corresponding lognormal fits.

Flow Conditions Hot Wire Stainless Steel in Air			
$Q_{HotWire}$ [l/min]	$Q_{sh} = Q_{ex}$ [l/min]	$Q_s = Q_{ae}$ [l/min]	Q_{CPC} [l/min]
6	19	2.2	1.5

Table 6.9: DMPS flow conditions Hot Wire stainless steel. Wire diameter = 0.5 mm

Power Supply Settings		μ	σ_{GSD}	Mode [nm]	Median [nm]	Mean [nm]	N_{tot} [cm^{-3}]
I = 5 A	U = 5.7 V	1.31	1.19	4.42	4.54	4.60	$3.0 \cdot 10^5$
I = 5.8 A	U = 6.7 V	1.80	1.38	5.46	6.04	6.35	$4.6 \cdot 10^5$
I = 6 A	U = 7 V	2.03	1.43	6.59	7.58	8.14	$4.7 \cdot 10^5$
I = 6.6 A	U = 7.8 V	2.27	1.52	8.15	9.72	10.61	$5.4 \cdot 10^5$

Table 6.10: Lognormal fitting parameters and corresponding means for stainless steel nanoparticles generated with the hot wire generator and a wire with diameter of 0.5 mm and total number concentration measured with the CPC.

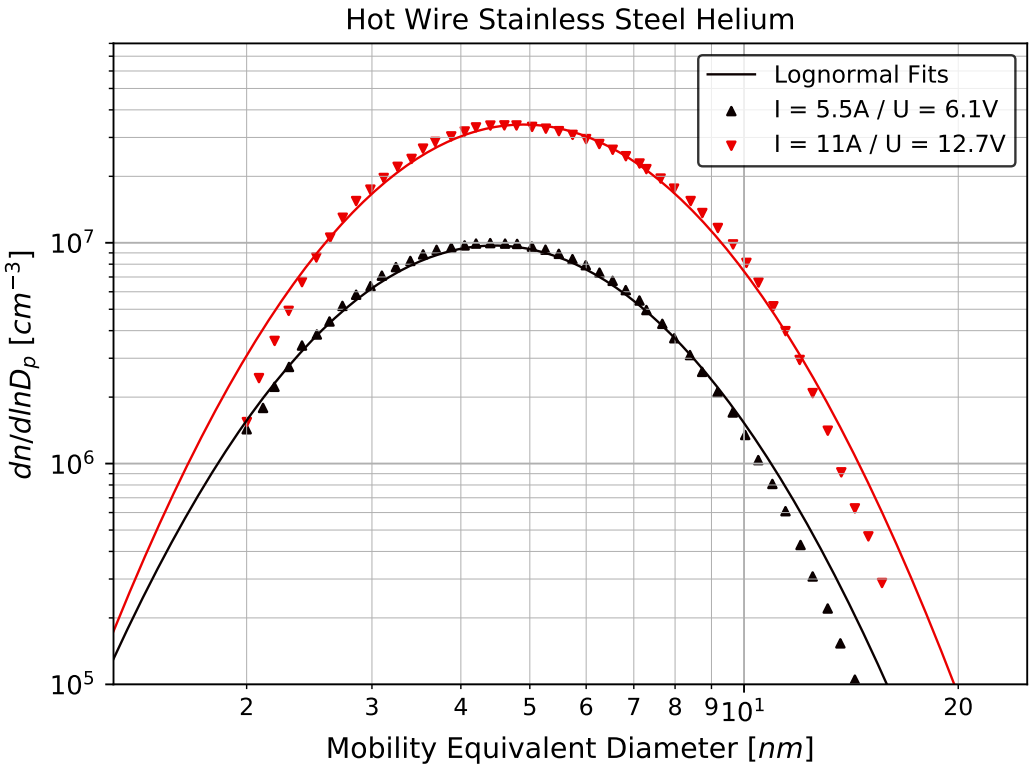

Figure 6.13: Stainless steel particle size distributions generated in helium with the hot wire generator for different power supply settings with corresponding lognormal fits.

Flow Conditions Hot Wire Stainless Steel in Helium			
$Q_{HotWire}$ [l/min]	$Q_{sh} = Q_{ex}$ [l/min]	$Q_s = Q_{ae}$ [l/min]	Q_{CPC} [l/min]
6	34	1.9	1.5

Table 6.11: DMPS flow conditions Hot Wire stainless steel in helium. Wire diameter = 0.5 mm

Power Supply Settings		μ	σ_{GSD}	Mode [nm]	Median [nm]	Mean [nm]	N_{tot} [cm^{-3}]
I = 5.5 A	U = 6.1 V	1.67	1.52	4.46	5.32	5.81	$3.5 \cdot 10^5$
I = 11 A	U = 12.7 V	1.76	1.50	4.88	5.78	6.30	$>1 \cdot 10^6$

Table 6.12: Lognormal fitting parameters and corresponding means for stainless steel nanoparticles generated in helium with the hot wire generator and a wire with diameter of 0.5 mm and total number concentration measured with the CPC. The total number concentration for I = 11 A, exceeded the upper limit of the TSI CPC 3776.

Tungsten 0.3 mm

Contrary to the Grimm WO_x Generator (characterized in Section 6.1), the hot wire generator allows to synthesize tungsten nanoparticles, to be more precise, tungsten blue oxide (Bauer [2019]) in helium. Experiments with tungsten wires resulted in a conspicuous blue coating inside the hot wire generator which had to be cleaned after every measurement.

In general, the most stable concentrations were achieved with tungsten wires. It has the highest melting point among all metals (3422°C ([David R. Lide, 2005, p.4-33])). This is why, very high currents could be applied without spontaneous rupture. Depending on the power supply settings, stable nanoparticle concentrations for up to eight hours were accomplished. Figure 6.14 depicts different particle size distributions for various settings. First glowing was observed at roughly 9 A. The higher the applied current, the more and bigger particles were measured.

The shape of the size distributions deviating from lognormal behavior indicates that the primary particles agglomerate considerably to bigger structures. This circumstance is plainly visible at the TEM images (Figure 6.15). Both panels show the same sample with different mangifications and were sampled at the same hot wire current of 12 A for 15 minutes with the TSI Nanometer Aerosol Sampler Model 3089 (see Section 5.1).

The DMPS flow rates of these measurements are provided in Table 6.13, total number concentrations are listed in Table 6.14. For tungsten wires, DMA 2 (see Chapter 6) was used. As discussed in Section 5.2, to avoid electrical breakdown the maximal scanning voltage was set to 1050 V, which allows detection of particles up to 75 nm (see Equation 2.19).

Flow Conditions Hot Wire Tungsten in Helium			
$Q_{HotWire}$ [l/min]	$Q_{sh} = Q_{ex}$ [l/min]	$Q_s = Q_{ae}$ [l/min]	Q_{CPC} [l/min]
6	20	1.9	1.5

Table 6.13: DMPS flow conditions Hot Wire tungsten in helium. Wire diameter = 0.3 mm

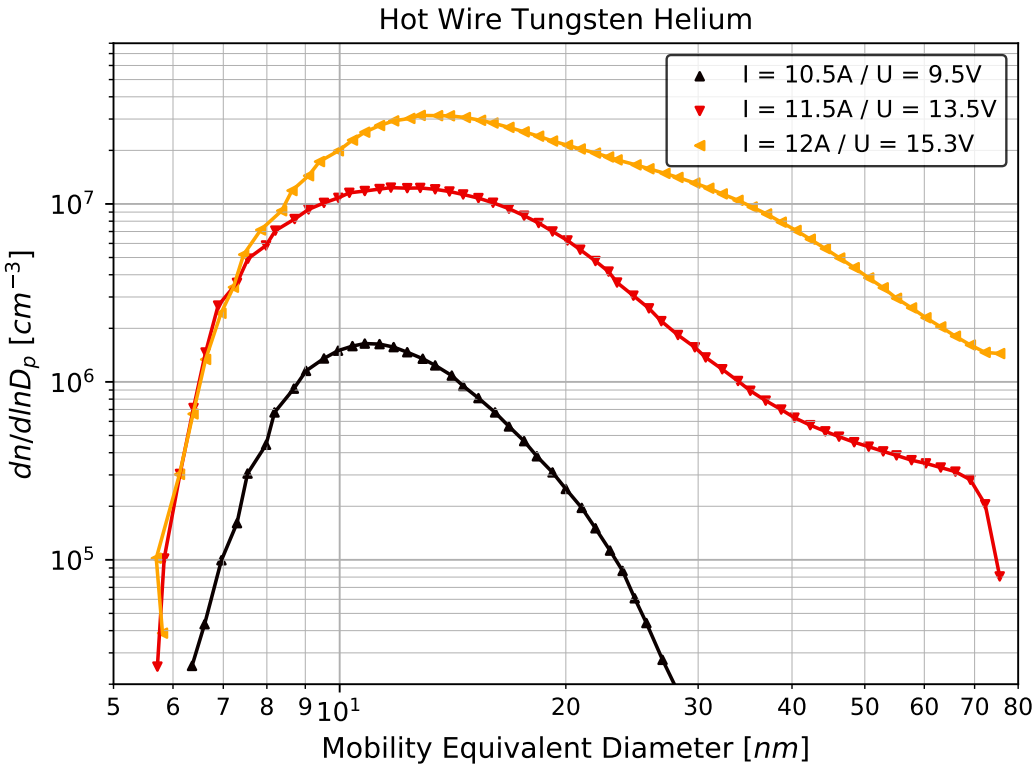

Figure 6.14: Tungsten blue oxide nanoparticle size distributions for different power supply settings beginning with 10.5 A, where initial glowing was observed. The higher the applied current and voltage, the higher the concentrations. Because of the high melting point of tungsten, it can handle very high power supply settings. As a result, stable particle output over several hours can be achieved.

Power Supply Settings		N_{tot} [cm^{-3}]
I = 10.5 A	U = 9.5 V	$3.8 \cdot 10^5$
I = 11.5 A	U = 13.5 V	$4.3 \cdot 10^5$
I = 12 A	U = 15.3 V	$7 \cdot 10^5$

Table 6.14: Total number concentration readings for several power supply settings of tungsten blue oxide generated with the hot wire generator

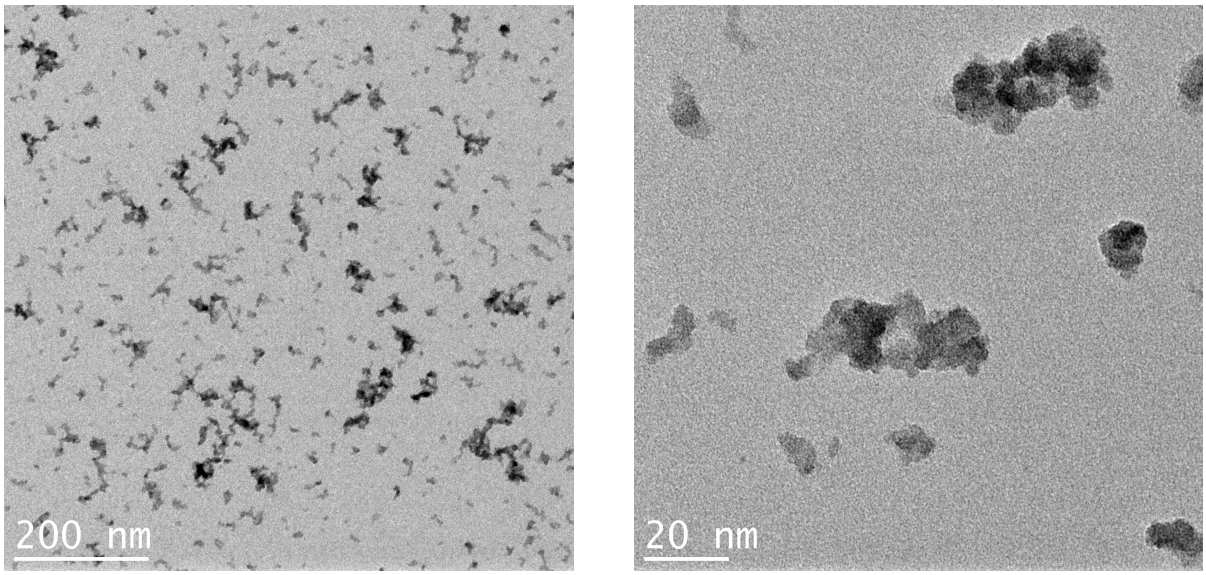

Figure 6.15: TEM images of tungsten blue oxide nanoparticles, synthesized with the hot wire generator. On the right panel, smaller structures, consisting of only few primary particles are visible. The left panel depicts the same sample at lower magnification and clearly illustrates the sizable agglomerates. Pictures taken from Bauer [2019]

In contrast to previously discussed wires, silver, stainless steel and tungsten, it was not possible to achieve constant particle generation with the following materials (copper, platinum, gold and brass). Nonetheless, distinctive particle size distributions were measured. Since the total number of particles decreased shortly after ramping up the wire-current, the following measurements show the first DMPS scan after an increase.

Copper 0.4mm

Figure 6.16 depicts two particle size distributions of copper nanoparticles generated in air for the most stable settings around 12 A. Higher currents resulted in higher concentrations and bigger particles for merely a few seconds before declining to lower numbers and sizes. First wire glowing was observed at 16 A and 2 V, which resulted in instantaneous rupture. DPMS flows are given in Table 6.15, lognormal means of the fitted distributions are listed in Table 6.16. The DMPS was operated with DMA 1 (see Chapter 6).

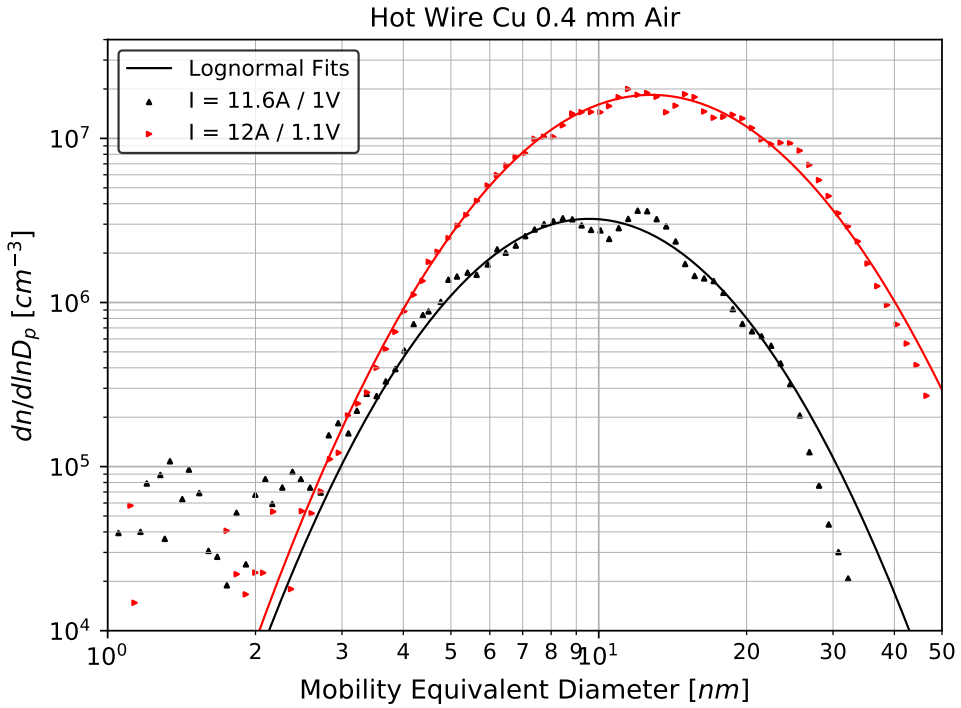

Figure 6.16: Copper particle size distributions generated in air with the hot wire generator for different power supply settings with corresponding lognormal fits.

Flow Conditions Hot Wire Copper in Air			
$Q_{HotWire}$ [l/min]	Q_{sh} = Q_{ex} [l/min]	Q_s = Q_{ae} [l/min]	Q_{CPC} [l/min]
6	19	2.2	1.5

Table 6.15: DMPS flow conditions Hot Wire copper in air. Wire diameter = 0.4 mm

Power Supply Settings		μ	σ_{GSD}	Mode [nm]	Median [nm]	Mean [nm]
I = 11.6 A	U = 1 V	2.45	1.55	9.56	11.62	12.81
I = 12 A	U = 1.1 V	2.77	1.60	12.78	16.01	17.91

Table 6.16: Lognormal fitting parameters and corresponding means of copper particle size distributions for different power supply settings. Because of a (at these currents) small but steady decline in concentration, no CPC readings are given.

Platinum 0.4 mm

A platinum wire with a diameter of 0.4 mm was used to generate nanoparticles with carrier gas air. Figure 6.17 illustrates two measured size distributions, corresponding means are listed in Table 6.18, the volumetric flow rates of the DMPS can be found in Table 6.17. The calculated modes are between 4.27 nm and 4.17 nm. An increase of the wire current did not result in overall bigger particles.

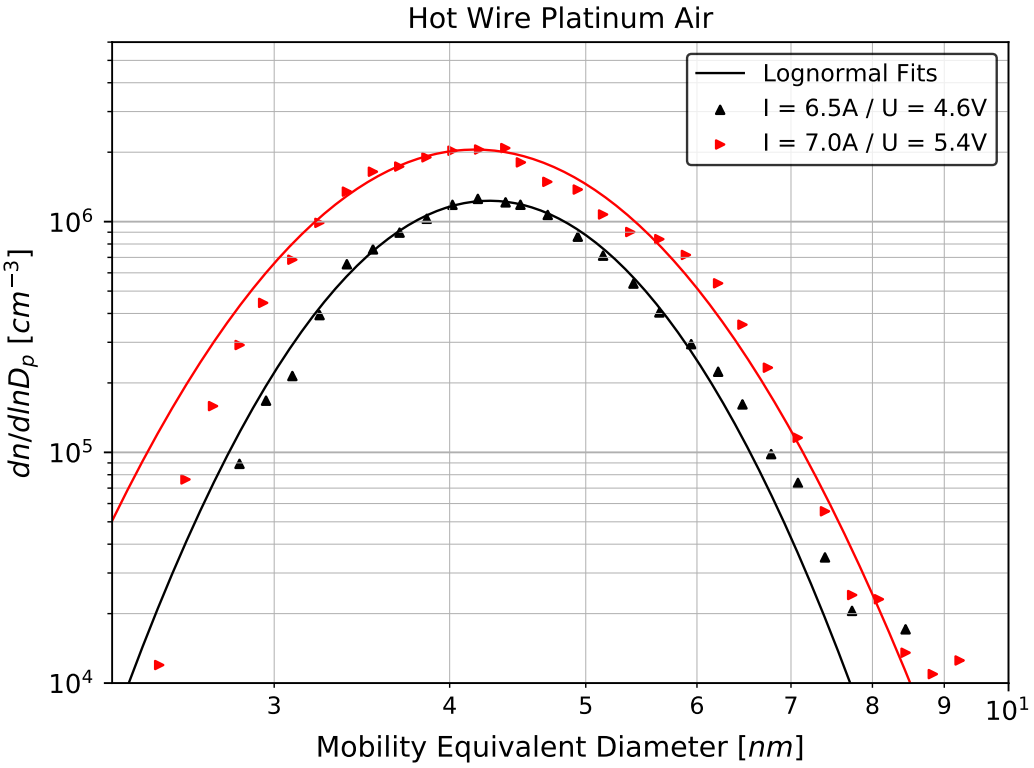

Figure 6.17: Platinum particle size distributions generated in air with the hot wire generator for different power supply settings with corresponding lognormal fits.

Flow Conditions Hot Wire Platinum in Air			
$Q_{HotWire}$ [l/min]	$Q_{sh} = Q_{ex}$ [l/min]	$Q_s = Q_{ae}$ [l/min]	Q_{CPC} [l/min]
6	19	2.2	1.5

Table 6.17: DMPS flow conditions Hot Wire platin in air. Wire diameter = 0.4 mm

Power Supply Settings		μ	σ_{GSD}	Mode [nm]	Median [nm]	Mean [nm]
I = 6.5 A	U = 4.6 V	1.49	1.21	4.27	4.43	4.51
I = 7 A	U = 5.4 V	1.46	1.25	4.17	4.37	4.48

Table 6.18: Lognormal fitting parameters and corresponding means of platinum particle size distributions for different power supply settings.

Gold 0.3 mm

Figure 6.18 depicts three different gold nanoparticle size distributions, that were obtained in helium. High currents were essential, first particles were measured at 11 A and 1.5 V, even at the 18 A that were applied on the gold wire, no glowing was observed. Greater power supply settings did not result in higher particle concentrations, on the contrary, most particles were obtained with lower settings. As mentioned before, after an initial spike in particle concentrations shortly after increasing the current on the wire, the total number did fall off within seconds. DMPS flow conditions are listed in Table 6.19. These measurements were performed with DMA 2 (see Chapter 6).

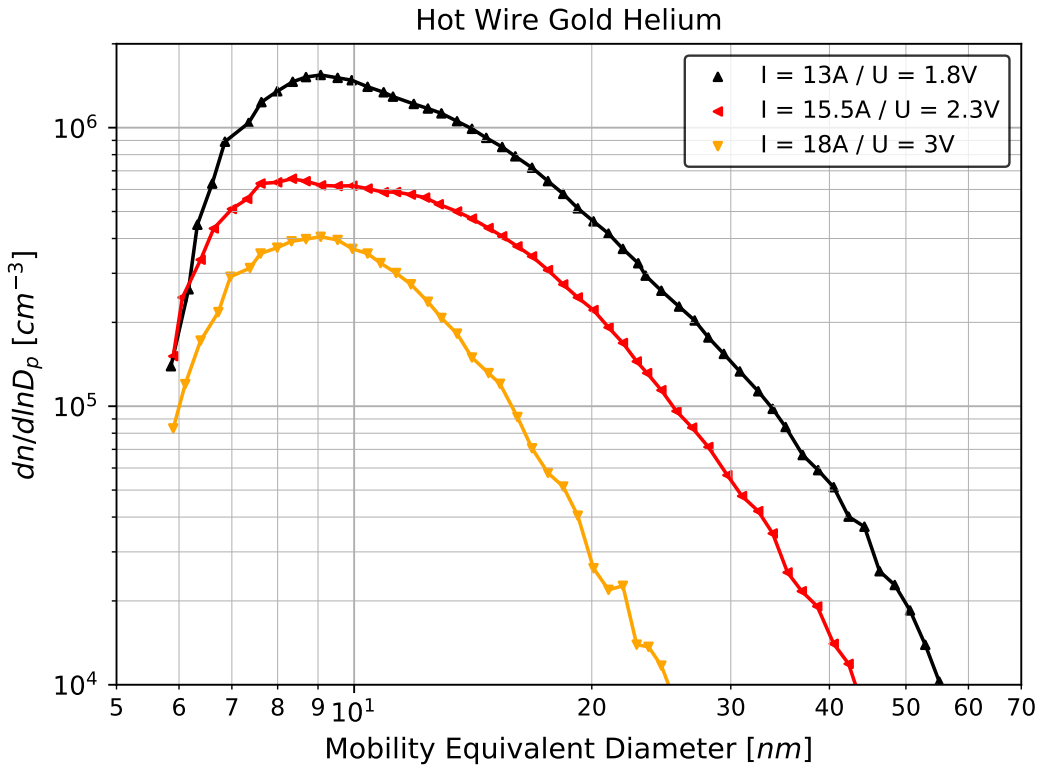

Figure 6.18: Particle size distributions of gold nanoparticles generated in helium. Particularly noteworthy is, that higher currents applied on the wire did not result in higher particle concentration.

Flow Conditions Hot Wire Gold in Helium			
$Q_{HotWire}$ [l/min]	$Q_{sh} = Q_{ex}$ [l/min]	$Q_s = Q_{ae}$ [l/min]	Q_{CPC} [l/min]
6	20	1.9	1.5

Table 6.19: DMPS flow conditions Hot Wire gold in helium. Wire diameter = 0.3 mm

Brass 0.4 mm

Brass nanoparticle size distributions generated in air, are shown in Figure 6.19. Best stability was obtained with high currents, slightly before wire rupture (13 A, 2.8 V). As for gold, a particularly conspicuous aspect is, that greater concentrations were achieved with lower current on the wire. Furthermore, the particles became smaller. Calculated distribution modes decreased from 6.08 nm down to 5.14 nm (see Figure 6.19 and Table 6.21). DMA 1 (see Chapter 6) was operated for brass.

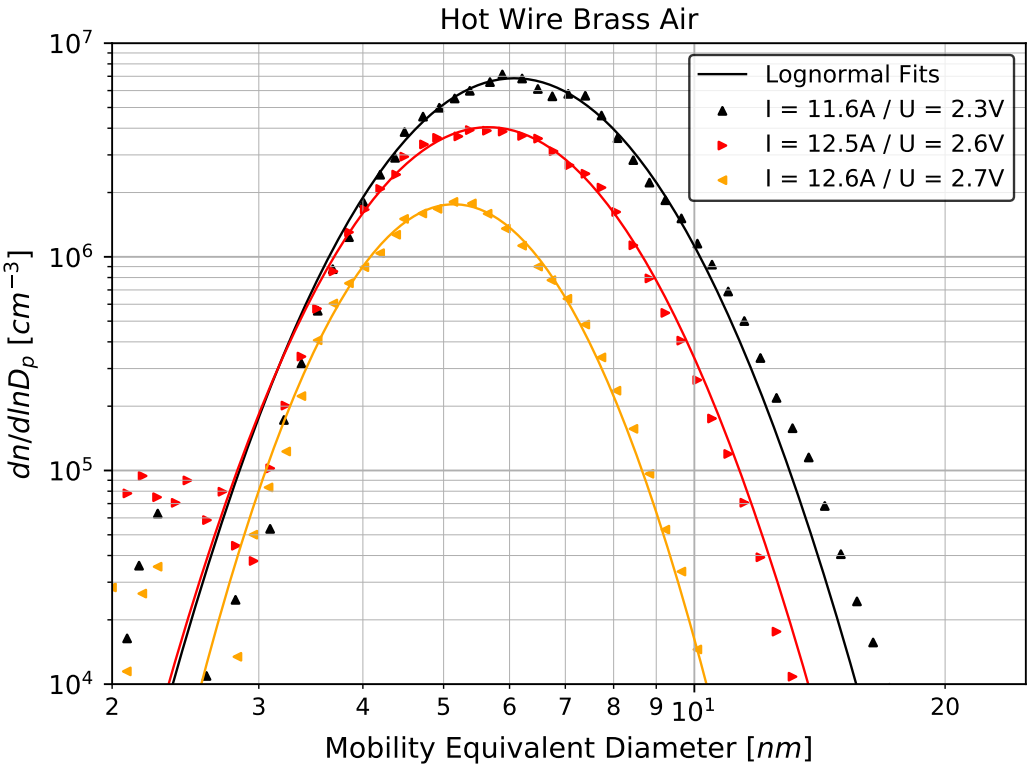

Figure 6.19: Brass particle size distributions generated in air for different power supply settings with corresponding lognormal fits. Remarkable is, that higher wire currents result in lower concentrations of overall smaller particles.

Flow Conditions Hot Wire Brass in Air			
$Q_{HotWire}$ [l/min]	$Q_{sh} = Q_{ex}$ [l/min]	$Q_s = Q_{ae}$ [l/min]	Q_{CPC} [l/min]
6	19	2.2	1.5

Table 6.20: DMPS flow conditions Hot Wire brass in air. Wire diameter = 0.4 mm

Power Supply Settings	μ	σ_{GSD}	Mode [nm]	Median [nm]	Mean [nm]
I = 11.6 A U = 2.3 V	1.87	1.30	6.08	6.51	6.74
I = 12.5 A U = 2.6 V	1.79	1.30	5.66	6.04	6.24
I = 12.6 A U = 2.7 V	1.68	1.45	5.14	5.39	5.52

Table 6.21: Lognormal fitting parameters and corresponding means of brass particle size distributions for different power supply settings.

Conclusion

Seven different wires were operated to generate diverse nanoparticles with the hot wire generator. The particles sizes greatly depend on the metal of choice. With every tested wire it was possible to obtain exceedingly high concentrations, whereas only with silver (in air), stainless steel (in helium and air) and tungsten (in helium) proper stabilization was achieved. For the latter it is, due to its high melting point, particularly easy to sustain a glowing wire, and therefore obtain constant nanoparticle output for up to eight hours.

Because of the high purity of the aerosol and its (wire material dependent) steady and controllable particle generation, glowing wire generators were operated in several studies. Some metals that were tested in this work have been successfully applied in the hot wire generator (Peineke et al. [2006]), including tungsten (Kangasluoma [2013], Chen and Zhang [2017], Bauer [2019]) and silver (Peineke et al. [2006], Müller et al. [1987], Schmidt-Ott [1997], de la Mora et al. [2003]).

Boies [2011] successfully generated high concentrations of gold nanoparticles using a 0.4 mm diameter gold-coated platinum wire with nitrogen as carrier gas. The diameters of these particles are comparable to the ones synthesized in helium for this work, between 5 nm and over 30 nm.

6.3 Tube Furnace Nanoparticle Generator

Generation of synthetic nanoparticles in the gas phase through evaporation of heated materials is a well established approach. In the past, several authors generated successfully particles of various composition employing a tubular furnace. For instance Gurav et al. [1994] synthesized nanometer-size fullerene via vapor condensation, Magnusson et al. [1999] gold nanoparticles, or Scheibel and Porstendorfer [1983] silver and salt, as used in this work. In this thesis, however, the tube furnace was not only operated with air as carrier gas, but also with helium. In both cases, the tube furnace guaranteed very stable nanoparticle output of high concentrations.

In practice, a boat containing high purity silver wool or salt is placed inside the furnace. As the temperature increases, the materials evaporate. A gas flow, in this case pure dry air or helium, streams through the furnace and carries the evaporating material beyond the heated section. As the vapors are cooled directly after the furnace through mixing it with additional carrier gas (in the case of salt), or per water cooling (silver), clusters are formed via nucleation, which further develop towards nanoparticles by condensation and coagulation (Biskos et al. [2008], Karlsson [2004]). With changing the flow conditions, and especially the furnace temperatures, it is possible to shift the number size distributions of the generated nanoparticles (Magnusson et al. [1999]).

Figure 6.20: Carbolite® Gero Tube Furnace Model 301. Picture: Carbolite

In this work, a wire wound single zone tube furnace from Carbolite® was in use (see Figure 6.20). It provides temperatures up to 1200°C.

6.3.1 Silver Nanoparticle Generation in Air and Helium

Silver nanoparticles were generated in carrier gases air and helium. For this purpose, high purity silver wool was placed inside the furnace and heated to temperatures of around 1000°C.

Once the melting point of silver at 1234 K (961°C) (Kirshenbaum et al. [1962]) was reached, the generated particles slightly changed in number and size compared to loose wool. Thus, in order to guarantee reproducibility, all measurements were done with silver, that at least once surpassed its melting point.

Experimental Setup

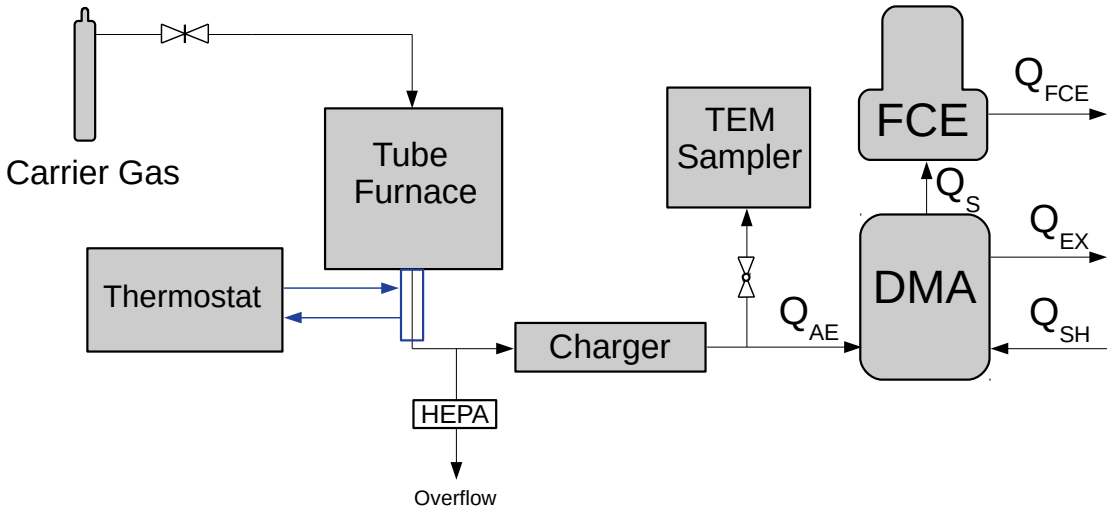

Figure 6.21: Experimental Ag-Tube Furnace DMPS Setup.

For both, helium and air, a volumetric flow of 4.5 l/min of particle free and dry carrier gas into the furnace was provided. Integrated water circulation in a glass tube right after the furnace ensured sufficient cooling of the aerosol. A Lauda RCS 20-D thermostat guaranteed constant water temperature of 25°C.

Downstream of the tube furnace, the particles became neutralized in the TSI Aerosol Neutralizer 3088, were analyzed according to their electrical mobility and detected in the FCE. To prevent any excess pressure in the system, an overflow through a HEPA filter was installed. Furthermore, TEM samples of nanoparticles were taken.

For both measurements, air and helium, a DMA with an inner radius R_{in} = 17.5 mm, outer radius R_{out} = 24.1 mm and length L = 15 mm was operated (see Chapter 2).

Experimental Results

Flow Conditions Ag Air			
$Q_{Furnace}$ [l/min]	Q_{sh} = Q_{ex} [l/min]	Q_s = Q_{ae} [l/min]	Q_{TEM} [l/min]
4.5	19	2.2	1.5

Table 6.22: DMPS and TEM flow conditions

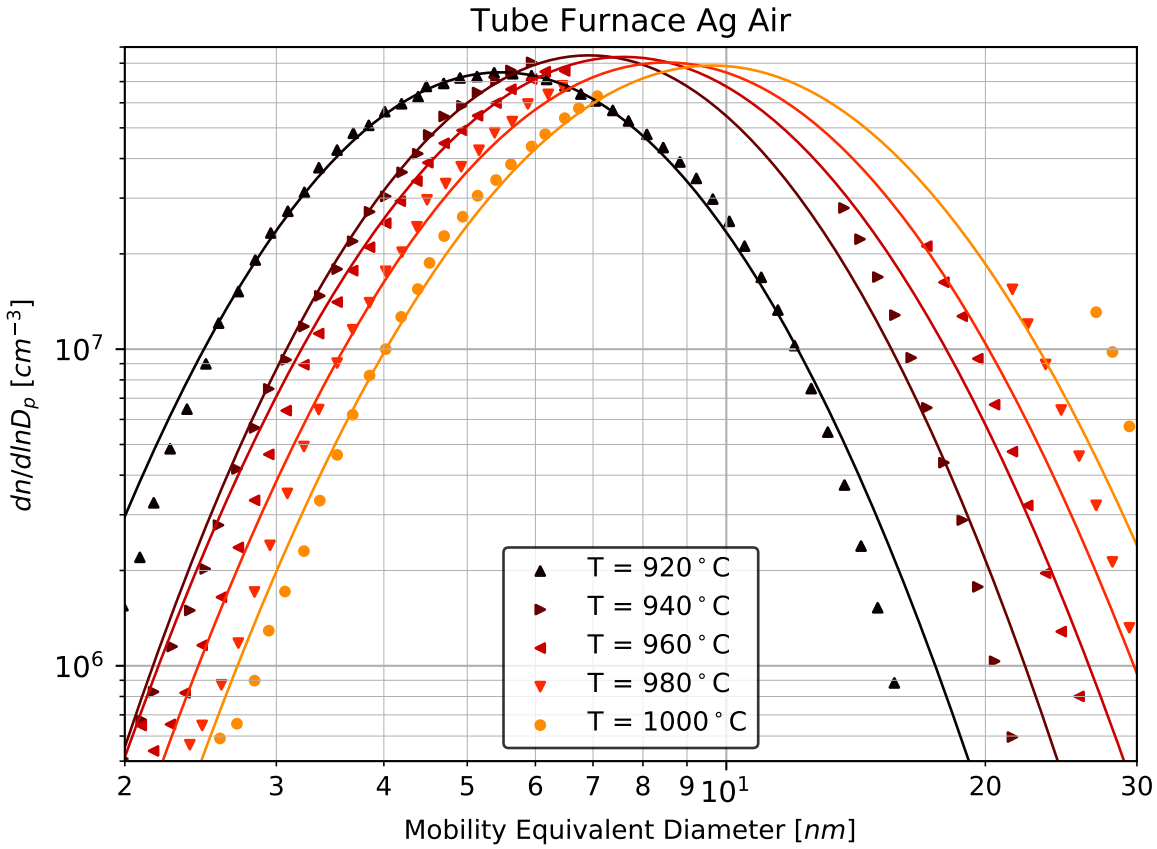

Figure 6.22: Number Size Distributions Tube Furnace Ag in air for different tube furnace temperatures. See text for further explanation.

Furnace Temperature [°C]	μ	σ_{GSD}	Mode [nm]	Median [nm]	Mean [nm]
920	1.86	1.48	5.47	6.39	6.88
940	2.08	1.48	6.93	8.07	8.71
960	2.20	1.52	7.56	9.05	9.86
980	2.32	1.52	8.53	10.18	11.11
1000	2.45	1.54	9.63	11.59	12.71

Table 6.23: Lognormal fit parameters and respective means for different furnace temperatures with carrier gas air

Flow Conditions Ag Helium			
$Q_{Furnace}$ [l/min]	$Q_{sh} = Q_{ex}$ [l/min]	$Q_s = Q_{ae}$ [l/min]	Q_{TEM} [l/min]
4.5	22	1.8	1.5

Table 6.24: DMPS and TEM flow conditions

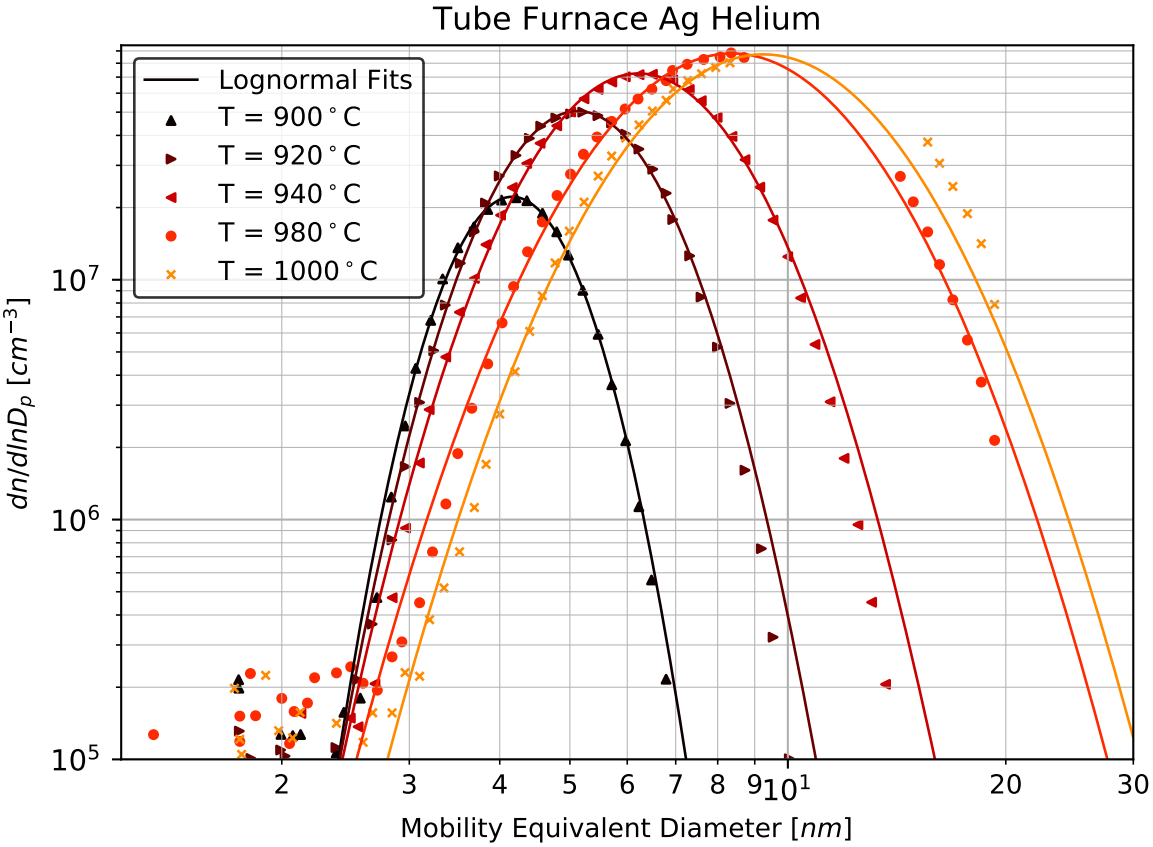

Figure 6.23: Number Size Distributions Tube Furnace Ag in Helium

Furnace Temperature °C	μ	σ_{GSD}	Mode [nm]	Median [nm]	Mean [nm]
900	1.45	1.17	4.16	4.28	4.32
920	1.68	1.23	5.13	5.36	5.49
940	1.89	1.30	6.19	6.65	6.84
980	2.23	1.38	8.37	9.30	9.80
1000	2.33	1.38	9.25	10.23	10.84

Table 6.25: Lognormal fit parameters and respective means for different furnace temperatures with carrier gas helium

For both carrier gases, very high and stable concentrations were achieved. For lower temperatures, the number size distributions show lognormal behavior. The higher the temperature, the wider they become. When the tube furnace was operated with air, particles between 2 nm and 30 nm were generated, with means between 6.88 nm and 12.71 nm. In helium, the distributions are distinctly narrower, the concentrations overall less high. The calculated means are within 4.32 nm and 10.84 nm.

The missing data at the highest concentrations of some distributions is a result of the upper detection limit of the FCE. For that reason, these fits are most likely not as accurate compared to the others, and non-lognormal behavior is possible. Especially in the case of using air as carrier gas, the maximal concentrations are very likely even higher for the topmost temperatures.

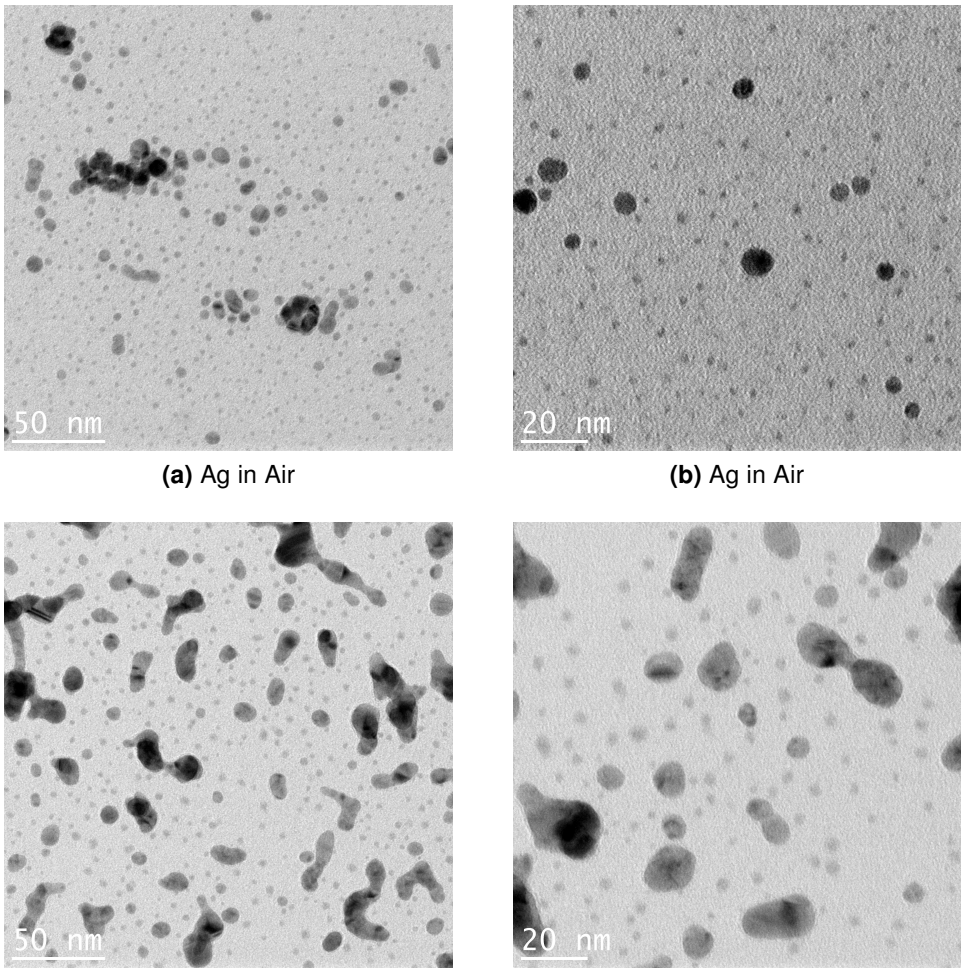

(a) Ag in Air **(b)** Ag in Air

(c) Ag in He **(d)** Ag in He

Figure 6.24: TEM images of sampled silver in air and helium. The upper panels (a) and (b) depict two different magnifications of silver nanoparticles generated in air, the lower panels (c) and (d) likewise in helium. Clearly visible is, that in air the agglomerates consist of distinguishable primary particles, in helium they show coalesced behavior. Pictures taken from Bauer [2019].

Figure 6.24 depicts TEM images of the sampled silver nanoparticles at two different magnifications. The upper panels, Figures (a) and (b) show silver particles generated in air, the lower panels, Figures (c) and (d) silver nanoparticles synthesized in helium.

Both samples were taken with a volumetric flow rate of Q_{TEM}=1.5 l/m for 15 minutes. The TSI Nanometer Aerosol Sampler was operated with a voltage of 1 kV on the sampling electrode.

Particularly noticeable is, in good agreement with the number size distributions, the large amount of small particles with approximate sizes around 10 nm and below. Besides that, the almost spherical primary particles form very different clusters in air versus helium. In air, the agglomerates consist of easily distinguishable primary particles, whereas in helium, they form into a new unity. This disparity is possibly an indication, that the agglomerates are formed in different stages in the process of generation.

6.3.2 Sodium Chloride Nanoparticle Generation

To generate salt nanoparticles, pure sodium chloride was heated up to temperatures of 630°C inside the tube furnace. Sizes within around 4 nm and clearly over 40 nm where synthesized.

Experimental Setup

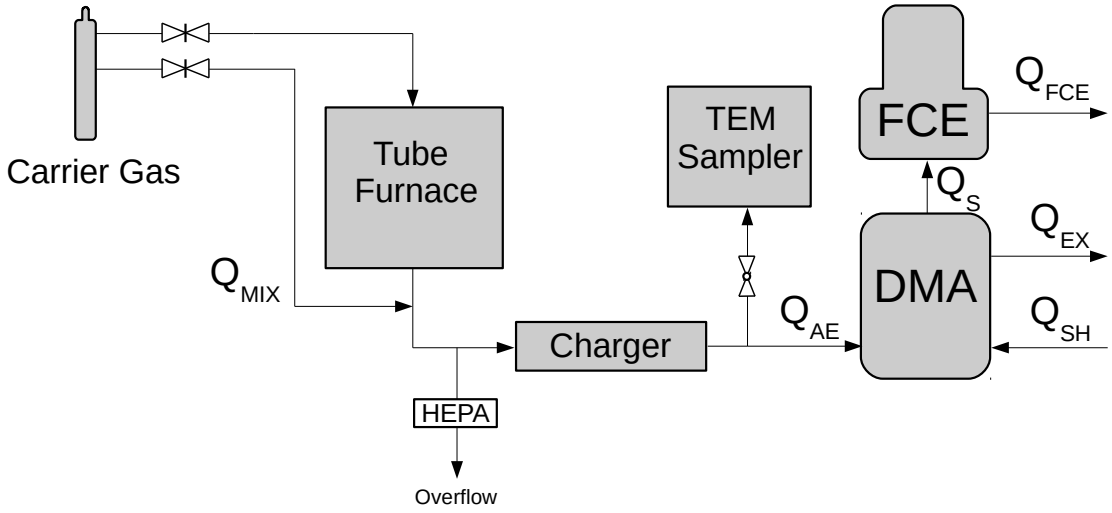

Figure 6.25: Experimental DMPS Setup for the generation of NaCl particles.

Since the applied temperatures are significantly lower when the furnace is operated with sodium chloride, contrary to silver, no water cooling is required. The cooling process is ensured by an additional pure and particle free carrier flow immediately after the furnace (see Q_{MIX} in Figure 6.25). The DMPS is the same as in previous silver measurements, including its DMA dimensions (R_{in} = 17.5 mm, R_{out} = 24.1 mm, L = 15 mm).

TEM samples of the nanoparticles were made. However, the contrast of the sodium chloride is too low to obtain meaningful images, even with sampling times of one hour. Nevertheless, diffraction reflexes of its crystal structure were visible. Furthermore, an EDX analysis was performed which showed distinct peaks for sodium and chlorine.

Characterization of the NaCl Tube Furnace

In this subsection the characterization of the Carbolite® Gero Tube Furnace Model 301, operated with sodium chloride in air is given. Flow conditions are listed in Table 6.26. Figure 6.26 shows particle size distributions of generated nanoparticles for temperatures within 540°C and 630°C.

Flow Conditions NaCl Air				
$Q_{Furnace}$ [l/min]	Q_{MIX} [l/min]	$Q_{sh} = Q_{ex}$ [l/min]	$Q_s = Q_{ae}$ [l/min]	Q_{TEM} [l/min]
2	2	19	2	1.5

Table 6.26: DMPS and TEM flow conditions NaCl Air

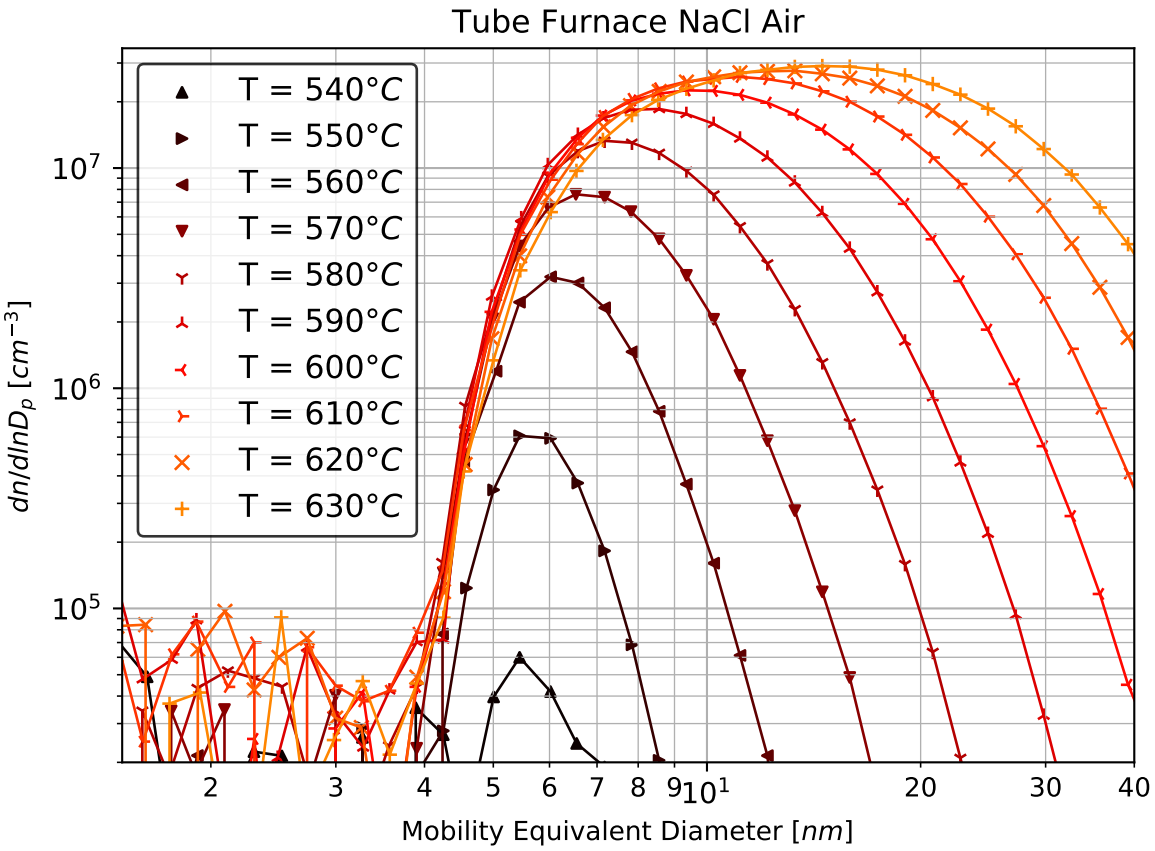

Figure 6.26: Tube Furnace characterization for NaCl in Air. Higher tube furnace temperatures generates higher concentrations and bigger nanoparticles. Sizes within 4-6 nm are present for all settings.

First particles were detectable with 540°C. Increasing temperatures resulted in overall higher concentrations and bigger particles. Interestingly, the size distributions do not shift as a whole, particles within 4 nm and 6 nm were present for all temperatures settings.

7 Humidity Effects on Sodium Chloride Nanoparticles in Air and Helium

As mentioned in Chapter 1, sea salt, with its primary constituent sodium chloride, is a major contributor to the atmospheric aerosol and therefore an important factor for Cloud Condenstion Nuclei (CCN's) numbers and light scattering (Gong [2002], Quinn et al. [1998]). Since sea salt mainly originates from sea spray, the effect of moisture onto these particles is of great interest.

In this section, results of experiments regarding effects of humidity on NaCl nanoparticles are presented.

Relative Humidity (RH) is defined as the ratio of water vapor pressure to its saturation vapor pressure at a given temperature. If the RH of the ambient air exceeds a certain threshold, salt particles absorb water from the gas-phase and form significant bigger aqueous droplets (Biskos et al. [2006], Martin [2000], Cruz and Pandis [2000]). This effect is called deliquescence and should not be mixed up with hygroscopic growth, the condensation of vapor on already aqueous solutions. For sodium chloride particles, Biskos et al. [2006] found these (particle size dependent) thresholds, where deliquescence occurs, to be at RH values of around 75%. The reverse effect, in which water evaporates from the solution with decreasing RH until spontaneous crystallization occurs, is called efflorescence (Martin [2000]).

The experiments performed for this work are focused on a different reaction of humidity on sodium chloride nanopartlicles, the shrinkage of dry particles when they are exposed to moisture. Various authors (Krämer et al. [2000], Biskos et al. [2006], Tauber et al. [2019]) found dry sodium chloride nanoparticles to shrink in the presence of water vapor since they undergo a structural change (further theoretical information on this subject is given by Castarède and Thomson [2018]). For this thesis, sodium chloride nanoparticles were generated in a tube furnace, in two different carrier gases, air and helium. The tube furnace was set to a constant temperature, whereas the RH was increased gradually, from utterly dry, up to around 50%.

7.1 Experimental Setup

Figure 7.1 depicts a schematic of the experimental setup. Sodium chloride nanoparticles were generated using the Carbolite® Gero Tube Furnace Model 301 (see Section 6.3). The furnace was set to a constant temperature of 570°C, the corresponding size distribution is depicted in Figure 6.26. As discussed in Section 6.3.2, the gas flow through the furnace is diluted with Q_{MIX}. The DMPS setup downstream the furnace is described in Section 5.1.

Between the aerosol charger and the DMA, the carrier gas was moistened using a non commercial humidifier that essentially consists of a metallic double-walled pipe.

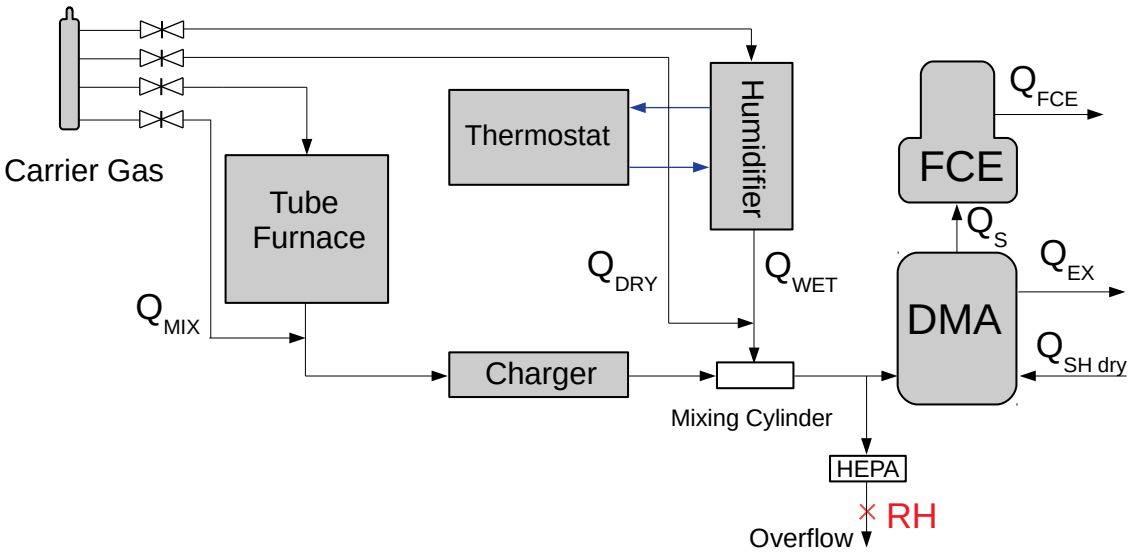

Figure 7.1: The experimental setup for evaluating the effect of humidity on sodium chloride nanoparticles in air and helium. The particle free humidified carrier gas was mixed with the dry flow Q_{DRY}. The sum of Q_{WET} and Q_{DRY} was kept at a constant level, to ensure identical flow conditions throughout the measurements and allowed accurate control over the relative humidity in the mixing cylinder. Corresponding flow rates are listed in Table 7.1 for air, and Table 7.2 for helium. The RH was measured after a HEPA filter, using the Vaisala HMI38 humidity data processor.

The inward of this pipe was covered with blotting paper, drenched with distilled water. The secondary pipe was connected to a thermostat, the Lauda RCS 20-D. By changing the temperature inside the humidifier, the RH was adjusted. The hermetic sealed inner tube, as well as the low gas flow through the humidifier (see Tables 7.1 and 7.2) enabled constant humidification of the carrier gas for around twenty straight hours.

As displayed in Figure 7.1, the dampened gas flow downstream the humidifier Q_{WET} was mixed with dry carrier gas, depicted as Q_{DRY}. The sum of both volumetric flow rates was kept at a constant level throughout the experiment. This allowed precise control of the total RH in the mixing cylinder, without changing any flow conditions. Further, the humidified sodium chloride particles where analyzed in a DMA, which was operated with dry sheath gas, ensured by installing a regenerated silica gel diffusion dryer before every measurement run.

In order to protect the sensors, the RH was measured at the overflow after a HEPA filter. It was verified, that once the filter was saturated, no difference beyond sensor accuracy regarding readings upstream and downstream occurred. Two different RH sensors

were in use, the Sensiron SHT75 and the Vaisala HMI38 humidity data processor with the HMP35E probe. Since the latter has greater accuracy for low RH values (±2% compared to ±1.8-4% for the SHT75) and was manually calibrated beforehand, only HMI38 readings are presented in this section.

7.2 Experimental Results

Figure 7.2 depicts sodium chloride nanoparticle size distribuions generated with the tube furnace at a constant temperature of 570°C (compare Figure 6.26). To enhance comparability, all distributions are normalized to their maximum.

It clearly shows a shift of the distributions to smaller sizes, as the relative humidity increases. This effect is most prominent for low RH values. Moreover, the particle shrinkage seems to be more pronounced for bigger particles, than for smaller ones.

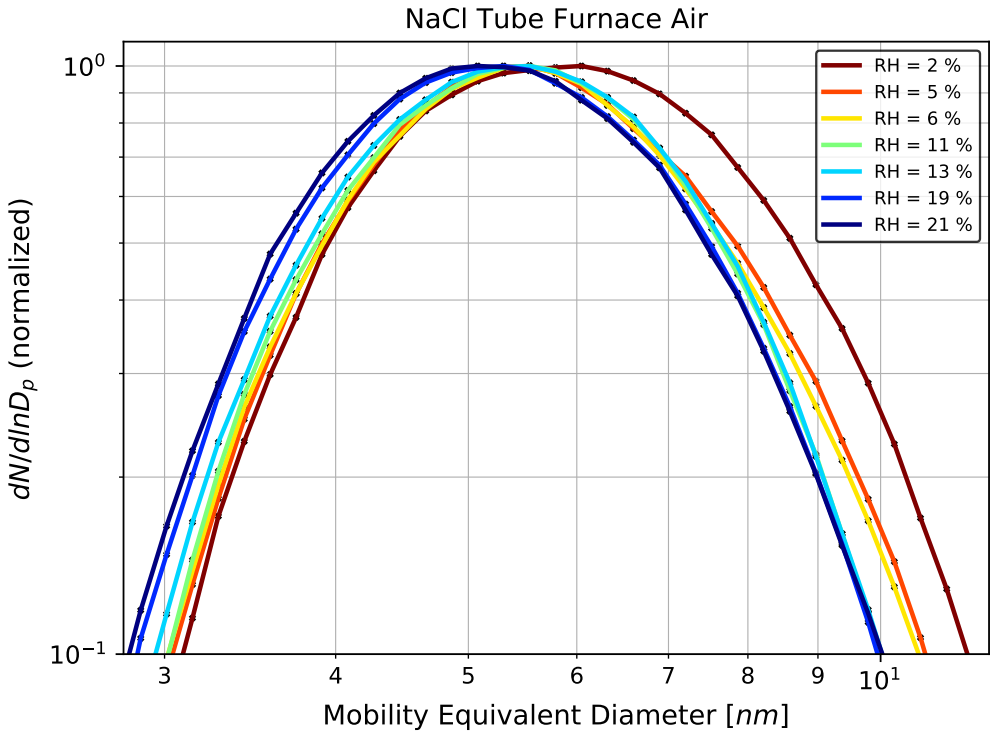

Figure 7.2: Normalized sodium chloride nanoparticle size distributions for different humidities in air. With increasing RH, the distributions shift to the smaller sizes. Shrinking is especially pronounced for bigger particles and for low humidity values.

Flow Conditions Humidity Setup NaCl Air				
$Q_{Furnace}$ [l/min]	Q_{MIX} [l/min]	$Q_{sh} = Q_{ex}$ [l/min]	$Q_s = Q_{ae}$ [l/min]	$\sum Q_{DRY}, Q_{WET}$ [l/min]
2	2	18.5	2	4

Table 7.1: Flow conditions of the polydisperse NaCl humidity setup with carrier gas air

Figure 7.3 depicts the calculated medians of lognormal fits of sodium chloride particle size distributions plotted against relative humidity of a measurement run with up to 34% RH. The right ordinate indicates the percental shrinkage compared to the calculated value at the lowest RH.

Remarkable is the steep gradient at very low humidity under 10 percent whereas at higher RH the curve flattens off. At 34% percent RH the median of the size distributions decreases by about 14%.

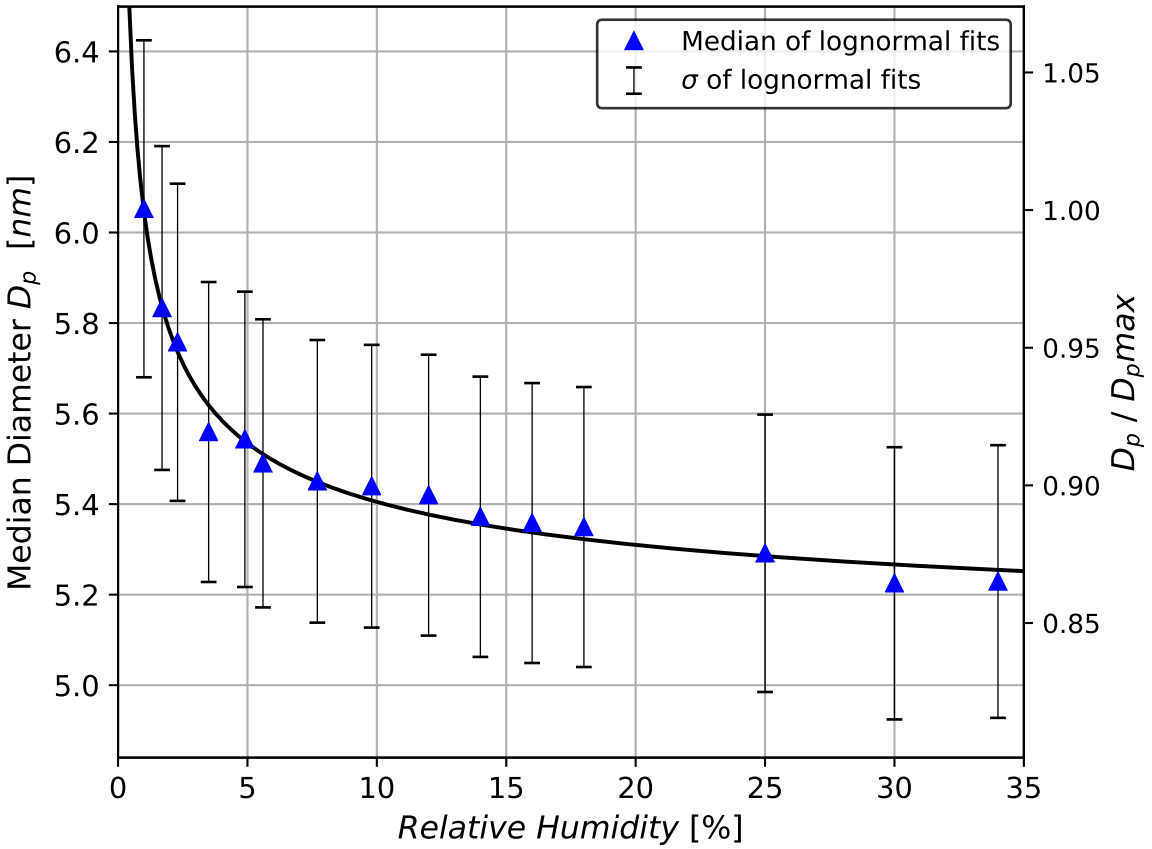

Figure 7.3: Median sizes of sodium chloride nanoparticles in air at different RH and the corresponding four parameter logistic fit. The right ordinate indicates the percental shrinkage compared to the calculated median diameter at the lowest RH. The steep slope at the left indicates, that most of the microstructural rearangement happens at low RH values. Between two and ten percent RH, the median of the sodium chloride nanparticles shrink to about 90% of their initial size. At 34% percent RH the median of the size distributions decrease by about 14%.

The same experiment was conducted with carrier gas helium instead of air. No changes regarding the setup were made (see Figure 7.1), the volumetric flow rates are listed in Table 7.2. Again, the tube furnace was set to a constant temperature of 570°C and only the RH was increased gradually.

Figure 7.4 depicts selected normalized size distributions of sodium chloride nanoparticles generated in carrier gas helium for several RH values within 2% and 22%. The mode of the most dry distribution is around 5 nm, whereas in air it is roughly 6 nm (see Figure 7.2). Here again, with increasing RH the size distributions shift to the smaller sizes. Therefore, sodium chloride nanoparticle shrinking in the presence of water vapor is clearly perceptible not only in air, but also in helium.

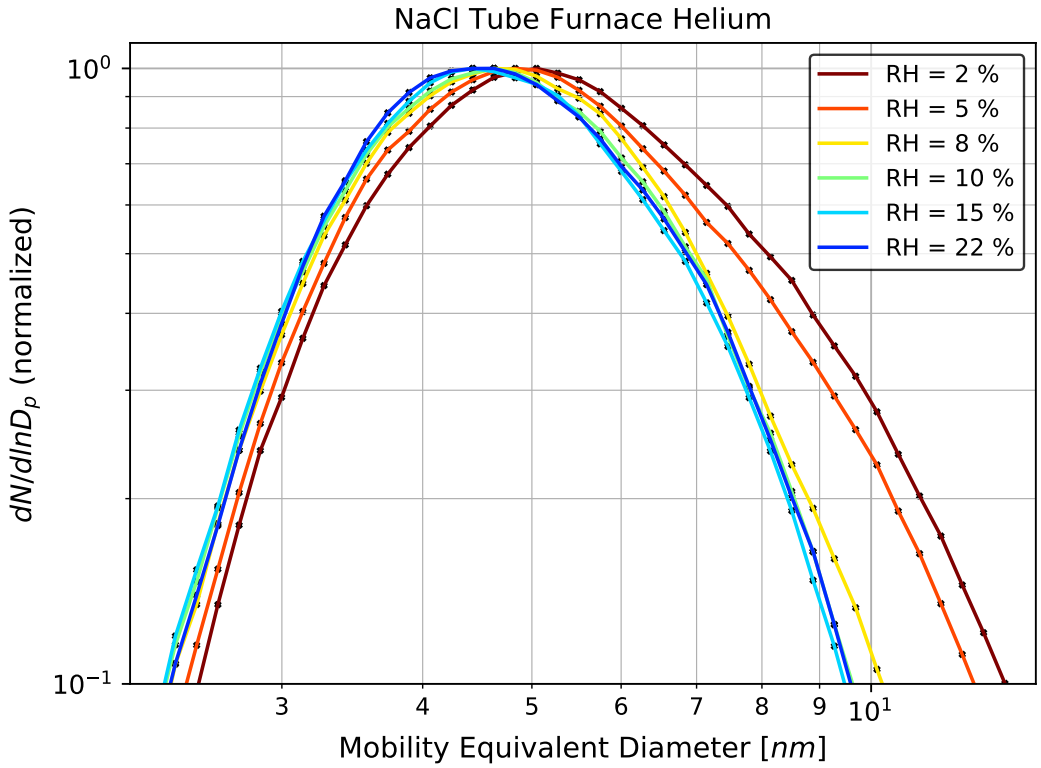

Figure 7.4: Normalized sodium chloride nanoparticle size distributions for different humidities in helium. As in air, with increasing RH the size distributions clearly shift to smaller sizes. Again, bigger particles tend to shrink more than smaller ones.

Flow Conditions NaCl He				
$Q_{Furnace}$ [l/min]	Q_{MIX} [l/min]	$Q_{sh} = Q_{ex}$ [l/min]	$Q_s = Q_{ae}$ [l/min]	$\sum Q_{DRY}, Q_{WET}$ [l/min]
1.5	1.5	20	1.9	3

Table 7.2: Flow conditions of the polydisperse NaCl humidity setup with carrier gas helium.

7.3 Humidity Effects on Monodisperse Sodium Chloride Nanoparticles

As discussed above, the shrinkage effect of sodium chloride nanoparticles in the presence of water vapor is considerably more pronounced the bigger the particles become. For that reason, this effect was examined with monodisperse aerosol nanoparticles. Particles with mobility equivalent diameters of 4.5 nm, 6 nm, 8 nm, 10 nm and 11 nm were investigated.

To this end, a tandem DMA setup was operated. Figure 7.5, taken from Tauber et al. [2019], depicts its schematic.

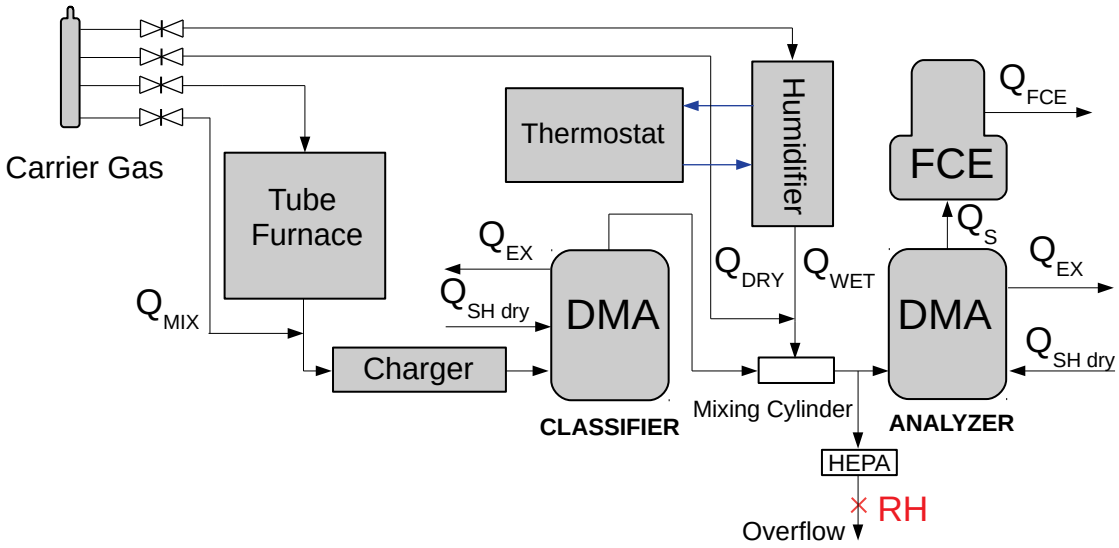

Figure 7.5: Schematic of the setup used for evaluating the effect of humidity on monodisperse sodium chloride nanoparticles, taken from Tauber et al. [2019]. A tandem DMA setup with classifier DMA, which is contrary to the analyzer operated at constant voltage, allowed shrinkage measurements of nanoparticles of certain size. Between both DMAs, the particles were humidified, as desrcibed in Section 7.1.

Compared to the polydisperse setup (Figure 7.1), an additional DMA (referred to as classifier in Figure 7.5) was installed. Contrary to the analyzer, this DMA was set at a fixed voltage, therefore only particles with a very narrow mobility equivalent diameter got through. As discussed in Section 2.4, the transfer function of the DMA can never be considered perfect. This is why, the particles downstream the classifier have not completely equal mobility equivalent diameters, but since the obtained size distributions are highly narrow, the aerosol can be considered as monodisperse. This sodium chloride nanoparticles were humidified in the same way as described in Section 7.1. Downstream the mixing cylinder, the nanoparticles entered the second DMA, where they were analyzed according their electrical mobility (referred to as analyzer in Figure 7.5) and subsequently counted in the FCE. Both DMAs were operated with dry sheath air. The flow conditions of the setup are listed in Table 7.3.

Volumetric Flow Rates NaCl Humidity Setup [l/min]					
			Analyzer		Classifier
$Q_{Furnace}$	Q_{MIX}	$\sum Q_{DRY}, Q_{WET}$	$Q_{sh} = Q_{ex}$	$Q_s = Q_{ae}$	$Q_{sh} = Q_{ex}$
1.5	1.5	3	18.5	2	31

Table 7.3: Flow conditions of the monodisperse NaCl humidity setup with carrier gas air.

Fiugre 7.6 depicts the normalized median diameters versus relative humidity for five different sizes and corresponding four parameter logistic fits. (Data obtained from Tauber et al. [2019]). It clearly illustrates, that smaller sodium chloride nanoparticles tend to shrink less than bigger ones. The median shrinkage of 4.5 nm particles is roughly 4%, while 11 nm particles shrink by about 15% when RH up to 40% is applied.

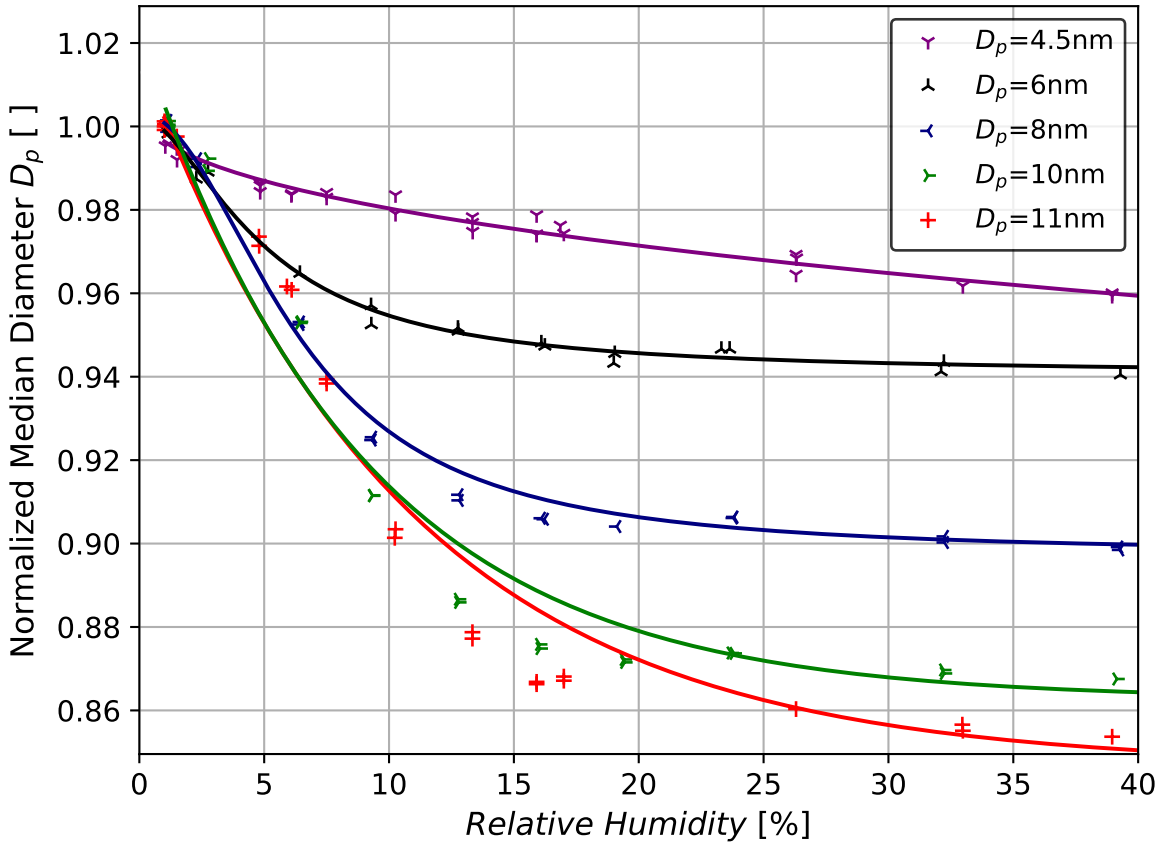

Figure 7.6: Effect of humidity on sodium chloride nanoparticles of various size. The data for this plot was obtained from Tauber et al. [2019]. It is apparent, that smaller particles shrink less than bigger ones. While the median size of particles with a mobility equivalent diameter of 4.5 nm decrease only about 4%, it's roughly 15% for 11 nm particles.

8 Conclusion

Aerosols are ubiquitous in the earth's atmosphere. Their impact on global radiative forcing (Haywood and Boucher [2000]), climate modeling (IPCC [2013]) and human health (WHO [2016]) is of great interest. Particularly nanoparticles, particles in the size range within 1 and 100 nm raise considerable attention, due to their complex behavior regarding formation (Kulmala et al. [2013]) and subsequent growth mechanisms to sizes, where they can act as Cloud Condenstaion Nuclei (CCN's) (Merikanto et al. [2009]). Besides that, the risk assessment of nanoscale materials concerning public health is of major importance (Handy and Shaw [2007]).

For investigation of these convoluted questions, it is crucial to have the possibility to scrutinize aerosol nanoparticles that are synthesized with control over number, size and composition. In this work, three nanoparticle generators were characterized, the Grimm WO_x Generator Model 7.860, a hot wire generator, and the Carbolite® Gero Tube Furnace Type 301. Two different carrier gases were operated, air and helium. Although nanoparticles that are generated in air are more suitable to gain a deeper understanding of atmospheric processes, using helium as carrier gas can lead to new powerful in-situ characterizations of aerosol nanoparticles, as performed by Bauer [2019].

Besides some technical difficulties regarding generating nanoparticles in helium instead of air (see Section 5.2) and theoretical diversities concerning back-calculation of the number size distributions (Section 5.3), in both gases, stable nanoparticle concentrations were successfully synthesized with the hot wire generator as well as the tube furnace.

With regard to the hot wire generator, stainless steel and tungsten were found to have the most constant particle output. For stainless steel, number size distribution modes between 4 nm and 8 nm were measured (in the case of air), with helium the modes were between 4 nm and 5 nm. Tungsten has the highest melting point among all metals and therefore high currents could be applied without the danger of wire rupture. Stable nanopaprticle concentrations up to eight hours were accomplished with measured sizes between 6 nm and 75 nm. The TEM pictures of tungsten clearly show the wide range of particle sizes, from small structures, that consist of only a few primary particles, up to big agglomerates around 100 nm. Broadly speaking, the main difference regarding received size distributions in air compared to helium is, that in the latter generated particles are mostly smaller. This effect is explainable by faster quenching due to the higher thermal conductivity of helium.

Even more stable was the tube furnace generator operated with silver and sodium chloride. TEM pictures of silver were made in air and helium. They show in good agreement with

the measured size distributions, that most particles are up to 10 nm in size. However, the primary particles form very different clusters in air compared to helium. In air the agglomerates consist of distinguishable primary particles, whereas in helium they show coalesced behavior and form into a new unity (see Figure 6.24).

The tube furnace also allowed to perform humidity experiments with no changes in concentration during the whole measurement run. To this end, sodium chloride number size distributions were measured at a constant furnace temperature while increasing the RH from utterly dry up to around 35 %. In both gases the particles shrank with increasing RH. In air, the median of the NaCl nanoparticles decreased by about 14%. Since these data indicated, that bigger particles tend to shrink more than smaller ones, size resolved measurements were performed with the result, that the median size of particles with a mobility equivalent diameter of 11 nm decrease by about 15%, whereas for 4.5 nm particles it's around 4%. TEM pictures of sodium chloride were taken, but while diffraction reflexes of its crystal structure were visible, the contrast of NaCl is too low to obtain pictures of the nanoparticles.

The Grimm WO_x Generator was not possible to be operated in helium, likely because the lack of oxidation processes as well as the possibility that using helium, the coil does not get hot enough. Besides that, it was found to be an eminently convenient generator of air-laden nanoparticles. Its size distributions show lognormal behavior.

Besides limitations of the particle detectors (discussed in Section 4.2), and missing information about particle shapes (see Chapter 2), restraints concerning time resolutions are possible drawbacks of a DMPS. A DMA-train presented by Stolzenburg et al. [2017] overcomes the latter by operating six DMAs at fixed voltage in parallel with as many particle counters. Bauer [2019] on the other hand proved, that Small Angle X-ray Scattering (SAXS) is applicable to perform in-situ characterization of aerosols at ambient pressure and concentrations. Although the DMPS is a powerful tool to obtain crucial information regarding size and number of nanoparticles, the development of in-situ measurement techniques is desirable. Regarding humidity effects on sodium chloride, future efforts should focus on the effect of water vapor on diverse aerosol instruments as well as humidity caused microstructural rearrangements of atmospheric aerosol particles in general.

As can be seen, many efforts are necessary to gain knowledge on the complex behavior of aerosol nanoparticles. Knowledge, that is crucial to answer questions concerning cloud formation, the earth's climate and public health.

Bibliography

William C. Hinds. *Aerosol Technology: Properties, Behavior, and Measurement of Airborne Particles*. JOHN WILEY & SONS INC, 1999. ISBN 0471194107.

M. Kulmala, J. Kontkanen, H. Junninen, K. Lehtipalo, H. E. Manninen, T. Nieminen, T. Petaja, M. Sipila, S. Schobesberger, P. Rantala, A. Franchin, T. Jokinen, E. Jarvinen, M. Aijala, J. Kangasluoma, J. Hakala, P. P. Aalto, P. Paasonen, J. Mikkila, J. Vanhanen, J. Aalto, H. Hakola, U. Makkonen, T. Ruuskanen, R. L. Mauldin, J. Duplissy, H. Vehkamaki, J. Back, A. Kortelainen, I. Riipinen, T. Kurten, M. V. Johnston, J. N. Smith, M. Ehn, T. F. Mentel, K. E. J. Lehtinen, A. Laaksonen, V.-M. Kerminen, and D. R. Worsnop. Direct observations of atmospheric aerosol nucleation. *Science*, 339(6122):943–946, feb 2013. doi: 10.1126/science.1227385.

WHO. *Ambient air pollution: A global assessment of exposure and burden of disease*. World Health Organization, 2016. ISBN 9789241511353.

J. Merikanto, D. V. Spracklen, G. W. Mann, S. J. Pickering, and K. S. Carslaw. Impact of nucleation on global CCN. *Atmospheric Chemistry and Physics*, 9(21):8601–8616, nov 2009. doi: 10.5194/acp-9-8601-2009.

James Haywood and Olivier Boucher. Estimates of the direct and indirect radiative forcing due to tropospheric aerosols: A review. *Reviews of Geophysics*, 38(4):513–543, nov 2000. doi: 10.1029/1999rg000078.

K. S. Carslaw, L. A. Lee, C. L. Reddington, K. J. Pringle, A. Rap, P. M. Forster, G. W. Mann, D. V. Spracklen, M. T. Woodhouse, L. A. Regayre, and J. R. Pierce. Large contribution of natural aerosols to uncertainty in indirect forcing. *Nature*, 503(7474):67–71, nov 2013. doi: 10.1038/nature12674.

IPCC. *Climate Change 2013: The Physical Science Basis. Contribution of Working Group I to the Fifth Assessment Report of the Intergovernmental Panel on Climate Change*. Cambridge University Press, Cambridge, United Kingdom and New York, NY, USA, 2013. ISBN ISBN 978-1-107-66182-0. doi: 10.1017/CBO9781107415324. URL `www.climatechange2013.org`.

Pramod Kulkarni, Paul A. Baron, and Klaus Willeke, editors. *Aerosol Measurement*. John Wiley & Sons, Inc., jun 2011. doi: 10.1002/9781118001684.

Wendelin J. Stark, Sotiris E. Pratsinis, and Alfons Baiker. Heterogeneous catalysis by flame-made nanoparticles. *CHIMIA International Journal for Chemistry*, 56(10):485–489, oct 2002. doi: 10.2533/000942902777680180.

Cátia S.C. Santos, Barbara Gabriel, Marilys Blanchy, Olivia Menes, Denise García, Miren Blanco, Noemí Arconada, and Victor Neto. Industrial applications of nanoparticles – a prospective overview. *Materials Today: Proceedings*, 2(1):456–465, 2015. doi: 10.1016/j.matpr.2015.04.056.

R. D. Handy and B. J. Shaw. Toxic effects of nanoparticles and nanomaterials: Implications for public health, risk assessment and the public perception of nanotechnology. *Health, Risk & Society*, 9(2):125–144, jun 2007. doi: 10.1080/13698570701306807.

L Forbes. Volcanic ash and respiratory symptoms in children on the island of montserrat, british west indies. *Occupational and Environmental Medicine*, 60(3):207–211, mar 2003. doi: 10.1136/oem.60.3.207.

Andreas Dahl, Arash Gharibi, Erik Swietlicki, Anders Gudmundsson, Mats Bohgard, Anders Ljungman, Göran Blomqvist, and Mats Gustafsson. Traffic-generated emissions of ultrafine particles from pavement–tire interface. *Atmospheric Environment*, 40(7):1314–1323, mar 2006. doi: 10.1016/j.atmosenv.2005.10.029.

D.B. Kittelson, W.F. Watts, and J.P. Johnson. Nanoparticle emissions on minnesota highways. *Atmospheric Environment*, 38(1):9–19, jan 2004. doi: 10.1016/j.atmosenv.2003.09.037.

R. R. Khaydarov, R. A. Khaydarov, Y. Estrin, S. Evgrafova, T. Scheper, C. Endres, and S. Y. Cho. Silver nanoparticles. In *Nanomaterials: Risks and Benefits*, pages 287–297. Springer Netherlands, 2009. doi: 10.1007/978-1-4020-9491-0.22.

Prashant Jain and T. Pradeep. Potential of silver nanoparticle-coated polyurethane foam as an antibacterial water filter. *Biotechnology and Bioengineering*, 90(1):59–63, 2005. doi: 10.1002/bit.20368.

Maksym V Yezhelyev, Xiaohu Gao, Yun Xing, Ahmad Al-Hajj, Shuming Nie, and Ruth M O. Regan. Emerging use of nanoparticles in diagnosis and treatment of breast cancer. *The Lancet Oncology*, 7(8):657–667, aug 2006. doi: 10.1016/s1470-2045(06)70793-8.

P. S. Bauer. *In-situ nanoparticle characterization at ambient pressure and concentrations by Small Angle X-ray Scattering*. PhD thesis, University of Vienna, 2019.

G. W. Hewitt. The charging of small particles for electrostatic precipitation. *Transactions of the American Institute of Electrical Engineers, Part I: Communication and Electronics*, 76 (3):300–306, 1957. doi: 10.1109/tce.1957.6372672.

Mang Zhang and Anthony S. Wexler. Cross flow ion mobility spectrometry: Theory and initial prototype testing. *International Journal of Mass Spectrometry*, 258(1-3):13–20, dec 2006. doi: 10.1016/j.ijms.2006.05.012.

Shou-Hua Zhang, Yoshiaki Akutsu, Lynn M. Russell, Richard C. Flagan, and John H. Seinfeld. Radial differential mobility analyzer. *Aerosol Science and Technology*, 23(3): 357–372, jan 1995. doi: 10.1080/02786829508965320.

E.O. Knutson and K.T. Whitby. Aerosol classification by electric mobility: apparatus, theory, and applications. *Journal of Aerosol Science*, 6(6):443–451, nov 1975. doi: 10.1016/0021-8502(75)90060-9.

Benjamin Y.H Liu and David Y.H Pui. A submicron aerosol standard and the primary, absolute calibration of the condensation nuclei counter. *Journal of Colloid and Interface Science*, 47(1):155–171, apr 1974. doi: 10.1016/0021-9797(74)90090-3.

W. Winklmayr, G.P. Reischl, A.O. Lindner, and A. Berner. A new electromobility spectrometer for the measurement of aerosol size distributions in the size range from 1 to 1000 nm. *Journal of Aerosol Science*, 22(3):289–296, jan 1991. doi: 10.1016/s0021-8502(05)80007-2.

Richard C. Flagan. History of electrical aerosol measurements. *Aerosol Science and Technology*, 28(4):301–380, jan 1998. doi: 10.1080/02786829808965530.

Gerhard Steiner. *High resolution mobility spectrometry of molecular ions and their effect on the charging probabilities of airborne particles under bipolar diffusion charging conditions*. PhD thesis, University Vienna, 2011.

Raymond T. Birge. The 1944 values of certain atomic constants with particular reference to the electronic charge. *American Journal of Physics*, 13(2):63–73, apr 1945. doi: 10.1119/1.1990683.

J. Kestin and W. Leidenfrost. The viscosity of helium. *Physica*, 25(1-6):537–555, jan 1959. doi: 10.1016/s0031-8914(59)95585-5.

E. Cunningham. On the velocity of steady fall of spherical particles through fluid medium. *Proceedings of the Royal Society A: Mathematical, Physical and Engineering Sciences*, 83(563):357–365, mar 1910. doi: 10.1098/rspa.1910.0024.

Ira Katz, Georges Caillibotte, Andrew R Martin, and Philippe Arpentinier. Property value estimation for inhaled therapeutic binary gas mixtures: He, xe, n2o, and n2 with o2. *Medical Gas Research*, 1(1):28, 2011. doi: 10.1186/2045-9912-1-28.

S.G Jennings. The mean free path in air. *Journal of Aerosol Science*, 19(2):159–166, apr 1988. doi: 10.1016/0021-8502(88)90219-4.

Haesung Jung, George W. Mulholland, David Y.H. Pui, and Jung Hyeun Kim. Re-evaluation of the slip correction parameter of certified PSL spheres using a nanometer differential mobility analyzer (NDMA). *Journal of Aerosol Science*, 51:24–34, sep 2012. doi: 10.1016/j.jaerosci.2012.04.005.

Mark R. Stolzenburg and Peter H. McMurry. Equations governing single and tandem DMA configurations and a new lognormal approximation to the transfer function. *Aerosol Science and Technology*, 42(6):421–432, apr 2008. doi: 10.1080/02786820802157823.

Spyros N. Pandis John H. Seinfeld. *Atmospheric Chemistry and Physics*. Wiley John + Sons, 2016. ISBN 1118947401.

K.T Whitby and B.Y.H. Liu. *Aerosol Science*. Academic Press Inc.,U.S., 1967. ISBN 0122056507.

J.-S. Chang, P.A. Lawless, and T. Yamamoto. Corona discharge processes. *IEEE Transactions on Plasma Science*, 19(6):1152–1166, 1991. doi: 10.1109/27.125038.

A Hernandez-Sierra, F.J Alguacil, and M Alonso. Unipolar charging of nanometer aerosol particles in a corona ionizer. *Journal of Aerosol Science*, 34(6):733–745, jun 2003. doi: 10.1016/s0021-8502(03)00033-8.

Heinz Burtscher. Measurement and characteristics of combustion aerosols with special consideration of photoelectric charging and charging by flame ions. *Journal of Aerosol Science*, 23(6):549–595, sep 1992. doi: 10.1016/0021-8502(92)90026-r.

L. Tigges, A. Wiedensohler, K. Weinhold, J. Gandhi, and H.-J. Schmid. Bipolar charge distribution of a soft x-ray diffusion charger. *Journal of Aerosol Science*, 90:77–86, dec 2015. doi: 10.1016/j.jaerosci.2015.07.002.

N. A. Fuchs. On the stationary charge distribution on aerosol particles in a bipolar ionic atmosphere. *Geofisica Pura e Applicata*, 56(1):185–193, sep 1963. doi: 10.1007/bf01993343.

A. Wiedensohler. An approximation of the bipolar charge distribution for particles in the submicron size range. *Journal of Aerosol Science*, 19(3):387–389, jun 1988. doi: 10.1016/0021-8502(88)90278-9.

Richard Flagan. Differential mobility analysis of aerosols: A tutorial. 26, 01 2008.

Ross Gunn and R.H. Woessner. Measurements of the systematic electrification of aerosols. *Journal of Colloid Science*, 11(3):254–259, jun 1956. doi: 10.1016/0095-8522(56)90050-2.

John Aitken. On the number of dust particles in the atmosphere 1. *Nature*, 37(957):428–430, mar 1888. doi: 10.1038/037428a0.

Jugal K. Agarwal and Gilmore J. Sem. Continuous flow, single-particle-counting condensation nucleus counter. *Journal of Aerosol Science*, 11(4):343–357, jan 1980. doi: 10.1016/0021-8502(80)90042-7.

P. J. Nolan and L. W. Pollak. The calibration of a photo-electric nucleus counter. *Proceedings of the Royal Irish Academy. Section A: Mathematical and Physical Sciences*, 1946.

Y. Kousaka, T. Niida, K. Okuyama, and H. Tanaka. Development of a mixing type condensation nucleus counter. *Journal of Aerosol Science*, 13(3):231–240, jan 1982. doi: 10.1016/0021-8502(82)90064-7.

J. Bricard, P. Delattre, G. Madelaine, and M. Pourprix. Detection of ultrafine particles by means of a continuous flux condensation nucleus counter. *Fine Particles, B.Y.H. Liu, ed., Academic Press, New York*, 1976.

Kenneth T. Whitby and William E. Clark. Electric aerosol particle counting and size distribution measuring system for the 0.015 to 1 ? size range. *Tellus*, 18(2-3):573–586, jan 1966. doi: 10.3402/tellusa.v18i2-3.9340.

John Zeleny. The distribution of mobilities of ions in moist air. *Physical Review*, 34(2): 310–334, jul 1929. doi: 10.1103/physrev.34.310.

Panich Intra and Nakorn Tippayawong. Development and evaluation of a faraday cup electrometer for measuring and sampling atmospheric ions and charged aerosols. *Particulate Science and Technology*, 33(3):257–263, sep 2014. doi: 10.1080/02726351.2014.952392.

M. Hermann, B. Wehner, O. Bischof, H.-S. Han, T. Krinke, W. Liu, A. Zerrath, and A. Wiedensohler. Particle counting efficiencies of new TSI condensation particle counters. *Journal of Aerosol Science*, 38(6):674–682, jun 2007. doi: 10.1016/j.jaerosci.2007.05.001.

Assoc.Prof.Dr. Panich Intra and Nakorn Tippayawong. An overview of differential mobility analyzers for size classification of nanometer-sized aerosol particles. 30, 03 2008.

G. P. Reischl, J. M. Mäkelä, and J. Necid. Performance of vienna type differential mobility analyzer at 1.2–20 nanometer. *Aerosol Science and Technology*, 27(6):651–672, jan 1997. doi: 10.1080/02786829708965503.

J. Dixkens and H. Fissan. Development of an electrostatic precipitator for off-line particle analysis. *Aerosol Science and Technology*, 30(5):438–453, may 1999. doi: 10.1080/027868299304480.

Friedrich Paschen. Ueber die zum funkenübergang in luft, wasserstoff und kohlensäure bei verschiedenen drucken erforderliche potentialdifferenz. *Annalen der Physik*, 273(5): 69–96, 1889. doi: 10.1002/andp.18892730505.

N. B. Vargaftik and L. V. Yakush. Temperature dependence of thermal conductivity of helium. *Journal of Engineering Physics*, 32(5):530–532, may 1977. doi: 10.1007/bf00860600.

Eric W. Lemmon and R. T. Jacobsen. Viscosity and thermal conductivity equations for nitrogen, oxygen, argon, and air. *International Journal of Thermophysics*, 25, 2004.

B. Baumgartner. Charging, detection and sizing of aerosol nanoparticles in helium and air. Master's thesis, University of Vienna, 2018.

A. Einstein. Über die von der molekularkinetischen theorie der wärme geforderte bewegung von in ruhenden flüssigkeiten suspendierten teilchen. *Annalen der Physik*, 322(8):549–560, 1905. doi: 10.1002/andp.19053220806.

Smoluchowski. Zur kinetischen theorie der brownschen molekularbewegung und der suspensionen. *Annalen der Physik*, 326(14):756–780, 1906. doi: 10.1002/andp.19063261405.

Martin Karlsson. *Methods to Generate Size- and Composition Controlled Aerosol Nanoparticles*. PhD thesis, Lund University, 2004.

George Biskos, Vincent Vons, Caner U. Yurteri, and Andreas Schmidt-Ott. Generation and sizing of particles for aerosol-based nanotechnology. *KONA Powder and Particle Journal*, 26(0):13–35, 2008. doi: 10.14356/kona.26.2008006.

J.M. Grace and J.C.M. Marijnissen. A review of liquid atomization by electrical means. *Journal of Aerosol Science*, 25(6):1005–1019, sep 1994. doi: 10.1016/0021-8502(94)90198-8.

G. I. Taylor. Disintegration of water drops in an electric field. *Proceedings of the Royal Society of London. Series A. Mathematical and Physical Sciences*, 280(1382):383–397, jul 1964. doi: 10.1098/rspa.1964.0151.

A. Ankilov, A. Baklanov, M. Colhoun, K.-H. Enderle, J. Gras, Yu. Julanov, D. Kaller, A. Lindner, A.A. Lushnikov, R. Mavliev, F. McGovern, T.C. Connor, J. Podzimek, O. Preining, G.P. Reischl, R. Rudolf, G.J. Sem, W.W. Szymanski, A.E. Vrtala, P.E. Wagner, W. Winklmayr, and V. Zagaynov. Particle size dependent response of aerosol counters. *Atmospheric Research*, 62(3-4):209–237, jun 2002. doi: 10.1016/s0169-8095(02)00011-x.

Wolf-Dieter Schubert Erik Lassner. *Tungsten*. Springer US, 2012. ISBN 1461372259.

W.D. Kilpatrick. An experimental mass-mobility relation for ions in air at atmospheric pressure. In *Proc. Annu. Conf. Massspectrosc*, volume 19, pages 320–325, 1971.

A. Schmidt-Ott, P. Schurtenberger, and H. C. Siegmann. Enormous yield of photoelectrons from small particles. *Physical Review Letters*, 45(15):1284–1287, oct 1980. doi: 10.1103/physrevlett.45.1284.

H. Burtscher, L. Scherrer, H. C. Siegmann, A. Schmidt-Ott, and B. Federer. Probing aerosols by photoelectric charging. *Journal of Applied Physics*, 53(5):3787–3791, may 1982. doi: 10.1063/1.331120.

J. Fernandez de la Mora, L. de Juan, K. Liedtke, and A. Schmidt-Ott. Mass and size determination of nanometer particles by means of mobility analysis and focused impaction. *Journal of Aerosol Science*, 34(1):79–98, jan 2003. doi: 10.1016/s0021-8502(02)00121-0.

C. Peineke, M.B. Attoui, and A. Schmidt-Ott. Using a glowing wire generator for production of charged, uniformly sized nanoparticles at high concentrations. *Journal of Aerosol Science*, 37(12):1651–1661, dec 2006. doi: 10.1016/j.jaerosci.2006.06.006.

ed. David R. Lide, editor. *CRC Handbook of Chemistry and Physics*. CRC Press, 85th edition edition, 2005.

J. Kangasluoma. Remarks on ion generation for CPC detection efficiency studies in sub-3-nm size range. *Aerosol Science and Technology*, 47(5):556–563, may 2013. doi: 10.1080/02786826.2013.773393.

Hui Chen and Zhenzhong Zhang. Condensation-type quasi monodisperse aerosol generator with WOx nanoparticles as nuclei produced by glowing wire method. *Powder Technology*, 313:344–352, may 2017. doi: 10.1016/j.powtec.2017.02.064.

U. Müller, A. Schmidt-Ott, and H. Burtscher. First measurement of gas adsorption to free ultrafine particles:o2on ag. *Physical Review Letters*, 58(16):1684–1686, apr 1987. doi: 10.1103/physrevlett.58.1684.

Schmidt-Ott. Characterizing nanoparticles by scanning tunneling microscopy and scanning tunneling spectroscopy. *Journal of Aerosol Science*, 28:S729–S730, sep 1997. doi: 10.1016/s0021-8502(97)85363-3.

Adam M. Boies. Hot-wire synthesis of gold nanoparticles. *Aerosol Science and Technology*, 45(5):654–663, mar 2011. doi: 10.1080/02786826.2010.551145.

Abhijit S. Gurav, Toivo T. Kodas, Lu-Min Wang, Esko I. Kauppinen, and Jorma Joutsensaari. Generation of nanometer-size fullerene particles via vapor condensation. *Chemical Physics Letters*, 218(4):304–308, feb 1994. doi: 10.1016/0009-2614(93)e1491-x.

Martin H. Magnusson, Knut Deppert, Jan-Olle Malm, Jan-Olov Bovin, and Lars Samuelson. Size-selected gold nanoparticles by aerosol technology. *Nanostructured Materials*, 12(1-4):45–48, jan 1999. doi: 10.1016/s0965-9773(99)00063-x.

H.G. Scheibel and J. Porstendorfer. Generation of monodisperse ag- and NaCl-aerosols with particle diameters between 2 and 300 nm. *Journal of Aerosol Science*, 14(2):113–126, jan 1983. doi: 10.1016/0021-8502(83)90035-6.

A.D. Kirshenbaum, J.A. Cahill, and A.V. Grosse. The density of liquid silver from its melting point to its normal boiling point 2450k. *Journal of Inorganic and Nuclear Chemistry*, 24 (3):333–336, mar 1962. doi: 10.1016/0022-1902(62)80188-2.

S. L. Gong. Canadian aerosol module (CAM): A size-segregated simulation of atmospheric aerosol processes for climate and air quality models 2. global sea-salt aerosol and its budgets. *Journal of Geophysical Research*, 107(D24), 2002. doi: 10.1029/2001jd002004.

P. K. Quinn, D. J. Coffman, V. N. Kapustin, T. S. Bates, and D. S. Covert. Aerosol optical properties in the marine boundary layer during the first aerosol characterization experiment (ACE 1) and the underlying chemical and physical aerosol properties. *Journal of Geophysical Research: Atmospheres*, 103(D13):16547–16563, jul 1998. doi: 10.1029/97jd02345.

G. Biskos, A. Malinowski, L. M. Russell, P. R. Buseck, and S. T. Martin. Nanosize effect on the deliquescence and the efflorescence of sodium chloride particles. *Aerosol Science and Technology*, 40(2):97–106, feb 2006. doi: 10.1080/02786820500484396.

Scot T. Martin. Phase transitions of aqueous atmospheric particles. *Chemical Reviews*, 100(9):3403–3454, sep 2000. doi: 10.1021/cr990034t.

Celia N. Cruz and Spyros N. Pandis. Deliquescence and hygroscopic growth of mixed inorganic-organic atmospheric aerosol. *Environmental Science & Technology*, 34(20): 4313–4319, oct 2000. doi: 10.1021/es9907109.

Lutz Krämer, Ulrich Pöschl, and Reinhard Niessner. Microstructural rearrangement of sodium chloride condensation aerosol particles on interaction with water vapor. *Journal of Aerosol Science*, 31(6):673–685, jun 2000. doi: 10.1016/s0021-8502(99)00551-0.

Christian Tauber, Sophia Brilke, Peter Josef Wlasits, Paulus Salomon Bauer, Gerald Köberl, Gerhard Steiner, and Paul Martin Winkler. Humidity effects on the detection of soluble and insoluble nanoparticles in butanol operated condensation particle counters. *Atmospheric Measurement Techniques Discussions*, pages 1–18, jan 2019. doi: 10.5194/amt-2019-23.

Dimitri Castarède and Erik S. Thomson. A thermodynamic description for the hygroscopic growth of atmospheric aerosol particles. *Atmospheric Chemistry and Physics*, 18(20): 14939–14948, oct 2018. doi: 10.5194/acp-18-14939-2018.

Dominik Stolzenburg, Gerhard Steiner, and Paul M. Winkler. A dma-train for precision measurement of sub-10 nm aerosol dynamics. *Atmospheric Measurement Techniques*, 10(4):1639–1651, may 2017. doi: 10.5194/amt-10-1639-2017.

List of Figures

List of Tables